NASA CR-54705
EOS REPORT 5470-Final

HALL CURRENT ACCELERATOR

by

G. L. Cann, R. L. Harder, R. A. Moore,
and P. D. Lenn

prepared for

NATIONAL AERONAUTICS AND SPACE ADMINISTRATION

CONTRACT NAS3-5909

ELECTRO-OPTICAL SYSTEMS, INC., Pasadena, California
A Subsidiary of Xerox Corporation

Requests for copies of this report should be referred to

National Aeronautics and Space Administration
Office of Scientific and Technical Information
Attention: AFSS-A
Washington, D.C. 20546

NASA CR-54705
EOS REPORT 5470-Final

FINAL REPORT

HALL CURRENT ACCELERATOR

by

G. L. Cann, R. L. Harder, R. A. Moore,
and P. D. Lenn

prepared for

NATIONAL AERONAUTICS AND SPACE ADMINISTRATION

4 February 1966

CONTRACT NAS3-5909

Technical Management
NASA Lewis Research Center
Cleveland, Ohio
Spacecraft Technology Division
Stanley Domitz

ELECTRO-OPTICAL SYSTEMS, INC. – PASADENA, CALIFORNIA
A Subsidiary of Xerox Corporation

HALL CURRENT ACCELERATOR

G. L. Cann, R. L. Harder, R. A. Moore, P. D. Lenn
Electro-Optical Systems, Inc.
A Subsidiary of Xerox Corporation

ABSTRACT

15830

Experimental and analytic investigations of axisymmetric Hall current accelerators are reported. The purpose of the investigations was to determine the performance potential of such a device as an electric space propulsion engine. Parametric studies of the accelerator were made with several propellants, emphasis being placed upon the tests using hydrogen and sodium. Some diagnostic measurements on the engine and exhaust beam were made and are reported, the most important being a determination of the current path in the exhaust beam of the hydrogen accelerator. Mechanisms to explain thrust production and other engine characteristics are postulated and discussed in detail. The concept of an "effective" mass flow rate, which is determined by a minimum potential hypothesis, is developed to the point where a complete analysis of a simplified model of the accelerator can be made. Such an analysis is completed and the results are compared, where possible, with experimental results.

Author

CONTENTS

CONTENTS (contd)

ILLUSTRATIONS

ILLUSTRATIONS (contd)

ILLUSTRATIONS (contd)

1. INTRODUCTION

The development of the direct current axisymmetric plasma accelerator over the past several years has been a technological accomplishment of considerable magnitude. However, the desire to rapidly develop the accelerator into a practical space propulsion engine has led to an inordinate emphasis being placed upon obtaining overall performance comparable to or better than that of ion engines. A comprehensive investigation of the physical principles which determine the performance capability of the engine has consequently not taken place. Nor is it likely, even if a program were initiated to this end, that results of immediate value would appear because of the multiplicity of mechanisms and their interdependency. This should not deter us, however, from developing hypotheses for the mechanisms in the engine and deriving from these semi-empirical design parameters and criteria for optimizing the configuration.

A few very general statements concerning the mechanisms which govern the behavior of magnetic annular accelerators can be made:

1. Thrust is produced by the expulsion of high-velocity ions from the engine.
2. The ions are produced by collisions between atoms and energetic electrons throughout the volume of the discharge.
3. The electrical discharge extends a considerable distance downstream of the electrodes and, hence, transfers most of the energy and momentum to the gas far from the engine. Viscous interaction with engine components can hence be neglected. Thermal conduction effects to all engine components other than the cathode can also be neglected.

4. Since the discharge occurs in a low density environment, most of the internal energy of the gas can be associated with the electrons. As the arc current becomes large, e.g., > 1000 amps, then this may not remain valid, since the high pressures in the cathode jet could lead to considerable ion heating due to electron-ion collisions. Similarly, the energy associated with the body forces exerted on the gas can be associated with the ions.
5. The power transferred to the anode can almost all be attributed to the energy convected by the electrons as they carry the current into the anode. This is especially true when the cathode tip is flush with the anode face. As the cathode tip is recessed further and further back in the anode cavity, more and more of the anode heating will be due to conduction from the hot gas.
6. The solenoidal magnetic field that is applied acts as a magnetic nozzle for any plasma that is produced by the discharge. That is, all forms of electron and ion energy (exclusive of ionization and radiation) are converted into axial and radial ion velocities by expansion out of the magnetic field. This indicates that all the electrical power of the discharge can be converted into beam power except for: (a) The anode and cathode power loss, (b) The power used in ionizing the propellant.
7. All of the beam energy cannot be converted into axial kinetic energy. The ions will have some tangential velocity to balance the torque produced on the accelerator by the discharge current crossing the applied magnetic field. There will also be some radial velocity of the ions due to the shape of the magnetic nozzle.
8. A large fraction of the thrust reaction occurs on the magnet. This indicates that azimuthal currents must be flowing in the plasma tube.

The above considerations lead to some well defined design criteria:

1. Raise the arc voltage to as high a value as possible while maintaining the electron temperature at modestly low values. This will transfer a large amount of kinetic energy directly to the ions with good thermal efficiency.
2. Inject the propellant so that it will be ionized in a region of high potential, i.e., near anode potential. This will allow the ions to carry some of the current and thus acquire energy directly from the electric field.
3. Use a propellant of low molecular weight to obtain the best possible energy transfer characteristics between ions and electrons. Also pick a propellant with a low first ionization potential so the gas can be easily singly ionized with a minimum power loss. The second ionization potential should be as high as possible to prevent excitation or ionization of the second electron.

One of the most difficult questions that confronts the experimentalist who is attempting to evaluate the accelerator performance capability is to define the conditions which will constitute a valid test. The problem arises because the discharge extends into the wake an indeterminate distance. The specific questions are these:

1. How large must the vacuum tank be to insure that the tank walls do not affect engine performance?
2. What precautions which must be taken to insure that the mass flow rate in the exhaust beam is equal to or lower than the propellant injection rate into the accelerator?

Preliminary tests indicated that the size of the tank is not critical. However, the possibility still exists that in some cases the tank may limit the size of the discharge, or may actually carry some of the discharge current over a part of its path. Tests in tanks of various diameters and lengths have been conducted at EOS and elsewhere but the results are still not conclusive because other variables occurred simultaneously in the tests.

The problem of determining the ratio of beam particle flux rate to propellant injection rate is formidable. When tests are being conducted with an alkali metal propellant any one of the following sources of extra material for the beam exists:

1. Propellant can condense on any cool engine component. When conditions are altered so that the engine heats up, this propellant can vaporize and enter the exhaust beam.
2. If all of the beam particles do not adhere to the target or tank walls once they have struck it, then this "backstreaming" propellant can be ionized and accelerated in the discharge, resulting in a recirculation of the propellant.
3. If any background gaseous material is present in the vacuum tank, e.g., air leakage, then this substance can be ionized and accelerated by the discharge.
4. The heat flux to one or both electrodes can become high enough to vaporize electrode or insulator material. The discharge may, once again, ionize and accelerate this material.

Items 1 and 4 can be controlled by proper design and by exercising care while testing. By using adequate pumping capacity and sealing of the vacuum tank, the impurity level of ambient gas can be maintained adequately low. If necessary, liquid nitrogen liners can be used. There is real difficulty, however, in determining if the recirculation of propellant can ever be completely eliminated. The beam itself is likely to dislodge particles that have condensed in the target area and these could backstream into the volume of the discharge.

The extent to which any one or several of the above-mentioned four processes may have had some influence upon performance data that have been reported elsewhere and in this report is difficult to assess. Since it is not possible to obtain sufficient detail from reading reports of other work, we shall confine our comments on this subject to test results reported by EOS exclusively. The most important observation is as follows.

When an alkali metal is used as the propellant, it has been found that increasing the background pressure, by injecting gas into the vacuum tank, results initially in a decrease of measured thrust and a consequent degradation in engine performance. In all cases, it has been found that the performance either remains constant or improves as the background pressure is reduced below 1μ. Further discussions of this problem will be found throughout this report.

The development of a comprehensive theory describing the mechanisms and performance capability of the accelerator has also proven to be a very difficult task. A phenomenological theory was developed at EOS (Ref. 1) which used measured dependencies of thrust and anode power loss upon the controllable variables to develop relations among the voltage, specific impulse, and thrust efficiency. Naturally, this approach did not identify any mechanisms for thrust production or power losses. A more fundamental approach to the problem is presented in this report and a complete analysis is carried out for a simplified model of the accelerator. The significance of some overall conservation principles is also discussed.

The underlying principle of the analytic approach developed at EOS is that the discharge will operate in a minimum potential mode. This follows the accepted approach to studying arc discharge phenomena, which is assumed to remain valid even when a significant fraction of the discharge power is transferred directly into kinetic energy of the ions. This leads to the concept of a critical mass flow defined as the effective mass flow rate. The ideas behind this concept are simple. Assume that a discharge is occurring in a vacuum environment across an electrode configuration where the arc current and applied magnetic field strength are held constant while the propellant flow rate through the engine is varied. If the thrust is electromagnetic in origin, it will not increase appreciably as the flow rate increases. If the propellant is fully ionized in the discharge, then as the flow

rate is increased the beam power decreases and the power used to ionize the propellant increases. These two competing processes indicate that there will probably be some mass flow rate at which the power input, or voltage drop will be a minimum. It is then assumed that the discharge will encompass enough volume to ionize propellant at just this critical rate, provided enough is available. If more than the "effective" mass flow rate is injected through the engine, it is assumed that the excess is not ionized and, hence, diffuses out of the accelerator unused. If less than the "effective" mass flow rate is injected through the electrodes, the discharge will attempt to entrain ambient material to make up the deficit. A considerable amount of the analytic effort presented in this report revolves around an attempt to compute this "effective" mass flow rate and to determine the parameters upon which it depends.

2. PHYSICAL PROCESSES

All electric propulsion engines rely upon two basic processes:

1. Ion production
2. Ion acceleration

In accomplishing these ends, certain penalties must be paid, which are usually evaluated in terms of propellant mass utilization and electric power utilization. The axisymmetric Hall current accelerator, or MPD arc, accomplishes all of the three processes mentioned above by means of a dc arc struck between electrodes placed symmetrically in a solenoidal magnetic field. However, the measurements that can be made are such that it is virtually impossible to evaluate propellant mass utilization and power utilization independently. Thus, great simplicity of design is gained at the expense of great complexity in the interaction of the engine operating mechanisms.

One of the features of the MPD arc that appears most baffling to physicists is the apparently uncorrelated behavior of the arc current and the ion flux rate. Since the electrons can carry an appreciable fraction of the arc current, considerable energy from the electric field is transferred initially to the electron internal and kinetic energy, from where it can later be transferred to the ions. This allows the ions, under some circumstances, to leave the engine with energies greater than they could achieve by falling through the potenfial drop of the discharge. The detailed process by which this can be accomplished will be discussed in the following paragraphs.

2.1 Ion Production

The momentum conservation equations indicate that some torque and force reaction must occur on the engine (see Section 3). For this to happen, ions must be produced in and expelled from the motor with axial and angular velocity. The fewer the ions, the higher the resultant velocities must be and, consequently, the beam power must be higher. On the other hand, as the ion production and expulsion rate increases, the power in ion production becomes very high, hence some ion flow rate must exist at which the electrical power into the discharge is a minimum. If the arc current is held fixed, this implies that the discharge seeks a minimum voltage mode in which to operate. The above argument then indicates that the arc accomplishes this end by ionizing the optimum amount of propellant to expell in the exhaust beam. The key, then, to explaining the operating characteristics of the engine lies in determining the optimum ion exhaust rate and in understanding the production process for these ions throughout the volume of the discharge.

Previously (Ref. 1), it had been concluded that volume ionization away from the electrode surfaces could not account for all of the ions produced. At that time, it was assumed that the electron temperature was about $10{,}000^{\circ}K$. Since then, data on anode heating have indicated that the electron temperature may be much higher, e.g., $\approx 30{,}000 - 50{,}000^{\circ}K$. This raises the probability of volume ion production, through electron atom collisions, to values where it can account for most, if not all, of the ions used in the exhaust beam.

The atoms are not confined to any great extent by the electric discharge. Hence the flow field of the gas will be substantially the same as one would find for the gas issuing from the orifice with no discharge present. The discharge must now encompass this gas and adjust the electron temperature and density throughout its volume so as to ionize the optimum amount of propellant. Clearly, to get good propellant utilization, the injected flow rate should be close to the ion flow rate in the beam. However, in the interest of obtaining best

overall efficiency, it may be necessary to inject slightly more propellant than is used by the beam. This would help to restrict the volume of the discharge and perhaps keep the electron temperature to lower values, thus reducing power loss by electron energy convection to the anode.

Since a vast majority of atom-electron collisions are elastic collisions, the energy used to ionize one atom must be considerably greater than the ionization potential of the atom. The energy difference is transferred into the internal energy of the atoms and ions. If most of the injected mass is eventually ionized, this energy is not lost but is available to be transferred into beam kinetic energy by eventual expansion through the magnetic nozzle. It is obvious, of course, that this internal energy of the heavy particles can never be higher than that of the electrons. This argument indicates that the ionization process need not be efficient. However, the number of inelastic collisions that excite the electrons to states that can radiate should be minimized. This is basically a problem of propellant selection.

The electron internal energy results from the electron current passing through the potential drop and being randomized by collisions with heavy particles. For this reason it would be expected that the highest electron energy would be found in the anode sheath, after the electrons have fallen through most of the potential drop. This is fortuitous, since it is precisely in this region that the highest production rate is wanted, to let the ions gain a maximum of kinetic energy by falling through the potential back toward the cathode jet

2.2 Ion Acceleration

Momentum can be transferred to the ions from electric fields or from collisions with other particles. For convenience, the momentum exchange processes in a fully ionized gas through which an electric discharge is passing shall be discussed.

Locally, the force on each ion is given by the following expressions:

Axial: $$|e|\left\{E_z + u_I B_\theta - v_I B_r - \frac{J_z}{\sigma}\right\}$$

Radial: $$|e|\left\{E_r + v_I B_z - w_I B_\theta - \frac{J_r}{\sigma}\right.$$

Azimuthal: $$|e|\left\{w_I B_r - u_I B_z - \frac{J_\theta}{\sigma}\right\}$$

If an electric discharge is established in a uniform axial magnetic field we shall call the region where the current flows downstream the anode sheath and the region where it flows upstream the cathode jet. If a cathode of maximum diameter R_c is surrounded by an anode ring of diameter R_A ($R_A > R_c$) we ask the questions:

1. Does the cathode jet expand out to meet the anode sheath?
2. Does the anode sheath contract in diameter to meet the cathode jet?
3. Do both (1) and (2) occur simultaneously?

Consider first the cathode jet. If the cathode jet is to expand outward, conservation of momentum states that the axial momentum of the jet must increase and the rotational momentum of the jet must increase. However, the local (E + v x B) axial and tangential electric fields are both in the wrong direction to accelerate the ions and the mementum must hence be transferred to them by electron collisions. This is a highly dissipative process, resulting in strong heating of the electrons. This increases the rates of entropy production over that caused by ion-electron drag in a purely dissipative plasma (no body force).

In the anode jet the situation is quite different. Both E_z and $u_I B_\theta$ are in the positive z direction, thus helping to accelerate the ions axially. The only dissipative or entropy producing

process is that associated with the electron-ion drag. Similarly, in the aximuthal direction the local electric field $u_I B_z$ aids the Hall currents in spinning up the ions. This allows the Hall currents to be smaller and thus dissipate less energy in spinning up the gas to the required velocity. These rather crude arguments indicate that if the discharge tends to operate at a minimum potential, then the current in the anode sheath would tend to move inward to meet the cathode jet, rather than vice versa.

Further strength is lent to this argument when the radial force balance on the anode sheath is investigated. Assuming that no net radial force can exist on the anode sheath as a whole, an integral of the radial momentum equation gives the following relation:

$$p_o - p_i = \int J_\theta B_z \, dr - \int J_z B_\theta \, dr$$

$$\approx \int J_\theta B_z \, dr = \frac{\mu_o I^2}{8\pi^2 R} + (p_i - p_o)$$

where $p_o - p_i$ = the pressure difference across the sheath.

R = average radius of the anode sheath.

This equation indicates that Hall currents must exist in the anode sheath for it to maintain its radial equilibrium. The Hall currents can be induced, however, only if the anode sheath moves radially inward across the magnetic field lines, i.e.,

$$- J_\theta = \frac{\sigma B_z}{|e| n_I} \left\{(-J_r) + |e| n_I u\right\}$$

From tne above discussions we postulate a model for the accelerator as follows when it is operating in a magnetic field that is initially purely axial and then, at some distance ($z > L$) downstream, is made to diverge.

1. A uniform diameter cathode jet is established which carries only a small fraction of the injected mass flow rate.
2. An annulus of plasma is established off of the anode face. The injected mass is accumulated within this annulus. All of the discharge current passes through the annulus.
3. The average radius of this anode sheath decreases downstream. This causes the ions in the sheath to be accelerated slightly in the axial direction and to be spun up to high azimuthal velocities. The electrons are simultaneously heated, mainly by the ion-electron drag in the azimuthal direction, where the azimuthal electron motion is helping to spin up the ions.
4. The anode sheath eventually meets the cathode jet at $z = L$ and the current path is completed. No discharge current flows at axial positions beyond this point.
5. At positions of $z > L$, the magnetic field acts like a magnetic nozzle. As the field diverges the ions are accelerated axially by two processes:
    a. Conversion of angular momentum requires that as the jet radius increases, rotational ion energy must be transferred to axial and radial kinetic energy.
    b. The high energy electrons tend to expand out of the nozzle ahead of the ions, thus setting up a positive axial electric field that accelerates the ions. In this manner, all of the energy of the particles in the beam can be converted into the kinetic energy of the ions. Obviously, some of this energy will reside in the radial motion with the result that the expansion will not be 100 percent efficient.

An attempt to analyze the "heating" (constant magnetic field) region of such a device is made in Section 4 of this report.

3. INTEGRALS OF THE MOMENTUM EQUATIONS

There are a few cases where the net electromagnetic force in an axisymmetric body can be computed without detailed knowledge of the distributions of current and magnetic field. In the general case, the momentum equations must be integrated simultaneously with continuity, energy, Ohm's laws, Maxwell's equations and the equations of state. The cases chosen here are such that the integrand (force per unit volume) can be put into the form of a divergence, by using Maxwell's equations and simplified momentum equations. These forces can be integrated in terms of total current, radius, and applied magnetic field.

3.1 Pressure Due to $J_z B_\theta$ Pinch

Here the average pressure on the cathode is computed in terms of the current and radius of attachment. The equations used are a momentum equation

$$\frac{dp}{dr} = - J_z B_\theta, \quad p(r=R) = p_o \quad , \tag{1}$$

an induction equation

$$\frac{1}{r} \frac{d}{dr}(rB_\theta) = \mu_o J_z, \quad B_\theta(r = 0) = 0 \quad , \tag{2}$$

a total current integral

$$I = \int_o^R J_z(r)\ 2\pi r\ dr \quad , \tag{3}$$

and a definition of average pressure

$$p_{av} = \frac{1}{\pi R^2} \int_0^R p(r)\ 2\pi r\ dr \tag{4}$$

Combining the above relations, it follows that independent of the distribution of J_z, the average cathode pressure is given by:

$$p_{av} = p_o + \frac{\mu_o I^2}{8\pi^2 R^2} \tag{5}$$

The pressure given by Eq. 5 will act on the cathode to give a thrust. This thrust force is given by $\mu_o I^2/8\pi$ and is independent of the distribution of the current density at the cathode, and of the size of the cathode attachment.

3.2 Thrust Due to $J_r B_\theta$ Pumping

The amount of thrust in an axially symmetric volume due to radial currents and induced azimuthal magnetic field can be evaluated in terms of the magnetic field distribution at the boundaries. This, in turn can be evaluated from the total currents. The following relations are used:

$$\frac{1}{r} \frac{\partial}{\partial r} (r\ B_\theta) = \mu_o\ J_z \tag{6}$$

$$- \frac{\partial B_\theta}{\partial z} = \mu_o\ J_r \tag{7}$$

From Eq.7 it follows that $J_r\ B_\theta = - \frac{\partial}{\partial z} (B_\theta^2/2\mu_o)$

$$\text{Thrust} = \int_0^R \int_{z_1(r)}^{z_2(r)} J_r \, B_\theta \, 2\pi r \, dz \, dr$$

$$= \int_0^R 2\pi r \left[\frac{- B_\theta^2}{2 \mu_o} \right]_{z_1(r)}^{z_2(r)} dr \qquad (8)$$

B_θ can be found by integrating (Eq. 6)

$$B_\theta(r, z) = \frac{1}{r} \int_0^r s \, J_z(s, z) \, ds \qquad (9)$$

Equation 8 shows that thrust can be evaluated in terms of magnetic field and Eq. 9 shows that magnetic field depends only upon axial current. If:

a) Current leaves cylindrical anode of radius R_A

b) current enters circular cathode of radius R_c with uniform current density

then

$$\text{Thrust} = \frac{\mu_o I^2}{4\pi} \left(\frac{1}{4} + \ln \frac{R_A}{R_c} \right) \qquad (10)$$

3.3 Torque Due to $(r J_z B_r - r J_r B_z)$

In an axially symmetric volume with radial and axial currents and magnetic fields, there will be a torque which occurs when the current crosses the magnetic field. To evaluate this torque, introduce the vector potential A_θ.

$$B_r = -\frac{\partial A_\theta}{\partial z} \; ; \quad B_z = \frac{1}{r}\frac{\partial}{\partial r}(r\,A_\theta) \tag{11}$$

The quantity $(r\,A_\theta)$ is constant along a magnetic field line. The torque per unit volume is given by:

$$r\,J_z B_r - r\,J_r B_z = -\left[J_r \frac{\partial\,(r\,A_\theta)}{\partial r} + J_z \frac{\partial\,(r\,A_\theta)}{\partial z}\right] \tag{12}$$

For the axially symmetric case, $\dfrac{\partial\,(r\,A_\theta)}{\partial\theta} = 0$, hence

$$\begin{aligned} \text{Torque} &= -\bar{J} \cdot \nabla\,(r\,A_\theta) \\ &= -\nabla \cdot (r\,A_\theta\,\bar{J}) \end{aligned} \tag{13}$$

where $\nabla \cdot J = 0$ has been used. Upon integration over a volume R of surface S, outward normal $\bar{n}$,

$$\int_R (\text{torque})\; d(\text{vol}) = \int_S (-r\,A_\theta)\;(\bar{J} \cdot \bar{n})\; dS \tag{14}$$

If $r A_\theta$ is constant at anode and cathode

$$\text{Torque} = I\left[(r A_\theta)_{\text{anode}} - (r A_\theta)_{\text{cathode}}\right]$$

$$= I \int_{\text{cathode}}^{\text{anode}} \left[\frac{\partial (r A_\theta)}{\partial r} dr + \frac{\partial (r A_\theta)}{\partial z} dz\right] \qquad (15)$$

$$= \frac{I \text{ (Magnetic Flux Between Cathode and Anode)}}{2\pi}$$

Finally for a point cathode, and an average axial field B_z through a circular anode of radius R_A,

$$\text{Torque} = \frac{1}{2} B I R_A^2 \qquad (16)$$

3.4 Max Thrust Due to $J_\theta B_r$

In an axially symmetric volume where J_θ is induced (by the Hall effect), the amount of axial force cannot be larger than for the case of a completely diamagnetic plasma. In this limiting case, the J_θ lies completely in the surface of the volume, and no magnetic fields exist inside the volume. Compute the currents and magnetic field as follows. Let $B = B_0 + B_1$ where B_0 is the applied field due to external magnets and B_1 is the field due to induced currents within the volume. Outside of the plasma, $\nabla \times B_1$ is zero, hence $B_1 = \nabla \Psi$, where Ψ is a scalar field. Since $\nabla \cdot B_1 = 0$, then

$$\nabla^2 \Psi = 0 \text{ (outside of plasma)} \qquad (17)$$

Since $\bar{B} \cdot \bar{n} = 0$ at the plasma surface

$$\frac{\partial \Psi}{\partial n} = - (\bar{B}_0) \cdot \bar{n} \text{ (at plasma surface)} \qquad (18)$$

Solve Laplace Eq. 17 with boundary condition Eq. 18. The force is given by

$$\text{Force} = - \int \int (\overline{B}_0 + \nabla \Psi)^2 \, \overline{n} \, d \, S$$

where $\overline{n}$ is an outward normal and S is the surface area of the plasma.

The same result can be obtained by the following method. Here we shall attempt to solve for the surface J_θ distribution for a particular plasma configuration shown in Fig. 3-1. We use a θ-Ohm's law (where Ψ_e is the Hall parameter for electrons).

$$J_\theta = - \frac{\Psi_e}{|B|} (J_z B_r - J_r B_z), \tag{19}$$

and the induction equations

$$\frac{\partial B_r}{\partial z} - \frac{\partial B_z}{\partial r} = \mu_o J_\theta \tag{20-a}$$

$$\frac{1}{r} \frac{\partial}{\partial r} (r B_r) + \frac{\partial B_z}{\partial z} = 0 \tag{20-b}$$

In Eq. 19, the coefficient $\frac{\Psi_e}{|B|}$ does not depend upon magnetic field, since Ψ_e is proportional to $|B|$. We assume J_z and J_r are known, based upon visual observations of the operation of the accelerator. It appears that $J_r = 0$, and J_z = total current divided by cross sectional area of the anode jet ($2\pi R_a \delta$). Thus Eq. 19 becomes

$$J_\theta = - \left[\frac{\Psi_e}{|B|} \frac{I_A}{2\pi R_A \delta} \right] B_r \tag{21}$$

From Eq. 21 we see that B_r (and not B_z) is important for calculating J_θ. We can use the integral solution of Eqs. 20-a and 20-b which assumes no magnetic material is present:

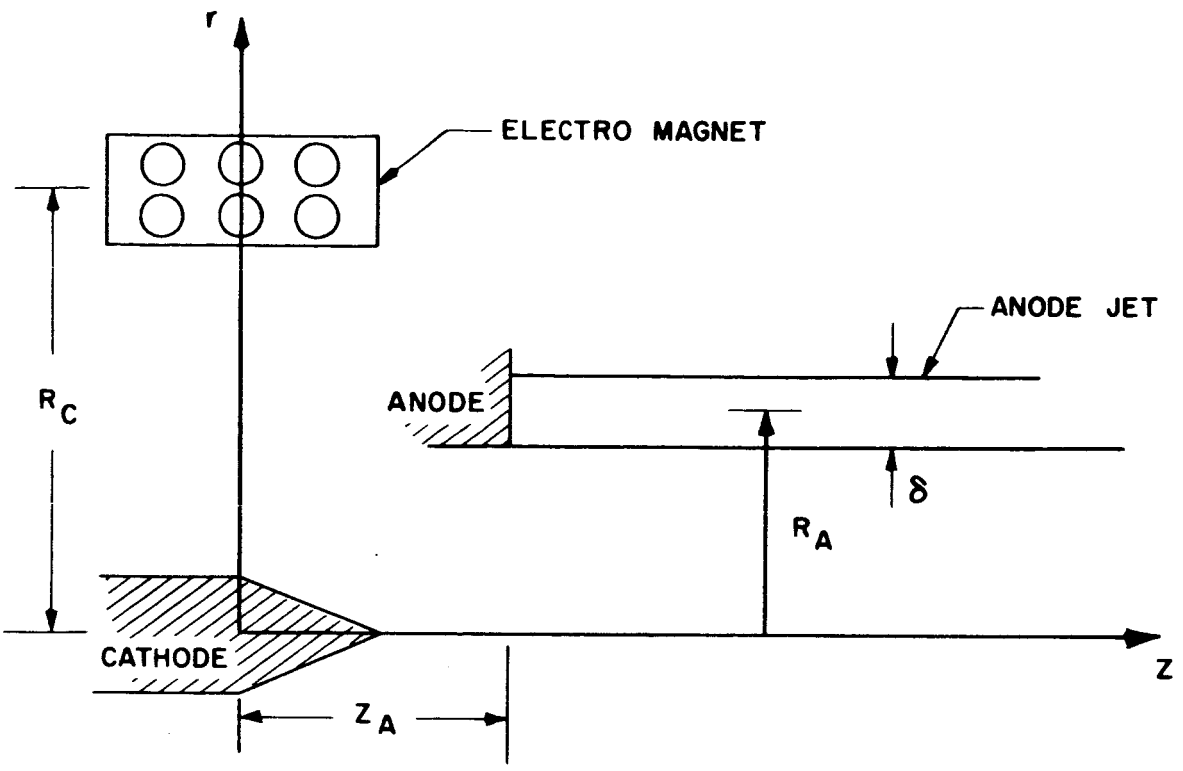

CONTINUOUS MODEL

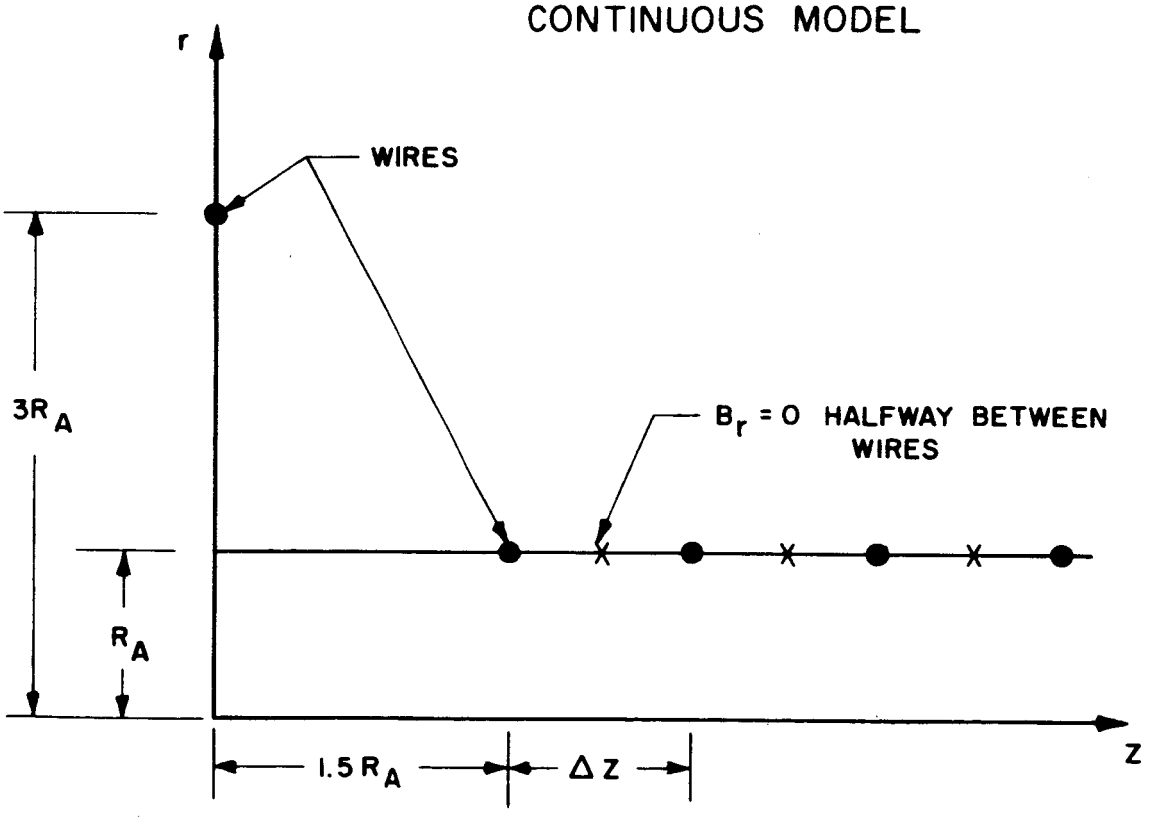

WIRE MODEL

FIG. 3-1 MODELS FOR INDUCED FIELD ANALYSIS

$$B_r(r, z) = \frac{\mu_o}{2\pi r} \iint G(r, s; z-t)\, J_\theta(s, t)\, ds\, dt$$

where

$$G(r, s; z-t) \equiv \int_0^\pi \frac{r\, s\, (z-t)\cos\phi\, d\phi}{\left[r^2 - 2rs\cos\phi + s^2 + (z-t)^2\right]^{3/2}} \qquad (22)$$

When applying Eq. 22, we use Eq. 21 for the value of J_θ in the region of the anode jet, and the known J_θ in the electromagnet. Thus, Eq. 21 becomes:

$$J_{\theta,Hall} = \left[1 - \frac{\Psi_e}{|B|} \frac{I_A}{2\pi R_A \delta}\right] \frac{\mu_o}{2\pi r} \left\{ \iint_{coil} G(r, s; z-t)\, J_{\theta,coil}(s,t)\, ds\, dt + \iint_{anode\ jet} G(r,s,z-t) J_{\theta,Hall}(s,t)\, ds\, dt \right\} \qquad (23)$$

Eq. 23 is an integral equation for the Hall current in the anode jet.

Exact solutions are not available for Eq. 23. An approximate solution has been obtained by lumping the distributed Hall currents J_θ into concentrated currents. We will refer to this technique as the wire model. The Hall currents are replaced approximately by hoop currents in a set of wires. The error of the lumping has been estimated, by changing the number of wires per unit length of the anode jet, and shown to be small.

The solution found was for infinite conductivity, or more precisely $\lambda \to \infty$ where

$$\lambda = \frac{\mu_o \Psi_e I_A}{|B| (2\pi)^2 R_A} = \frac{\mu_o \sigma I_A}{|e| n_I (2\pi)^2 R_A} \qquad (24)$$

This is the limit of a completely diamagnetic plasma.

To solve the wire model, concentrate the current density into a set of wires (see Fig. 3-1). Thus, the wire for the electromagnet coil has a current I_c, where I_c is equal to the number of turns times the current in one conductor. The wires which carry the Hall currents in the anode jet carry a current of $J_{\theta,\,\mathrm{Hall}} \cdot \Delta z \cdot \delta$. The integral Eq. 23 is thus replaced by a set of simultaneous algebraic equations. In the infinite λ case, which corresponds to infinite conductivity, $B_r = 0$. Thus, $(B_r)_j = 0$, where j stands for one of the points shown in the wire model of Fig. 3-1.

$$0 = G(R_A, R_c, z_j)\, I_c + \sum_{i=1} G(R_A, R_A, z_j - z_i)\, I_i \tag{25}$$

Some solutions of Eq. 25 are shown in Fig. 3-2. The Kernel function G defined in Eq. 22 can be computed in terms of elliptic integrals.

$$G(r,s;t) = \frac{2rst}{\left[(r+s)^2 + t^2\right]^{3/2}} \; \frac{(2-k^2)\,E(k) - 2(1-k^2)\,K(k)}{k^2\,(1-k^2)} \tag{26}$$

where E and K are elliptic integrals and $k^2 = 4rs/\left[(r+s)^2 + t^2\right]$. To simplify the computations, a function G_{planar} based upon a flat geometry was used

$$G_{\mathrm{planar}}(r,s;t) = \frac{4r^2\,st}{\left[(r-s)^2 + t^2\right]\left[(r+s)^2 + t^2\right]} \tag{27}$$

This is a good approximation to the Kernel function near the coil.

The electromagnetic thrust can be computed either from the integral of the $J_\theta B_r$ forces in the jet or by the reaction on the coil.

$$\text{Thrust} = \iint_{\text{coil}} J_{\theta,\,\text{coil}}\, B_r\, 2\pi r\, dr\, dz = -\iint_{\text{anode jet}} J_{\theta,\text{Hall}} B_r\, 2\pi r\, dr\, dz \tag{28}$$

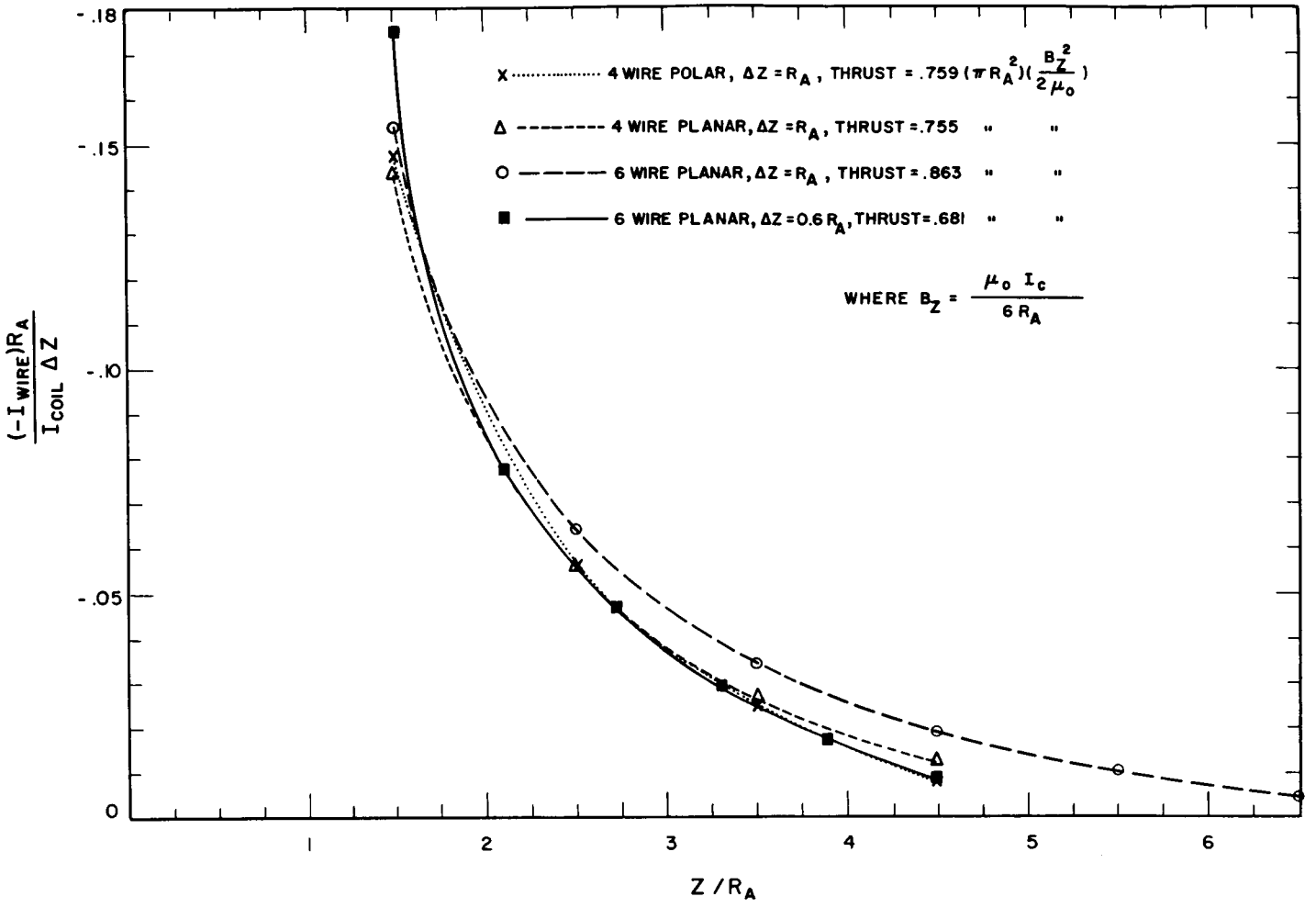

FIG. 3-2 COMPUTED HALL WIRE CURRENTS AND THRUSTS

For the example of Fig. 3-1, the integration was made over the coil. The thrust is approximately 80 percent of the product of the cross-section area of the anode jet times the magnetic pressure which would exist along the centerline if there were no Hall currents. This is probably an upper limit of the possible thrust.

4. ANALYTIC MODELS

The energy exchange and thrust-producing mechanisms in the anode jet are discussed in the following paragraphs. The anode jet is that region downstream from the anode of a Hall current accelerator (which often appears luminous), in which the current is conducted and the plasma accelerated. The anode jet ends when it difuses into the cathode jet.

Figure 4-1 is a sketch of the variables and shape of the anode jet which starts at radius R_o, and has radius $R_j(s)$. The jet has thickness $\delta(s)$. The current density along the jet is $J_s = -I/2\pi R_j \delta$ and the mass flux $\rho w_s = \dot{m}/2\pi R_j \delta$. The azimuthal current will be called J_θ and the velocity V_θ.

Assumptions.

Here a model is proposed and analyzed which the author believes incorporates the dominant features of this zone. There were many assumptions made, which are summarized here:

1. There is a jet and the mass and current flow along this jet. It is annular in shape. Azimuthal currents and velocities also exist. The thickness of the annular region is small compared to its mean radius.
2. The applied magnetic field is purely axial. In a typical accelerator fringing of the applied magnetic field produces radial components. In this analysis the field is axial and the anode jet decreases in radius.
3. There are two major energy sinks. The electrons, which flow back toward the anode, are heated. The ions, which flow away from the anode are given kinetic energy in the form of azimuthal velocity. Ionization is not included, since it is

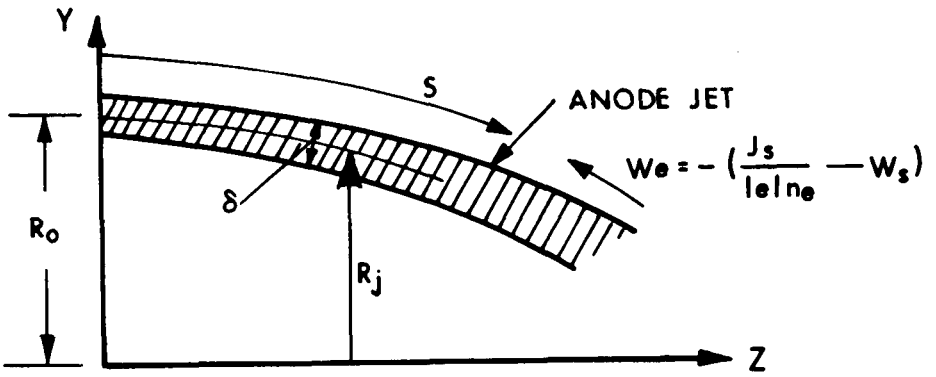

FIG. 4-1 ANODE JET COORDINATES

assumed to occur near the anode and not in the idealized jet. The energy for ionization comes from the heated electrons which leave the jet near the anode end. Internal energy of ions leaving the end of the jet is ineglected. The jet is fully ionized.

4. It is assumed there is no mass entrainment. In a Hall accelerator mass addition to the annular anode jet can come from the inside (gas feed arriving at jet) or outside (entrainment of ambient gas). This analysis applies to an anode-feed device in a hard vacuum.

5. In the analysis which follows, several minimum principles have been used. These are based upon the idea that currents adjust to minimize dissipation. A similar hypothesis has proved to be of great value in developing the theory of conventional arcs. Since this has not been proved for the case where strong magnetic fields exist throughout the discharge, this minimum principle will be treated as an assumption.

4.1 Dissipation

Dissipation is a randomization of energy which occurs with collisions. Electrons pick up energy from the electric field between collisions. Part of this energy is randomized, the rest going to directed kinetic energy. The dissipation (part randomized) per unit volume is $(J_s^2 + J_\theta^2)/\sigma$.

The jet current J_s can be found from the total current.

$$J_s = - I/2\pi R_j \delta \tag{1}$$

The azimuthal current is found from the azimuthal ohm's law

$$J_\theta - \frac{\sigma B}{|e| n_e} J_r = - \sigma B u \tag{2}$$

It follows from the assumed model that $J_r = J_s \frac{dR_j}{ds}$ and $u = W_s \frac{dR_j}{ds}$. The ratio of mass flow to current $\Psi = |e| n_e W_s / J_s = |e| \dot{m}/m_a I$. Hence

$$J_\theta = \frac{1 - \Psi}{\Psi} \sigma B W_s \frac{dR_j}{ds} \tag{3}$$

Integrate the dissipation over the cross section.

$$\frac{J_s^2 + J_\theta^2}{\sigma} 2\pi R_j \delta = \frac{I^2}{(2\pi R_j \delta)\sigma} + \left[\left(\frac{1 - \Psi}{\Psi}\right) B W_s \frac{dR_j}{ds}\right]^2 (2\pi R_j \delta)\sigma \tag{4}$$

Of the two terms, the first is large, if the jet is thin and of low conductivity, and the second is small. On the other hand, if the jet is thick and of high conductivity, the first is small and the second large. If we vary the thickness-conductivity product to minimize this, the dissipation per unit length is given by

$$\frac{J_s^2 + J_\theta^2}{\sigma} 2\pi R_j \delta = -2 \frac{1 - \Psi}{\Psi} B I W_s \frac{dR_j}{ds} \tag{5}$$

The term is positive since dR/ds is negative. The electron internal energy equation is

$$2\pi R \delta n_e (W_e)_s \frac{d}{ds}\left(\frac{3}{2} k T_e\right) = \frac{J_s^2 + J_\theta^2}{\sigma} 2\pi R \delta \tag{6}$$

Here the electron velocity along the jet can be given in terms of the current

$$|e| n_e (W_e)_s = |e| n_e (W_I)_s - J_s = - I(1 - \Psi)/2\pi R_j \delta \tag{7}$$

The resulting electron energy equation can be integrated (W_s = const) to give

$$\left(\frac{3}{2} k T_e\right)_{\text{anode}} - \left(\frac{3}{2} k T_e\right)_{\text{end of jet}} = \frac{2|e| B W_s}{\Psi}\left(R_o - R_j\right) \tag{8}$$

If the temperature of the electrons entering the jet is neglected, the electron temperature in the vicinity of the anode is given by

$$T_e = \frac{4 |e| B W_s}{3 k \Psi} \left(R_o - R_j\right) \tag{9}$$

4.2 Azimuthal Kinetic Energy

Since it is assumed that the anode jet is fully ionized, all kinetic energy is in the ions. The azimuthal momentum equation, integrated over the cross section is

$$\frac{\dot{m}}{R_j} \frac{d}{ds} \left(R_j V_\theta\right) = - B I \frac{dR_j}{ds} \tag{10}$$

This states that the rate of change of angular momentum is due to the rate of current crossing the applied B field (assumed axial). This equation is integrated to give

$$V_\theta(s) = \frac{B I \left[R_o^2 - R_j^2 (s)\right]}{2 \dot{m} R_j(s)} \tag{11}$$

The total power in azimuthal kinetic energy is thus given by

$$\frac{1}{2} \dot{m} V_\theta^2 = \frac{B^2 I^2 \left(R_o^2 - R_j^2\right)^2}{8 \dot{m} R_j^2} \tag{12}$$

Of this energy, part comes directly to the ions from the electric field and part from the electrons due to collisions. It is this transfer from the electrons in the azimuthal direction which may allow the ions to pick up more energy than they get by simply falling through the potential drop. The volume rate of energy transfer is equal to the ion velocity times the drag force. The drag force comes from a different azimuthal velocity for electrons and ions and is given in terms of currents and conductivity.

$$V_\theta \cdot (\text{azimuthal drag}) = V_\theta \cdot \frac{(-|e|\, n_e\, J_\theta)}{\sigma} \tag{13}$$

Use the azimuthal ohm's law (Eq. 3) for J_θ, Eq. 11 for V_θ, then integrate over the volume. That part of the total power in azimuthal kinetic energy which is transferred by the electrons is given by

$$\frac{(1 - \Psi)\, B^2\, I^2}{2\, \dot{m}} \left[R_o^2 \ln\left(\frac{R_o}{R_j}\right) - \frac{\left(R_o^2 - R_j^2\right)}{2} \right] \tag{14}$$

4.3 Power Balance

We can combine the above expressions to get an overall power balance and a power balance for electrons. The electrons enter the anode-ionization region with a temperature given by Eq. 9. They carry an energy of $\frac{5}{2}\, k\, T_e$, at a rate of $I/|e|$. Since the total power dissipated, IV, goes to electron energy at anode and ion energy in azimuthal kinetic energy, we have

$$IV = \frac{10}{3} \frac{B\, I\, W_s}{\Psi} (R_o - R_j) + \frac{|e|\, B^2\, I\, (R_o^2 - R_j^2)^2}{8\, m_a\, \Psi\, R_j^2} \tag{15}$$

The energy given to electrons, $(1 - \Psi)IV$, supplies the electron energy and part of the ion kinetic energy

$$(1 - \Psi)IV = \frac{10}{3} \frac{B\, I\, W_s}{\Psi} (R_o - R_j) + (1 - \Psi) \frac{|e|\, B^2\, I}{4\, m_a\, \Psi} \left[R_o^2 \ln \frac{R_o}{R_j} - \frac{R_o^2 - R_j^2}{2} \right] \tag{16}$$

In Eqs. 15 and 16, the current cancels out and the two expressions for the voltage can be equated. This determines R_j. Unfortunately, the resulting equation cannot be solved explicitly, so values must be computed numerically. If the resulting value of R_j is put in either equation, the voltage V can be computed as a function of Ψ and

(Ma W/|e| B R). These data are presented in Figs 4-2a and 4-2b where $V^* = 9\,|e|\,V/16000\,k\,T_A$ is ploted versus Ψ for several values of $A = 80\,m_a\,W_s/3\,|e|\,B\,R_o$. W_s is taken to be the thermal velocity near the anode.

4.4 Accelerator Performance

It is seen from Fig. 4-2 that V^* possesses a minimum, shown by the dashed line. It is likely that the anode jet will choose a mass flux to minimize the voltage. This gives a Ψ (and also R_j) as a function of A (to minimize V). Hence, the velocity, V_θ, of the ions at the exit of the cathode jet can be found as a function of A.

The thrust can be found from V_θ by assuming that all of the ion energy is converted to thrust through a magnetic nozzle. If we neglect nozzle efficiency,

$$T = \dot{m}\,V_\theta = \frac{B\,I\,(R_o^2 - R_j^2)}{2\,R_j} = T\,(A) \qquad (17)$$

This is shown on Fig. 4-3. A crude approximation of this curve is $T/T_{max} = A$. This approximation gives

$$T \doteq \left(\frac{40}{3}\,\frac{m_a W_s}{|e|}\right) I, \qquad (18)$$

which predicts that the thrust depends linearly upon current and is independent of the magnetic field.

Conclusion.

If the proposed model is valid, the thrust is produced in the anode jet (not cathode jet), and energy is transferred from the fields to the electrons, then to the ions. Thrust is nearly independent of magnetic field and depends linearly upon current.

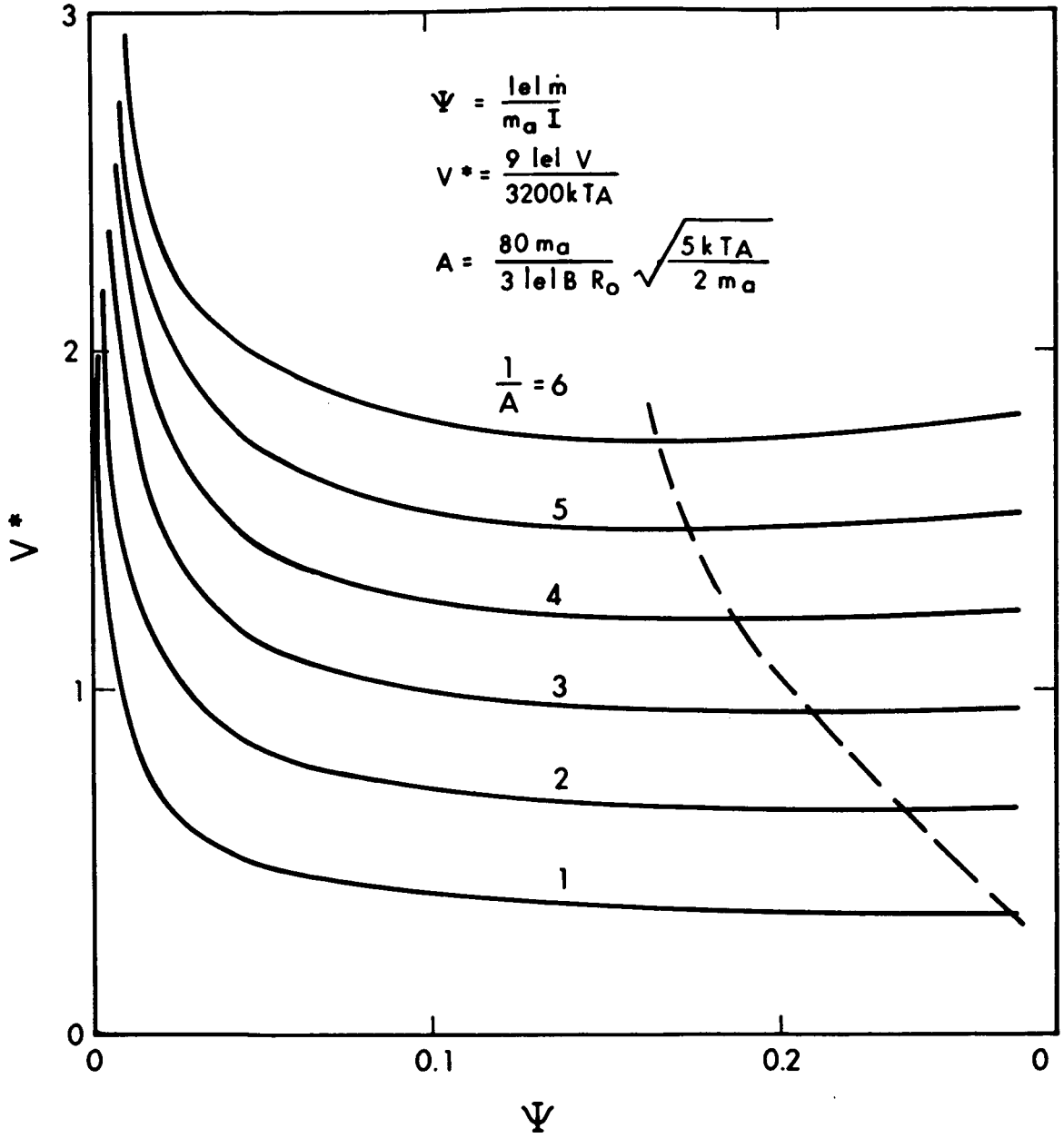

FIG. 4-2a VOLTAGE VERSUS MASS FLOW TO CURRENT RATIO

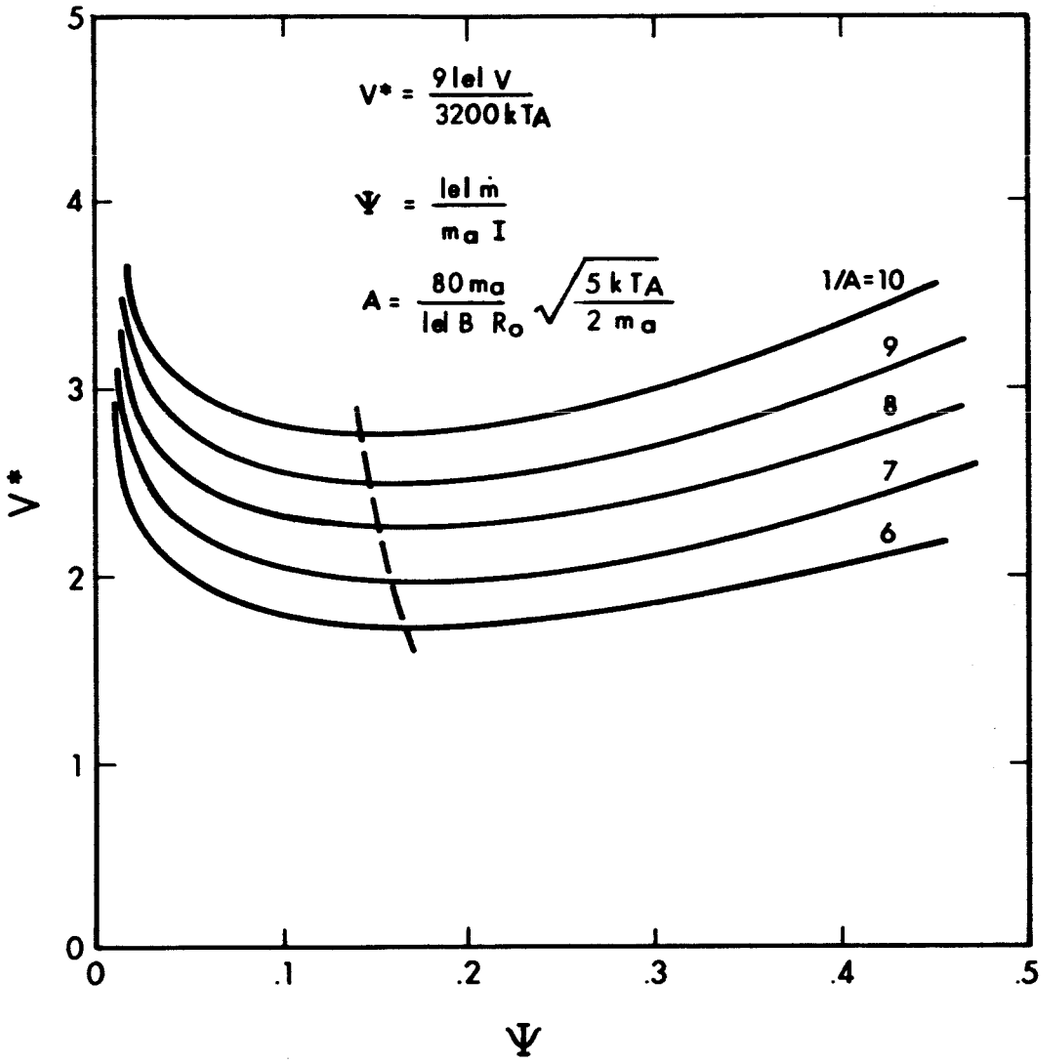

FIG. 4-2b VOLTAGE VERSUS MASS FLOW TO CURRENT RATIO

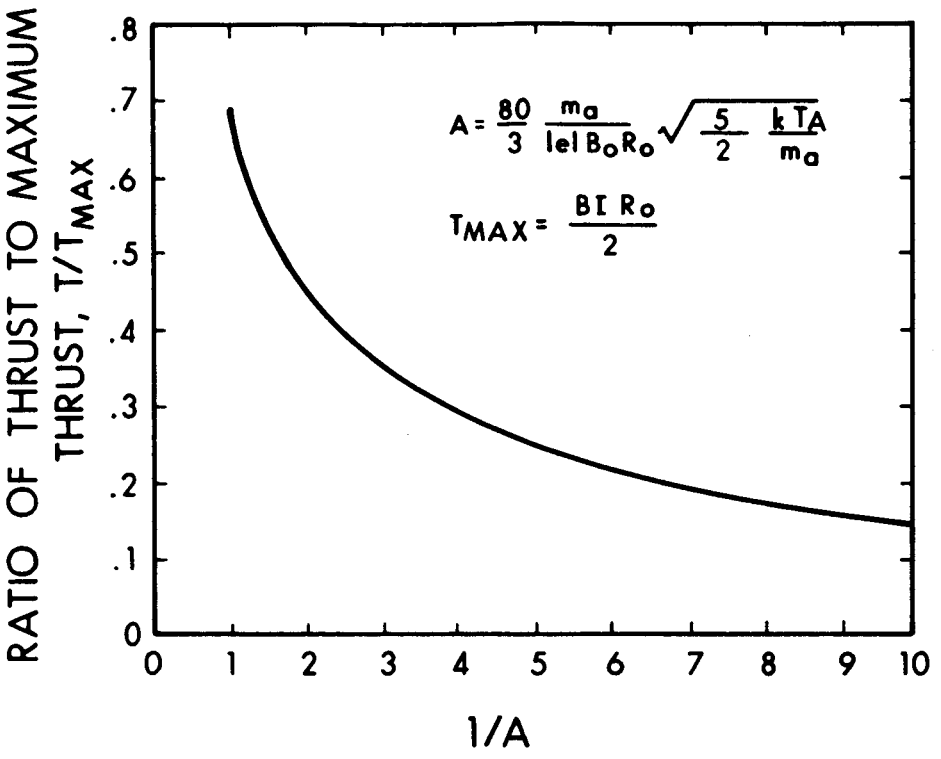

FIG. 4-3 RATIO OF THRUST TO MAXIMUM THRUST, T/T_{MAX}

5. EXPERIMENTAL EQUIPMENT

5.1 Vacuum Facilities

Tests were conducted in two tanks. The alkali metal experiments were conducted in a special facility, built especially for such tests. In this tank it was possible to obtain tank pressures of 10^{-4} mm during the test by water cooling the tank walls and using diffusion pumps. Tests with the gaseous propellants were conducted in a standard 3 foot by 5 foot tank that was water cooled. The mechanical vacuum pumps had a maximum capacity of 5000 cfm and hence could only maintain ambient tank pressure of 20 to 180μ during the tests reported.

The gas flow rate was measured by using calibrated sonic orifices. These had an inherent accuracy of better than ± 3 percent with the pressure gauges which were used.

5.2 Feed Systems

Two types of feed systems were used with the alkali metals. A vapor feed system was used initially and attempts were made to determine the mass flow rate by measuring the liquid temperature in the boiler. The flow rate was controlled by passing the vapor through a sonic orifice which was maintained at a temperature higher than that of the liquid. Because of the extreme sensitivity of the vapor pressure to small changes in the temperature of the liquid it was not possible to obtain accurate flow rate data using this boiler. A liquid feed system was used to obtain the data on sodium reported in Section 6. A full description of the feed system can be found in Ref. 2.

The thrust was measured using thrust balances developed previously (see Refs. 1 and 2) -A discussion of the calibration and probable errors of such a thrust measuring device is given below.

5.3 Thrust Stand Calibration for a Hall Current Accelerator

The complete investigation of Hall current accelerating mechanisms might make necessary the measurement of local values of momentum flux or velocity, as well as the individual reactions on the magnet and electrodes. However, the much more reliably measurable total momentum input to the exhaust stream of a propulsion device provides much useful information and is a valid measure of performance for mission analysis. The total momentum input or thrust is most accurately determined by mounting the entire accelerator, plus the magnet assembly, on a thrust dynamometer. Correct interpretation of thrust stand data requires consideration of the following extraneous forces which would not provide acceleration in space:

1. Interaction of magnetic field coil with tank and fixed current leads.
2. Interaction of applied accelerator current with tank and fixed current leads.
3. Interaction of Hall currents with tank and fixed current leads.

The first two of these interactions can be directly calibrated by shorting the electrodes of the accelerator, applying full magnet and arc current, and noting the indicated thrust. This is routinely done after each change of accelerator, magnet or power lead configuration in the tests performed at EOS and was done before the tests performed at the Lewis Research Center (Ref. 3).

The third interaction is difficult to calibrate because of the lack of detailed information about the distribution and magnitude of the Hall currents which flow in the plasma whan the accelerator is in operation. However the error caused by this type of interaction can be shown to be negligible. The discussion presented in Subsection 2.1 of the First Quarterly Report of the present contract (Ref. 4) indicated that when the field induced by the Hall currents is comparable to the applied field, the thrust is approximately given by

$$T = 0.8A \frac{B_o^2}{2\mu_o} \quad (1)$$

where T is thrust in newtons, μ_o is permittivity of free space ($4\pi \times 10^{-7}$ henries/m), B_o is the undisturbed field strength in webers/m^2 along the center line of the magnet coil, and A is the exit area of accelerator in m^2. The value given in Eq. 1 is an estimate of the upper limit on the thrust and is obtained when the induced currents are sufficient to completely exclude the applied magnetic field from the plasma (infinite conductivity approximation).

For typical test conditions of the 10-kW hydrogen accelerator, the following values are appropriate:

$T \approx 6$ grams force ≈ 0.06 newtons

$B_o \leq 3000$ gauss $= 0.3$ webers/m^2

$A = 10^{-4}$ m^2

Insertion of these values in Eq. 1 gives a thrust of approximately 3 newtons (300 grams force). Since the magnet current is kept constant during a test, the applied field strength remains constant and the ratio of the induced field to the applied field will be of the same order as the ratio of the actual thrust to a thrust of 3 newtons (typically 0.02).

Next, the effect of discharge geometry on the thrust interaction must be estimated. The field produced by a solenoidal current distribution decreases with roughly the third power of distance and increases with roughly the second power of the radius of the distribution for distances of the same order or greater than the length of the distribution. Since the field coil and the Hall current loops are at essentially the same distances from the tank, fixed supports, and the fixed current leads, and since the diameters of the Hall current loops are about the same as or smaller than the mean coil diameter, there seems to be no possibility that geometric factors would make the effect of the induced fields more important than that of the applied fields.

Since the thrust interaction with the tank and fixed current leads depends upon the second power of the total field strength,

$$\text{interaction} \propto B_{total}^2 = (B_o - B_{Hall})^2 = B_o^2 \left(1 - \frac{2B_{Hall}}{B_o} + B_{Hall}^2\right) . \qquad (2)$$

With B_{Hall}/B_o of the order of 0.02, it can be seen that the Hall currents make a small contribution to the calibration of the thrust stand.

Therefore, it may be concluded that the change in thrust stand calibration caused by the interaction of the Hall currents with the tank and fixed current leads can be neglected whenever the observed thrust is small compared to the product of the exit area of the accelerator and the center-line magnetic pressure of the undisturbed, applied magnetic field.

6. EXPERIMENTAL RESULTS

6.1 Tests of H_2-I Accelerator

The H_2-I accelerator design is shown in Figs. 6-1 and 6-2. The accelerator has a tungsten cathode tip mounted on a water cooled copper base and a water-cooled anode with an inner bore 1.5 cm in diameter and 0.5 cm long. The anode and cathode are separated by a boron nitride insulator which has six equally spaced ports through which the hydrogen expellant is introduced. In the first version of H_2-I, the anode had a tungsten insert as shown in Fig. 6-1. The completely copper anode shown in Fig. 6-2 was used in later versions.

The design shown in Fig. 6-1 was found to have inadequate spacing in the axial direction between the anode and cathode. Under some conditions this caused the discharge to strike directly between the electrodes in the direction of the applied magnetic field. The problem was successfully eliminated in the later version shown in Fig. 6-2 by reducing the cone angle and diameter of the cathode and arranging the boron nitride insulator to prevent direct arcing along the magnetic field.

Tests were performed with the H_2-I accelerators over the power range from 40 to 102 kw with mass flow rates of from 0.006 to 0.05 grams/sec, arc currents from 500 to 1000 amperes, magnet coil currents from 500 to 2000 amperes and ambient pressures from 0.02 to 4.5 mm Hg. The most pertinent data obtained with the H_2-I accelerator are presented in Table 6-I and in Figs. 6-3 through 6-16.

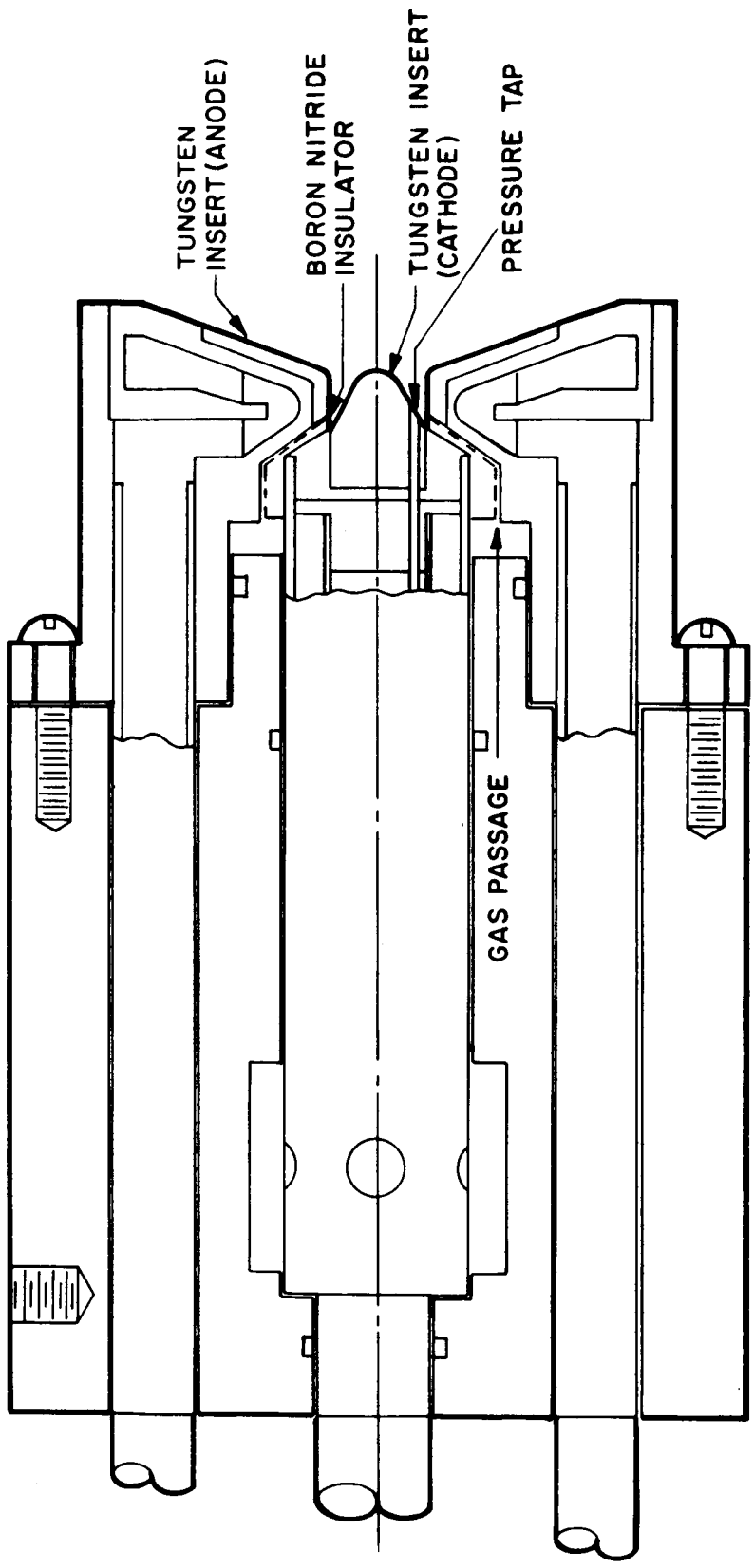

FIG. 6-1 SCHEMATIC OF ACCELERATOR H_2-I WITH TUNGSTEN LINED ANODE

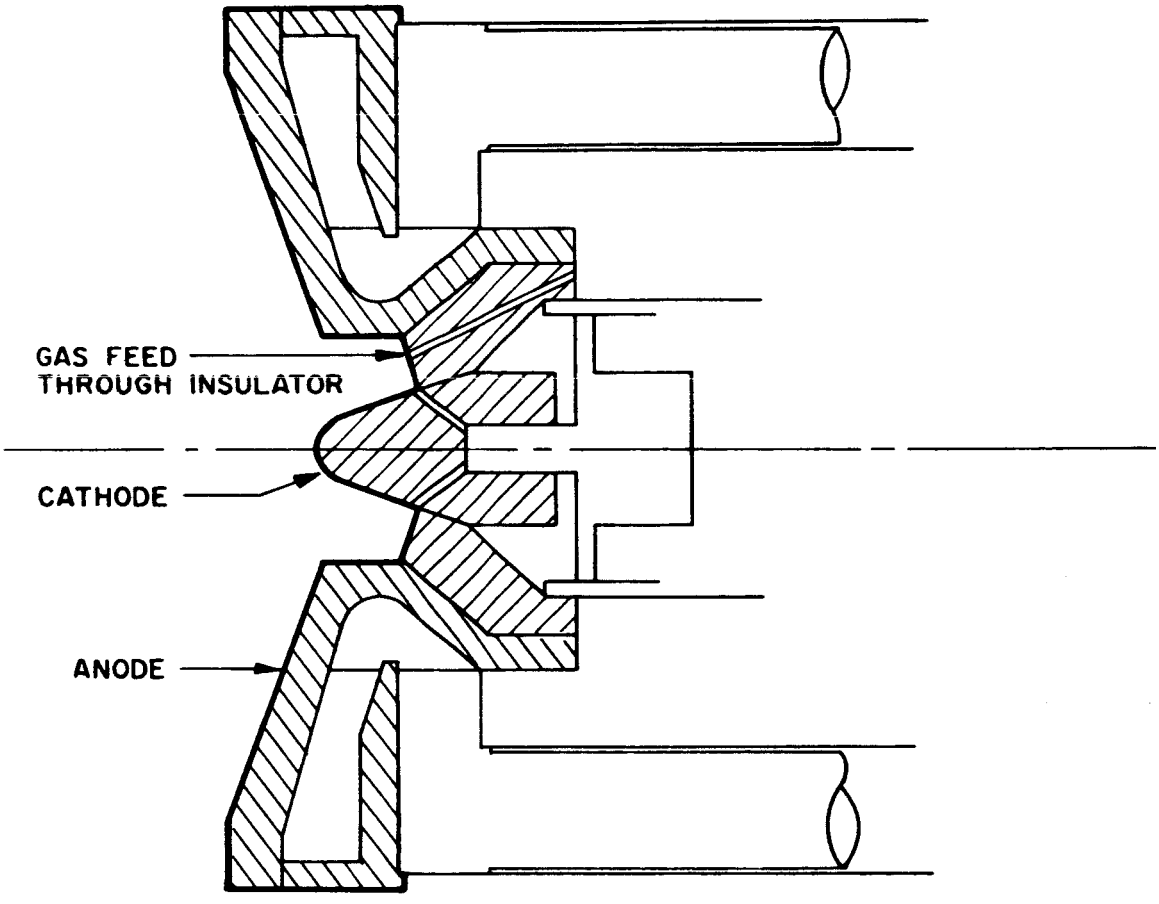

FIG. 6-2 HALL CURRENT ACCELERATOR WITH NO TUNGSTEN ANODE INSERT (H_2-I)

TABLE 6-I

PERFORMANCE DATA FOR HALL CURRENT ACCELERATOR H_2-I WITH HYDROGEN EXPELLANT

I_C amps	I_A amps	P_{arc} kw	P_{an} kw	P_{cath} kw	Mass Flow gr/sec	Tank Pressure mm Hg.	Arc Chamber Pressure mm Hg.	Thrust grams	I_{sp} seconds	η_b	η_{th}
1800	600	60.0	16.2	1.02	0.019	0.070	3.3	59.4	3130	.149	.714
1800	600	60.6	15.7	0.87	0.018	0.135	3.3	62.3	3460	.171	.728
1800	600	62.4	15.8	0.75	0.017	0.260	4.4	63.3	3720	.181	.735
1800	600	62.7	15.5	0.81	0.02	0.650	5.1	49.4	2470	.093	.741
1800	600	65.4	16.3	1.02	0.02	4.50	8.2	34.4	1720	.043	.736
1800	700	82.6	31.2	1.47	0.006	0.230	2.4	66.4	11100	.43	.605
1800	800	85.6	21.7	1.44	0.01	0.310	3.4	85.6	8560	.41	.730
1800	600	62.2	16.9	0.84	0.0146	0.145	3.0	56.9	3900	.17	.715
1800	600	58.8	14.3	0.81	0.02	0.145	3.6	59.5	2980	.14	.744
1800	600	58.2	12.8	0.81	0.029	0.145	4.3	63.8	2180	.12	.768
1800	600	59.1	12.3	0.75	0.041	0.145	5.2	67.8	1650	.09	.780
1800	400	38.2	9.6	0.62	.02	.135	2.90	37.5	1875	.088	.732
1800	500	48.0	11.6	0.71	.02	.140	2.99	49.8	2490	.124	.743
1800	700	64.4	17.4	1.09	.02	.140	5.23	66.6	3330	.165	.714
1800	800	74.6	19.6	1.30	.02	.135	5.79	78.1	3905	.196	.720
1800	900	88.7	22.1	1.65	.02	.135	6.07	92.5	4625	.232	.731
500	600	48.6	--	--	0.02	--	--	46.1	2310	.105	--
600	600	48.9	14.8	0.80	0.02	.150	2.89	49.0	2700	.118	.683
800	600	48.7	13.5	0.83	0.02	.145	2.52	59.4	3080	.174	.708
1000	600	51.3	13.7	0.83	0.02	.145	2.61	61.5	3180	.142	.717
1200	600	53.4	13.8	0.77	0.02	.140	2.89	63.5	3230	.145	.728
1400	600	55.2	13.9	0.77	0.02	.140	2.99	64.5	3210	.146	.735
2000	600	60.6	14.8	0.77	0.02	.140	3.55	58.9	2950	.137	.747

The tests were performed by varying one of the four variables of arc current, magnet current, ambient pressure, and mass flow, while keeping the other three constant. Because the mass flow rate has an effect on the tank pressure, tank pressure was maintained during the variable mass flow rate tests by bleeding cold H_2 into the downstream end of the tank. As a function of the above independent variables the following dependent variables were measured: thrust (total reaction on accelerator plus magnet assembly); arc voltage; magnet voltage; power absorbed by cooling water circuits of the anode, cathode, magnet, thrust balance structure, and tank walls; and arc chamber pressure (see location of taps in Fig. 6-2).

The power absorbed by the cathode was between 0.7 and 1.65 kW over the range of conditions tested. There was a definite trend in the data indicating that energy loss at the cathode increases at least linearly with current and is independent of magnetic field over the ranges tested. Though both the mass flow rate and tank pressure appear to affect cathode energy transfer, no simple correlation was evident from the data.

The arc chamber pressure measured at the base of the cathode is plotted as a function of each of the independent variables in Figs. 6-3 through 6-6. The cathode pressure seemed to increase slightly with applied magnetic field strength (Fig. 6-3) and linearly with ambient pressure (Fig. 6-4). It increased almost exactly as the square root of the mass flow rate (Fig. 6-5). The effect of arc current on cathode pressure is shown in Fig. 6-6. The arc chamber pressures observed in H_2-I were smaller by about a factor of ten than those found in an earlier accelerator which had the cathode tip set back 1-cm from the exit plane of the arc chamber. The arc attachment at the anode was visually observed to be on the downstream face of the anode rather than within the arc chamber. The slight anode erosion on the downstream surface during operation at high arc current and low mass flow rate confirmed that the anode attachment was outside the arc chamber. Thus it appeared that only a small amount of energy

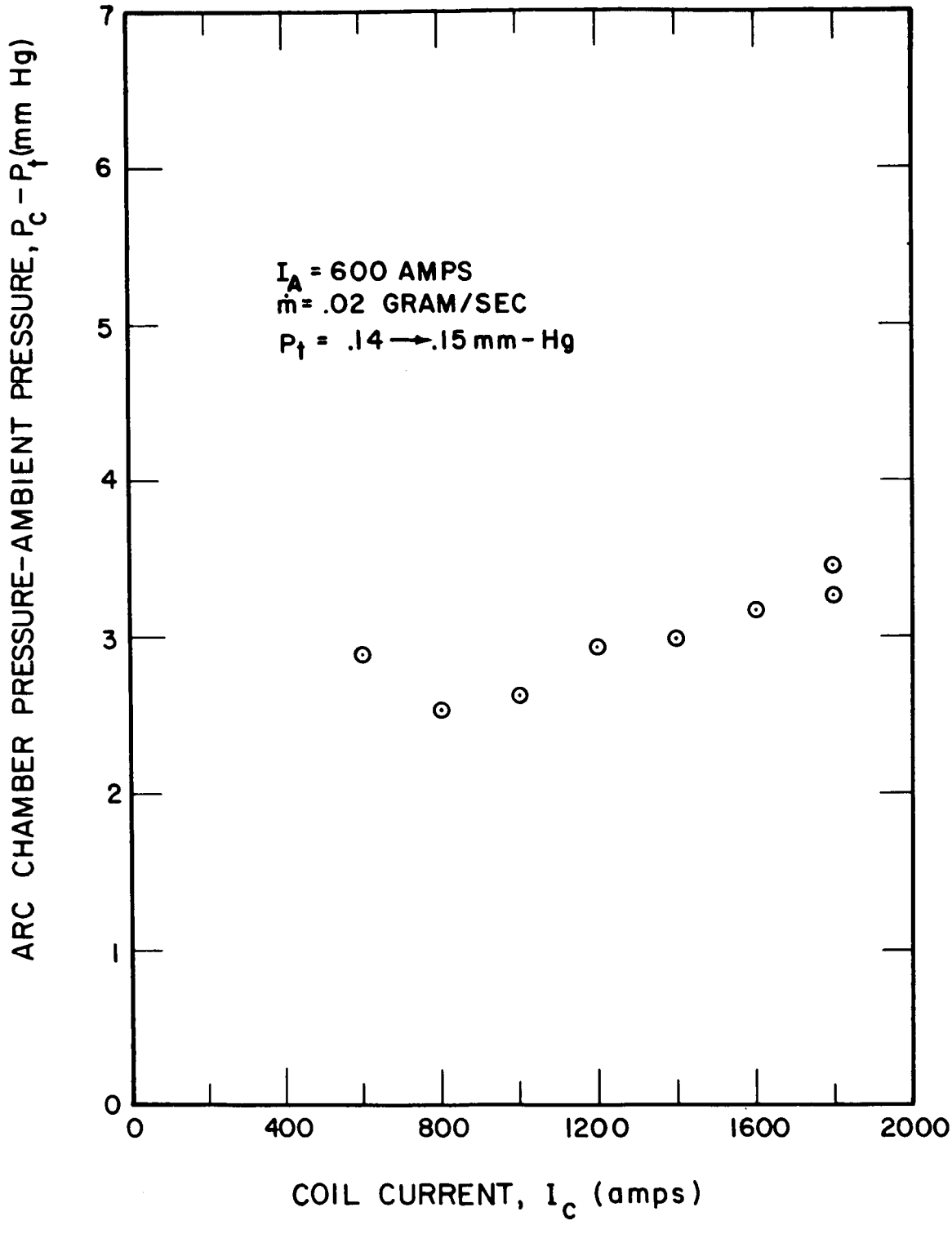

FIG. 6-3 ARC CHAMBER PRESSURE VERSUS COIL CURRENT FOR ACCELERATOR H_2-I

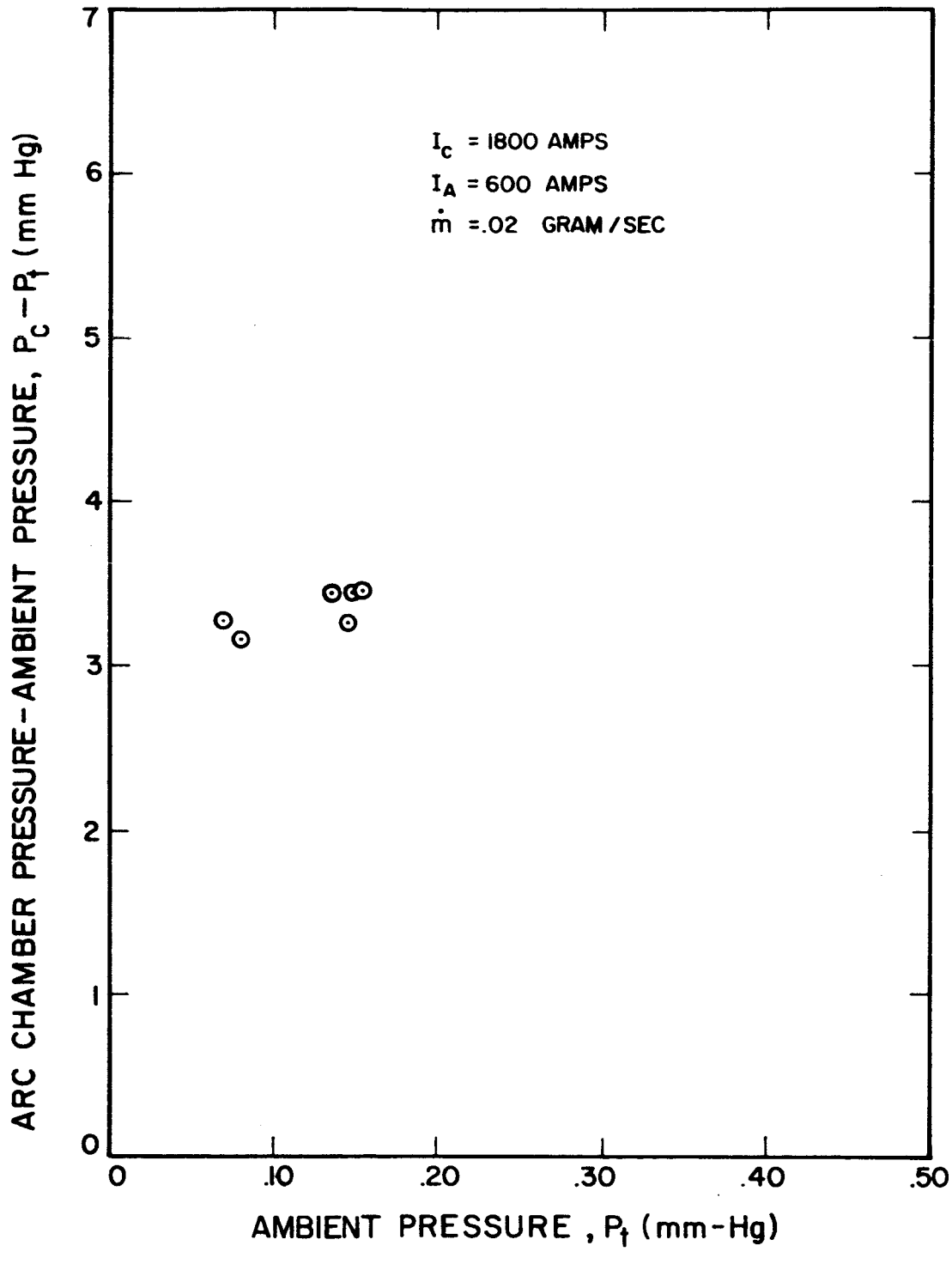

FIG. 6-4 ARC CHAMBER PRESSURE VERSUS AMBIENT PRESSURE FOR ACCELERATOR H_2-I

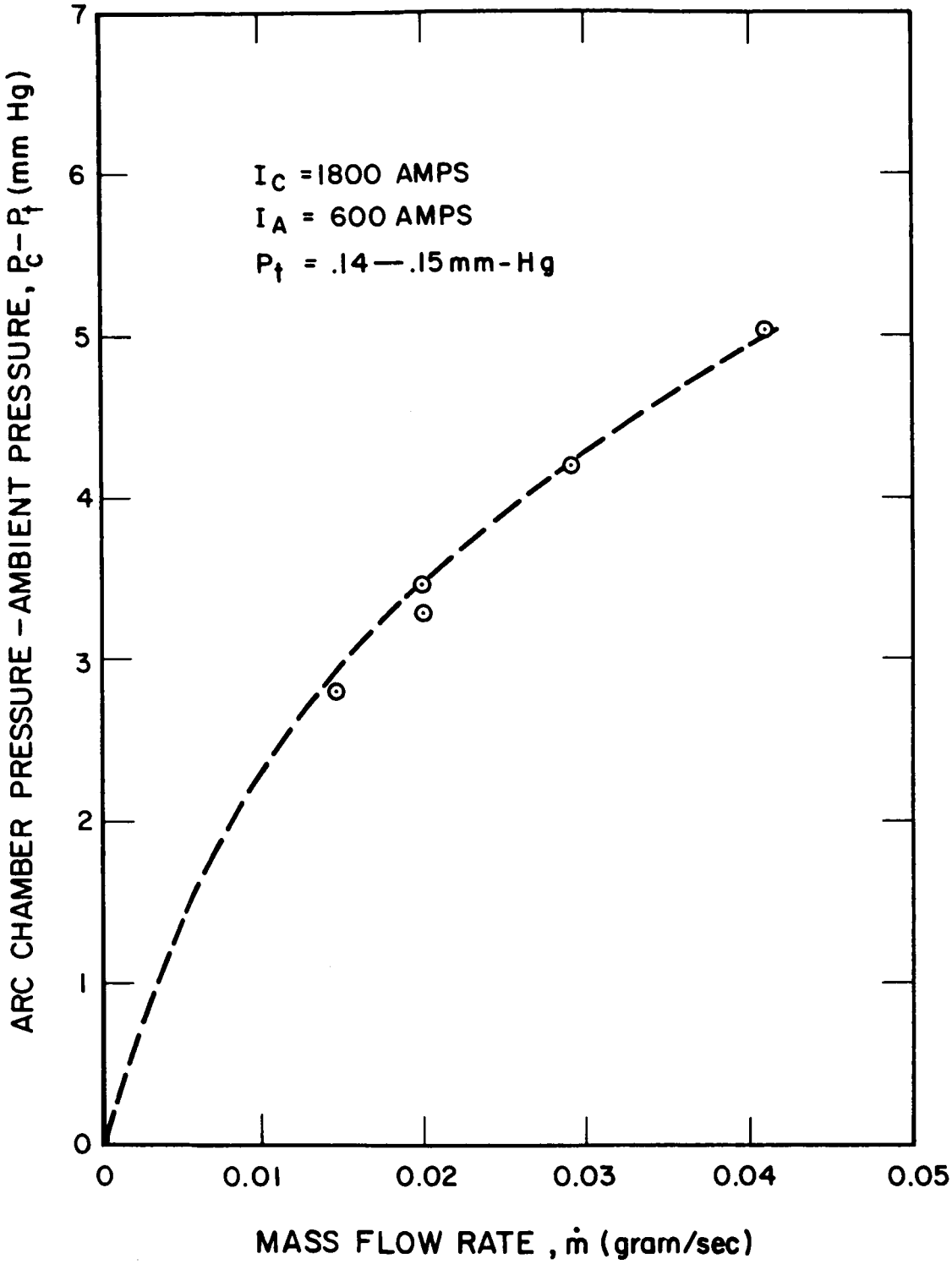

FIG. 6-5 PRESSURE AT CATHODE VERSUS MASS FLOW RATE FOR THE H_2-I ACCELERATOR

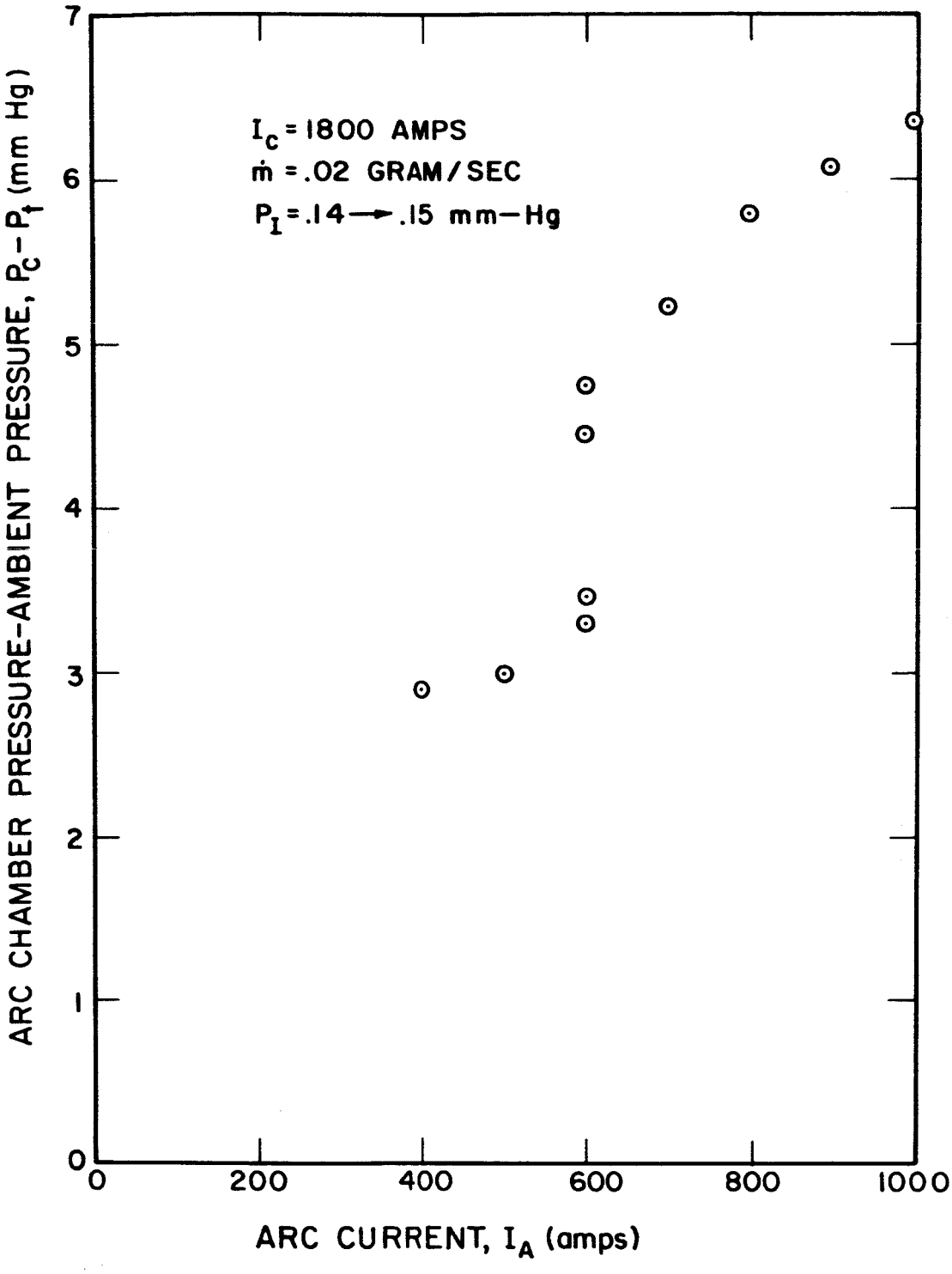

FIG. 6-6 ARC CHAMBER PRESSURE VERSUS ARC CURRENT FOR ACCELERATOR H_2-I

was transferred to the gas in the arc chamber. If the gas flow is assumed to be sonic at the exit plane of the arc chamber, the mass flow rate would be related to the exit static temperature and the stagnation pressure of the flow by a relation of the form:

$$\dot{m} = \frac{(A_{exit})\ p_o}{\sqrt{T_{exit}}}\ 7.7 \times 10^{-3}\ \left[\text{m.k.s}\right] \qquad (1)$$

Though the constant in Eq. 1 depends upon the degree of dissociation and ionization, the specific heat ratio, and the assumption of frictionless, constant area flow with heating, its numerical value is practically constant for most situations. For a typical test with H_2-I, Eq. 1 leads to:

$$T_{exit} = \left[\frac{(A_{exit})\ (p_o)\ 7.7 \times 10^{-3}}{\dot{m}}\right] = 1200\ ^{o}K \qquad (2)$$

The low exit temperature is in accord with other indications that little energy was transferred to the gas in the arc chamber.

The dependence of arc chamber pressure on the square root of $\dot{m}$ indicates that if the flow is sonic at the exit plane then the exit plane temperature varies inversely with $\dot{m}$. The applied magnetic field strength may be expected to have only a small effect on arc chamber pressure when the arc attaches to the downstream surface of the anode. The exit plane temperature can be expected to increase with the arc current, leading to a dependence of arc chamber pressure on current similar to that observed in Fig. 6-6. The irregularity of the curve in Fig. 6-6 may be associated with changes in the choking condition. The effect of ambient pressure on arc chamber pressure is probably also associated with changes in the choking condition at the exit plane and to some effect on the boundary layer thickness in the arc chamber. Because of the lack of a more precise model of the aerodynamics of the arc chamber, these qualitative conclusions are regarded as only tentative explanations of the observed data.

The power absorbed by the anode was determined calorimetrically and is plotted as a function of the independent variables in Figs. 6-7 through 6-10. The effects of magnetic field strength and tank pressure on anode heat transfer are seen to be slight in Figs. 6-7 and 6-8, except possibly at very low field strengths and pressures. The anode power loss is seen to be proportional to the current in Fig. 6-9 and to vary inversely approximately as the square root of the mass flow rate in Fig. 6-10. All four of these trends are what would be expected on the basis of convective heat transfer being the dominant mechanism for power loss to the anode. Previous correlations have indicated that some relation like

$$\frac{P_A - \Phi I}{I V} \approx \left(\frac{A \mu_{f.s.}}{\dot{m} d} \right)^n = Re^{-n}$$

exists between the power absorbed by the anode, P_A, and the free stream Reynold's number of the gas. The exponent n was found to lie between 1/2 and 1/3. As seen in Figs. 6-7 through 6-10, this expression well predicts all of the observed trends. However, it has not been possible to establish accurate values for the free stream gas viscosity $\mu_{f.s.}$ as yet, so no check on the absolute value of the relation between the "Stanton number", $\frac{P_A - \Phi I}{I V}$, and the "Reynolds number", $\frac{\dot{m} d}{A \mu_{f.s.}}$, can be made. The fact that the best correlation was based upon the total gas enthalpy, i.e., $\dot{m} \times I \times V$ conflicts to some extent with our present interpretation of the heat transfer mechanisms in the discharge. Attempts to resolve this problem are presently being made.

The thrust produced by the accelerator is plotted as a function of the independent variables in Figs. 6-11 through 6-14. It was found that the thrust increased linearly with applied current (Fig. 6-11), was essentially independent of mass flow rate (Fig. 6-12),

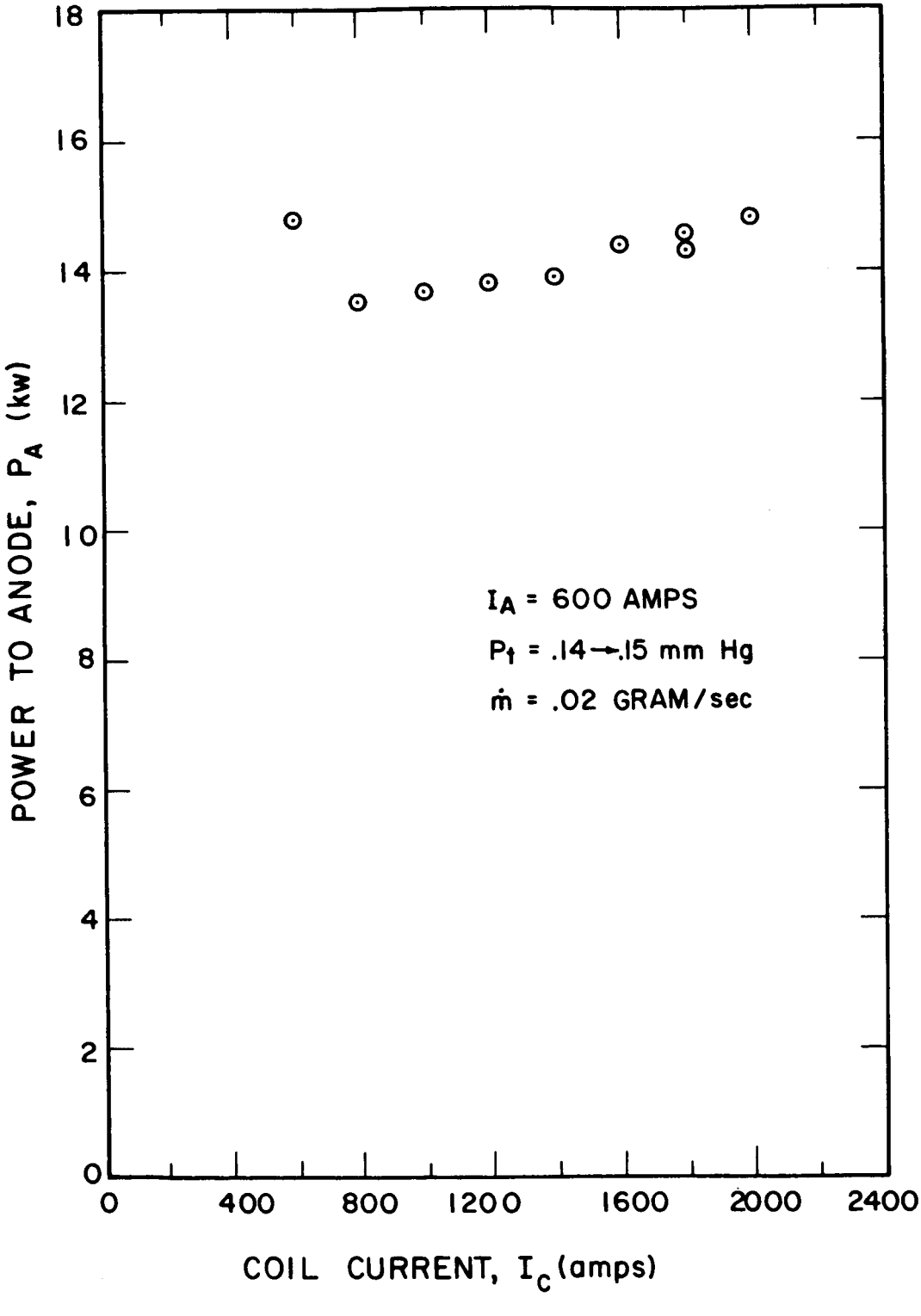

FIG. 6-7 POWER TO ANODE VERSUS COIL CURRENT FOR ACCELERATOR H_2-I. CENTERLINE FIELD ABOUT 3000 GAUSS AT I_c = 1800 AMPS

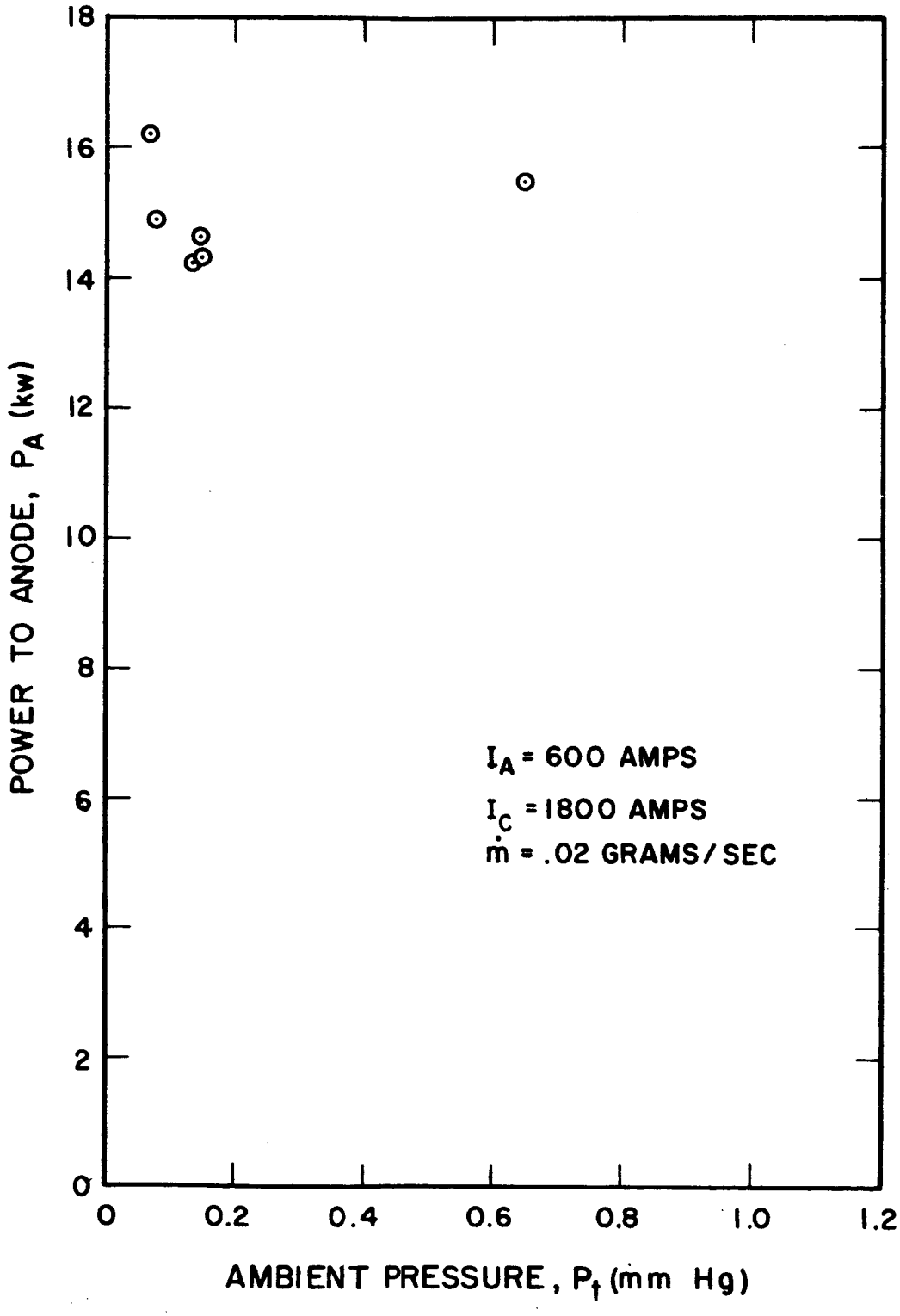

FIG. 6-8 POWER TO ANODE VERSUS AMBIENT PRESSURE FOR ACCELERATOR H_2-I

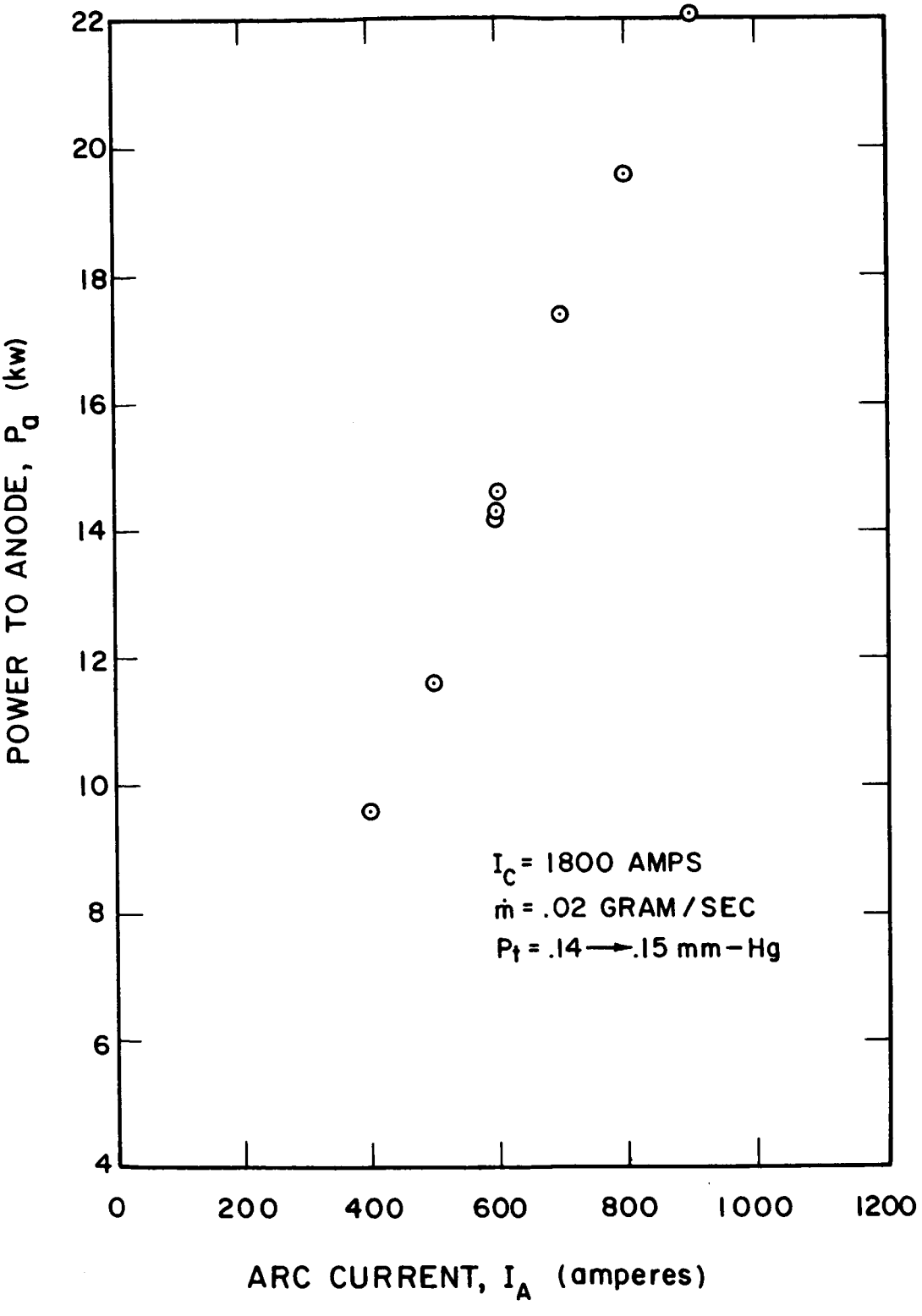

FIG. 6-9 POWER TO ANODE VERSUS ARC CURRENT FOR ACCELERATOR H_2-I

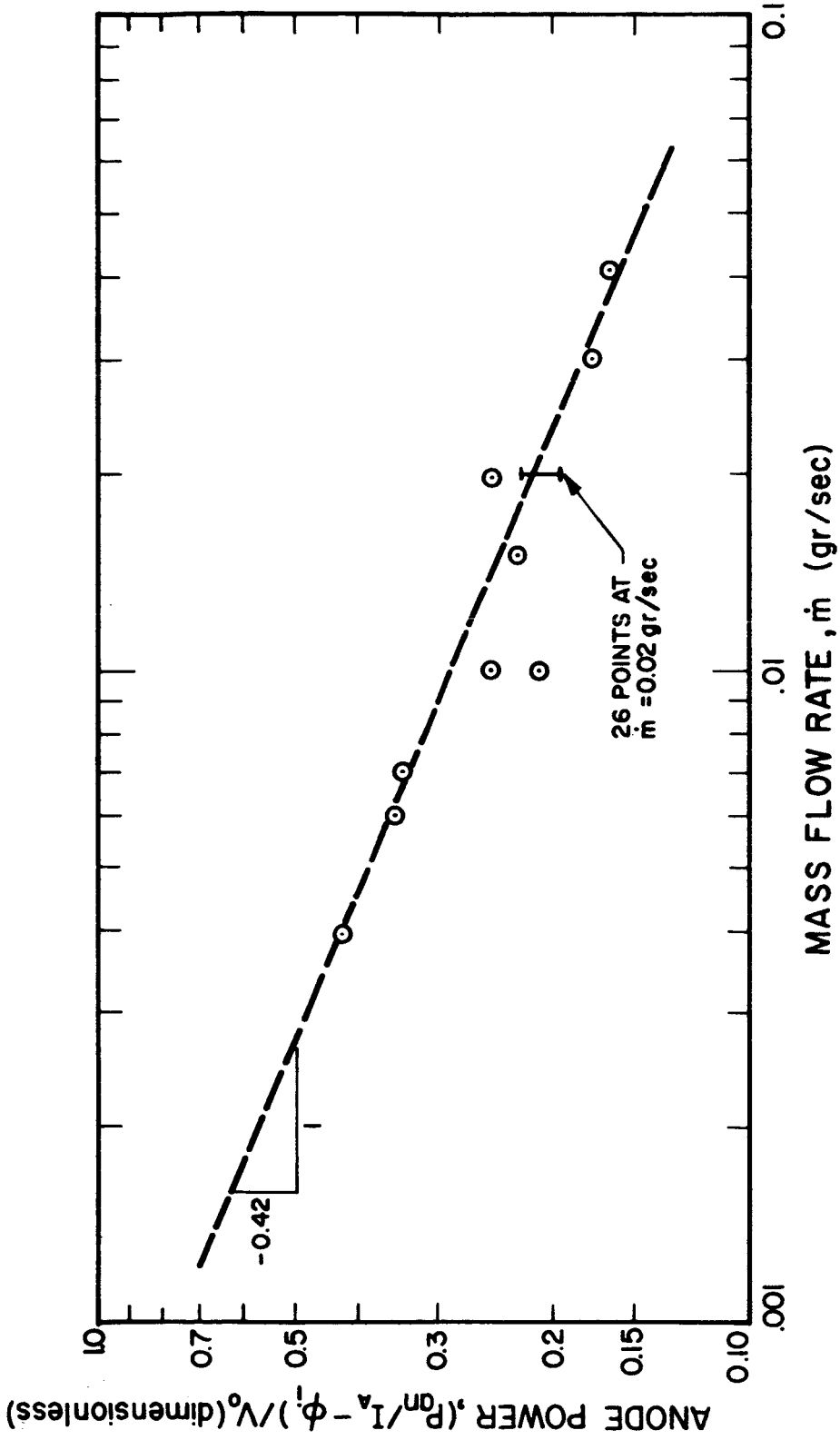

FIG. 6-10 ANODE POWER VERSUS MASS FLOW RATE FOR ACCELERATOR H_2-I. NOTE LOGARITHMIC SCALES

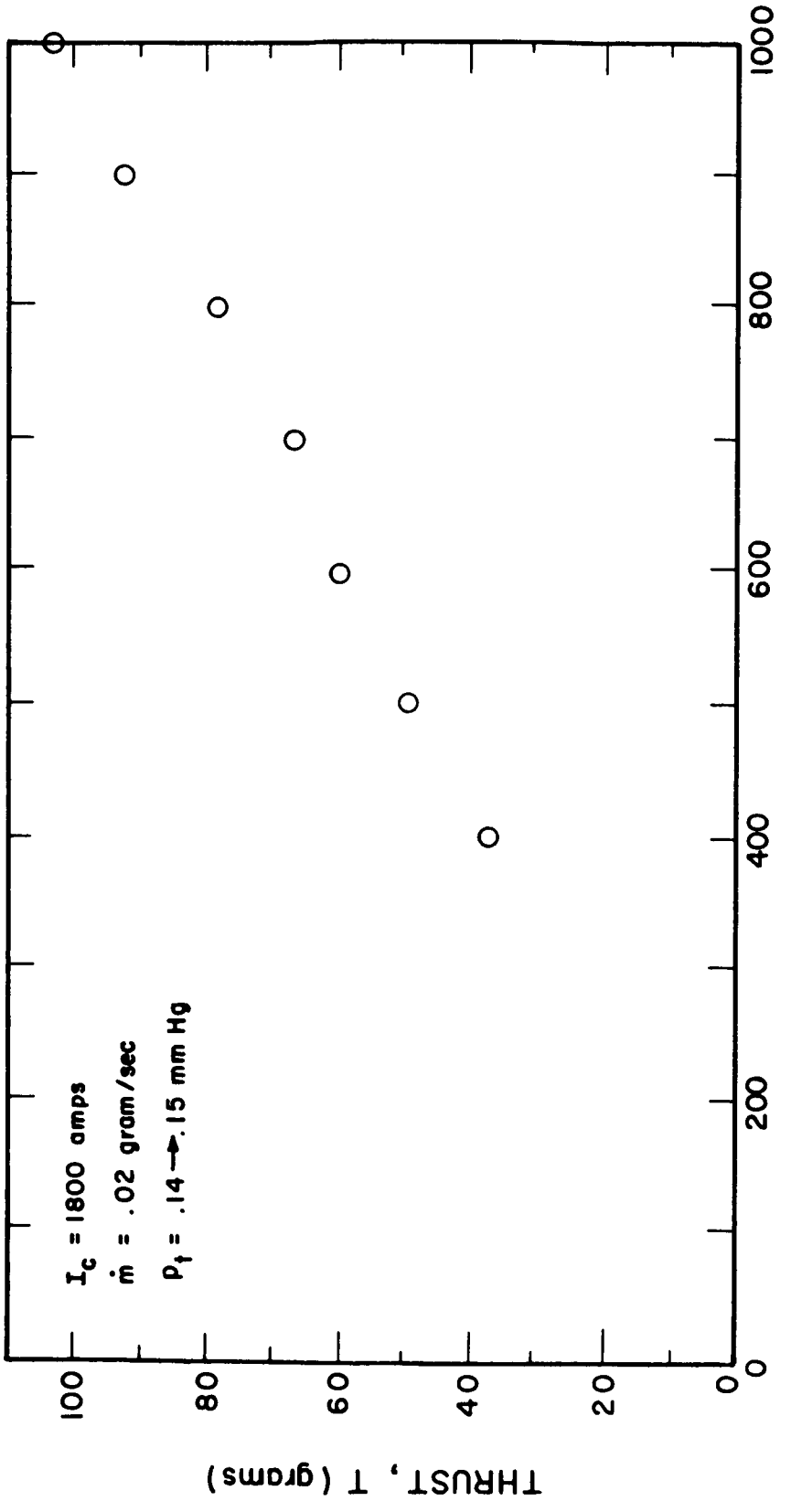

FIG. 6-11 THRUST VERSUS ARC CURRENT FOR ACCELERATOR H_2-I

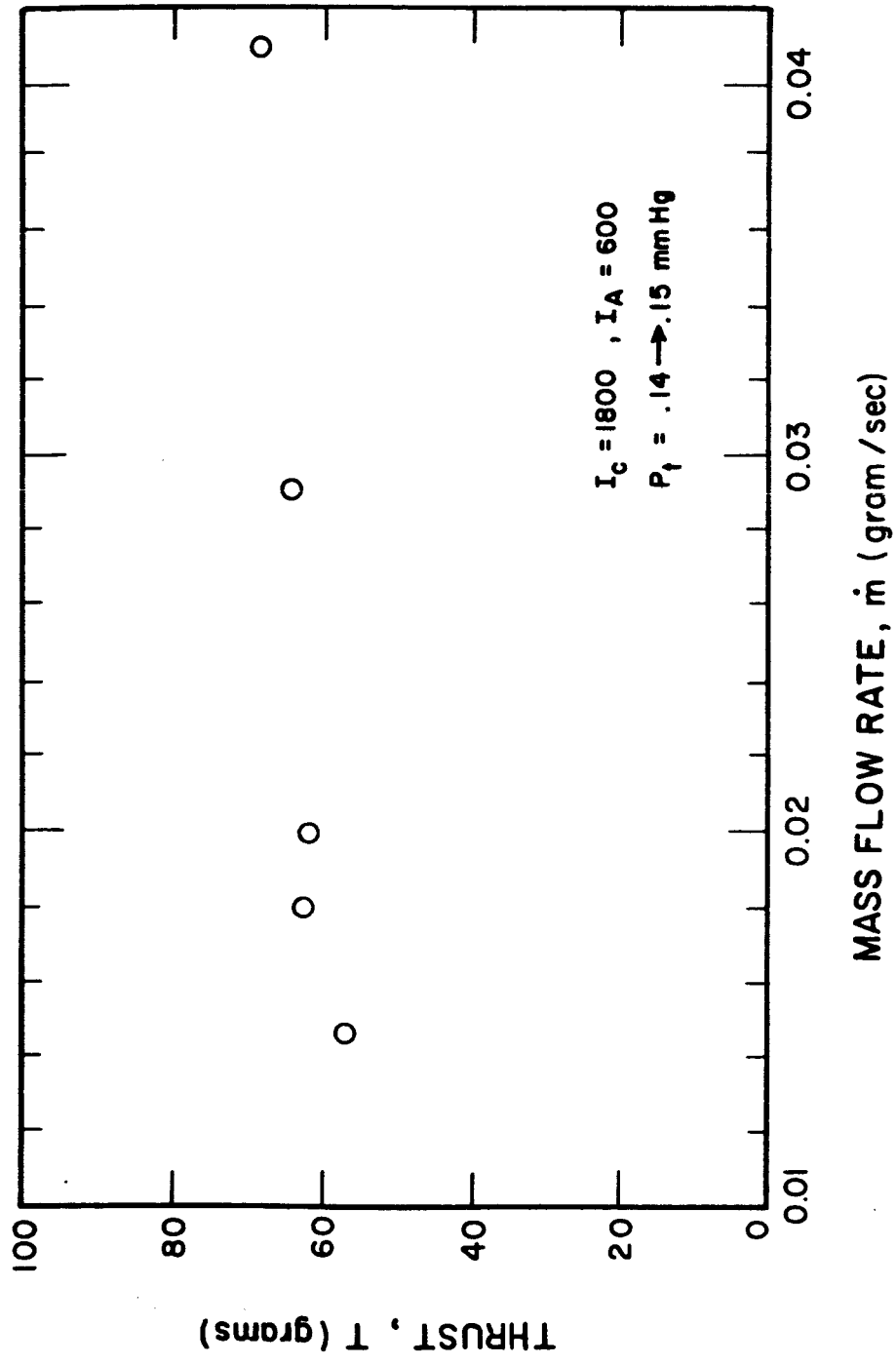

FIG. 6-12 THRUST VERSUS MASS FLOW

decreased with increasing tank pressure for pressures above about 0.5 mm Hg. (Fig. 6-13) and was only slightly affected by magnetic field strength over the range of conditions tested (Fig. 6-14). Linear dependence upon arc current can be predicted under the assumption that the plasma properties and the current distribution are independent of current. Since it would be surprising if these assumptions were always valid, a more detailed analysis still leading to a first power relationship may be needed for an accurate understanding of the effect of current level on the performance of the Hall current accelerator.

The fact that thrust is independent of mass flow rate is one of the most striking features of the H_2 Hall current accelerator and may be attributed to the fact that the accelerating mechanism is almost entirely electromagnetic. Since the thrust remains constant as mass flow rate is decreased, the thrust efficiency and effective back emf must increase. However it will probably be difficult to establish analytically the observed independence of thrust from mass flow rate because of the interrelated effects of mass flow rate on velocity and the induced electric and magnetic fields.

The effect of ambient (tank) pressure on thrust is shown in Fig. 6-13. From the lowest pressures attained to about 0.5 mm Hg., no effect on thrust was observed. Above 0.5 mm Hg, the thrust decreased with increasing pressure. That was probably due to the decrease in the local values of the Hall current caused by a decrease in the Hall parameter, $\psi_e = \omega_e \tau_e$. An additional effect may be associated with a change in the current density distribution also caused by changes in the plasma properties at higher pressures.

The slight effect of magnetic field strength on thrust shown in Fig. 6-14 is difficult to correlate with a detailed analytic description of the Hall current accelerator because of the many variables which are dependent upon the field, possibly including the current density distribution and the plasma properties. However, highly simplified considerations predict that the thrust should

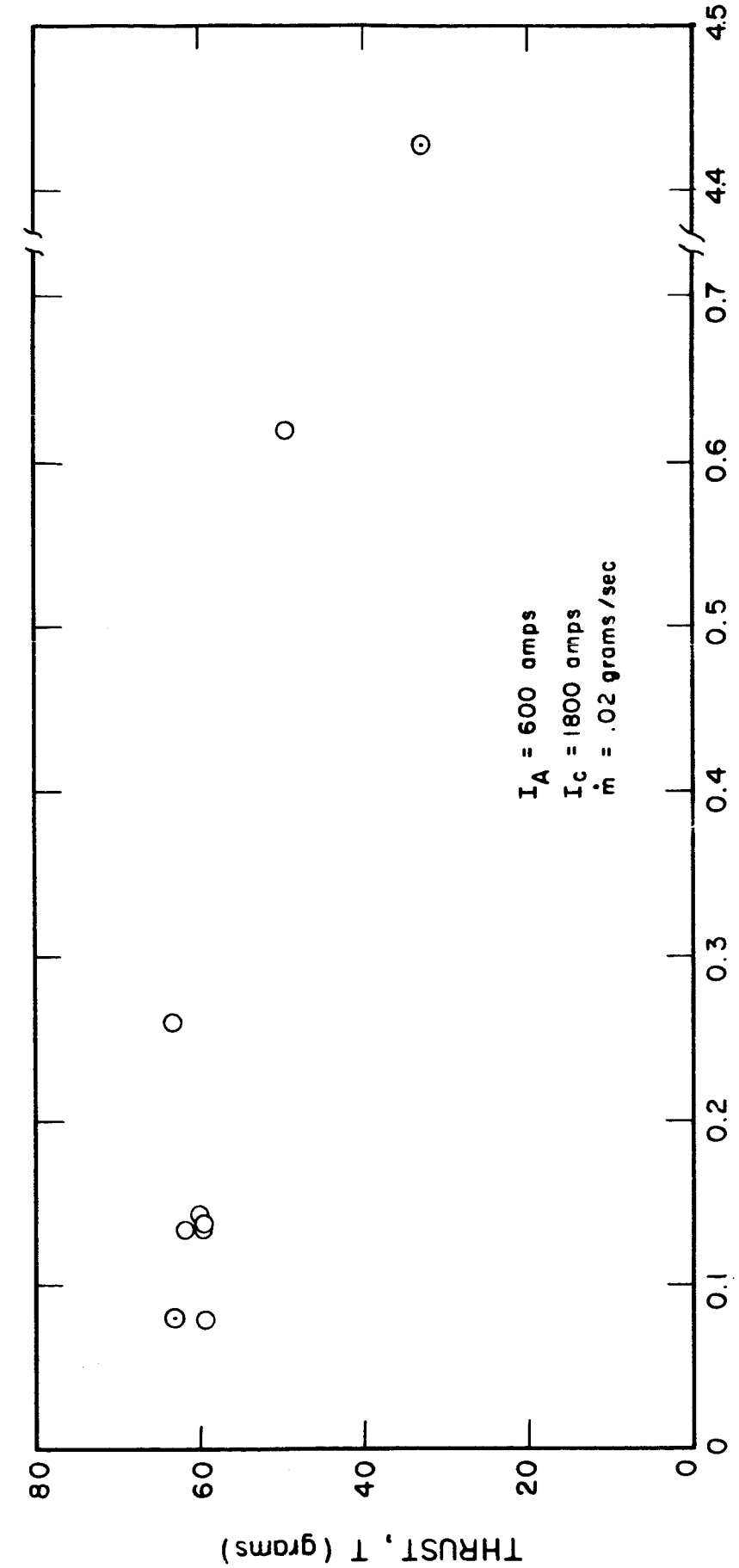

FIG. 6-13 THRUST VERSUS AMBIENT PRESSURE

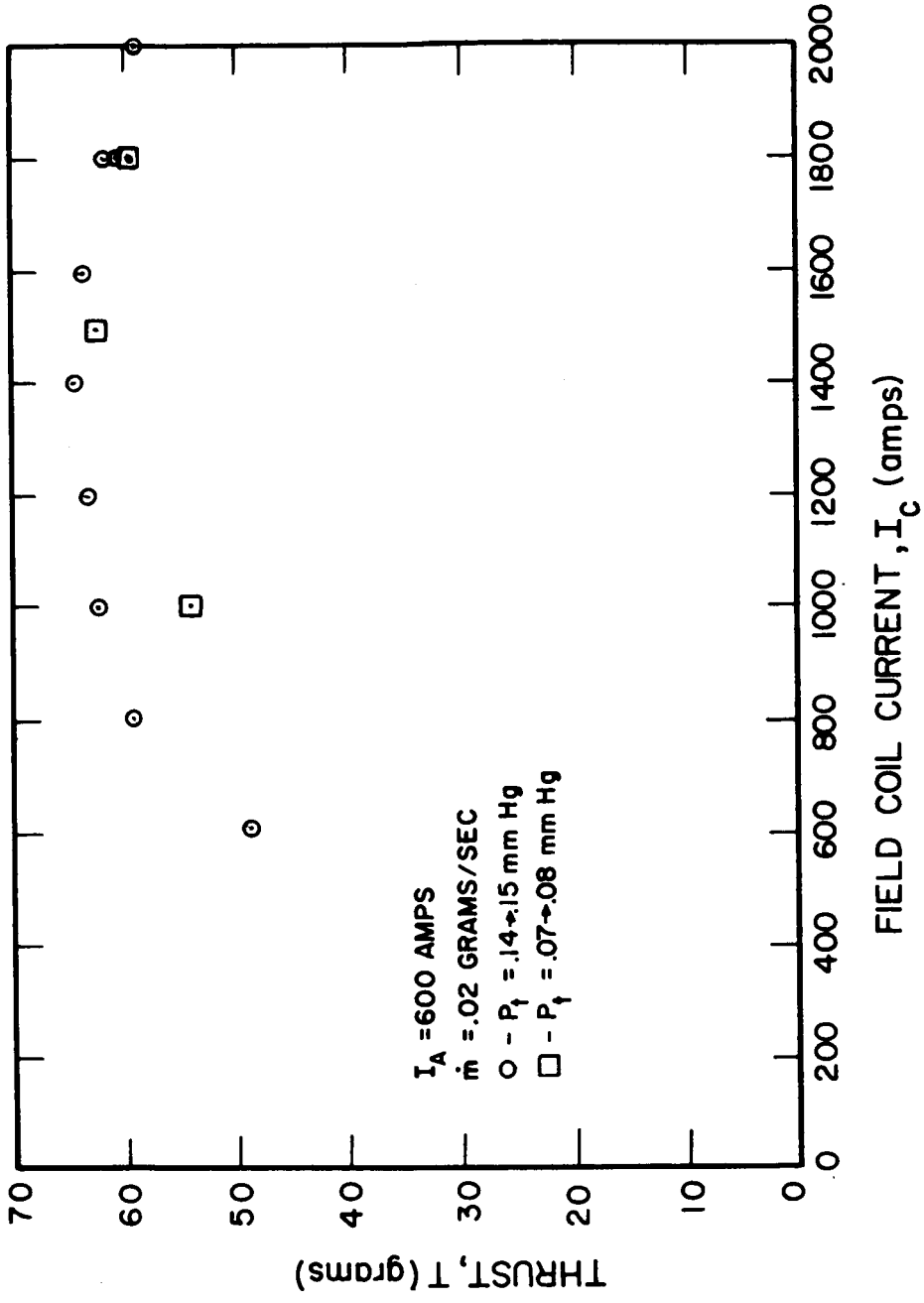

FIG. 6-14 THRUST VERSUS FIELD COIL CURRENT

increase with field strength for small fields and reach an asymptotic value for large fields (see Ref. 1 and Fig. 6-15). The experiments appear to bear out this predicted trend. Further analysis is needed to try to obtain simple analytic expressions for the magnitude of the thrust in terms of the measured magnet current.

The overall efficiency or acceleration efficiency is plotted against the specific impulse in Fig. 6-16. For both quantities the average velocity of the stream was computed as the ratio of the thrust to the mass flow rate. The increase in efficiency with I_{sp} is a consequence of the fact that thrust is linear in current and that the applied voltage remained nearly constant for the tests performed. Thus

$$\eta_o = \frac{T^2}{2\dot{m} P_{IV}} = \left(\frac{T}{\dot{m}}\right)\left(\frac{T}{I_A}\right) \frac{1}{2V} = \frac{g}{2V} \frac{T}{I_A} I_{sp}$$

varied almost linearly with I_{sp}.

In summary, the data from the tests performed on the H_2-I accelerator indicated the following trends:

1. The arc attachment at the anode was on the downstream face rather than within the arc chamber as it had been in accelerators in which the cathode was set back from the exit plane. The arc chamber pressure was also significantly lower with the present accelerator. These two effects are probably interrelated and dependent upon the independent variables of accelerator geometry, arc current and mass flow rate. The results of the present tests indicate that only a small amount of energy is transferred to the gas in the arc chamber when attachment occurs on the downstream face of the anode. Further information on these points is presented in Section 6.5, "Experimental Anode Studies".

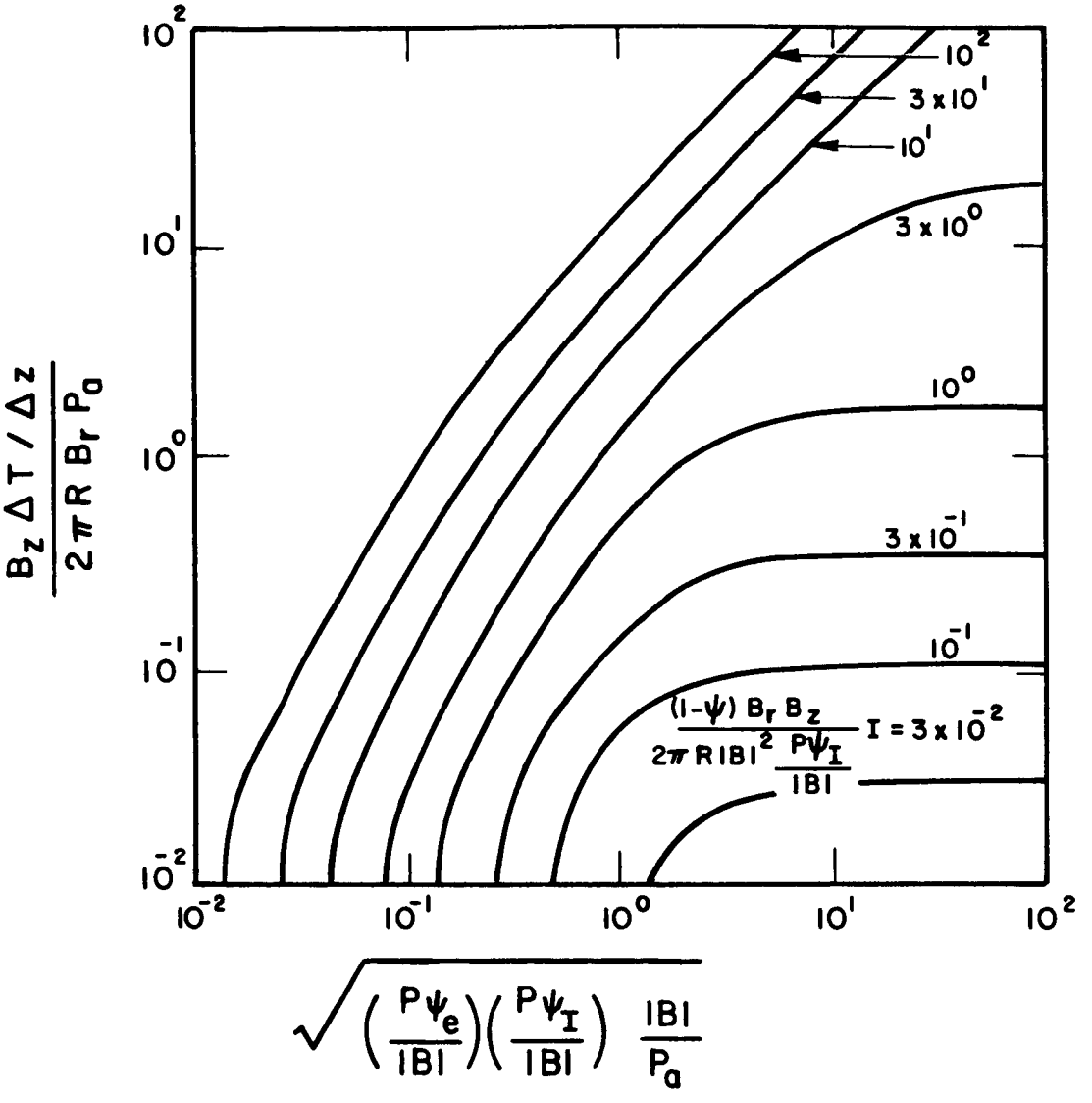

FIG. 6-15 THRUST VERSUS MAGNETIC FIELD AT CONSTANT CURRENT

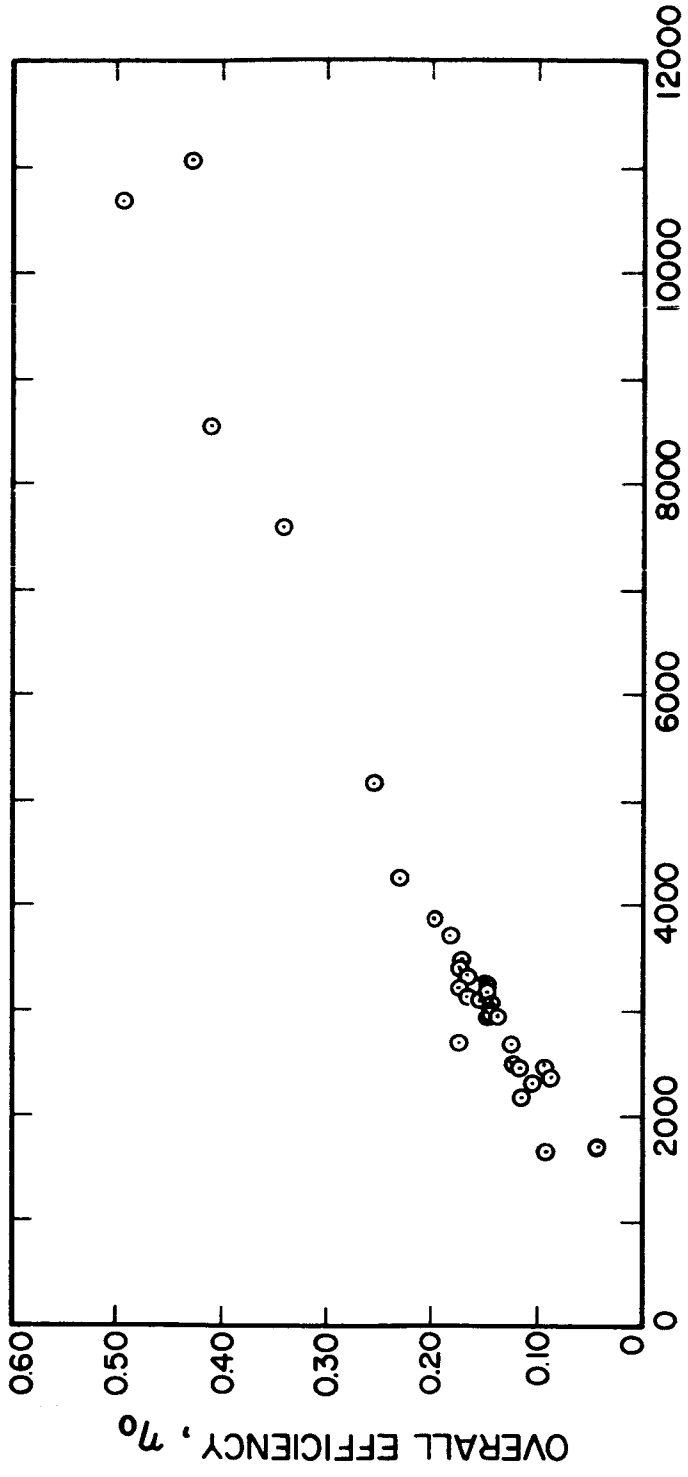

FIG. 6-16 OVERALL EFFICIENCY VERSUS SPECIFIC IMPULSE FOR H_2-I HALL CURRENT ACCELERATOR

2. The power transferred to the anode correlates well with the convective heat transfer model which proved so effective in arc jet technology; namely

$$\text{Stanton number} \propto (\text{Reynold's number})^{-n}$$

$$\frac{P_A - I_A \phi_i}{I_A V} \propto \left(\frac{A \mu_{f.s.}}{\dot{m} D} \right)^n$$

where the exponent n is between 1/3 and 1/2. Further analytical study of the anode attachment region appears to be required to explain the fact that the convective transfer model appears to be appropriate in this case.

3. The power transferred to the cathode varied linearly with arc current. Though the magnitude of the cathode losses is sufficiently small to be of little practical interest from the standpoint of optimizing the efficiency of an accelerator operating at power levels above about 50 kw, reduction of cathode losses may be important in lower power accelerators.

4. The thrust produced by the accelerator varied linearly with current, and was independent of mass flow rate. These facts, coupled with the anode heat transfer correlation, appear to indicate that, other things being equal, the best engine performance can be obtained by reducing mass flow rate rather than by increasing arc current.

5. The thrust was observed to be approximately constant with respect to changes in magnetic field, indicating that the asymptotic behavior in the vicinity of $\psi_e\psi_I = 1$, predicted on the basis of the existing theory of the Hall current accelerator, had been reached. Additional analysis is needed to demonstrate that the effect of magnetic field on the total thrust should be similar to the effect on the local magnitude of the Hall effect thrust.

6. The applied voltage varied only slightly over the entire range of conditions tested, producing an almost linear increase in overall efficiency with specific impulse. Theoretical prediction of the voltage will probably require analysis of the entire volume of interaction of the current with the applied magnetic field.

6.2 Test Using Sodium Accelerator

6.2.1 Experimental Equipment

The tests with sodium propellant have been conducted using an engine which was identical in configuration to that used for evaluating the performance capability of lithium and potassium in another program (see Ref. 5). A sketch of this engine is shown in Fig. 6-17. The unique features of this engine are:

1. The use of anode feed
2. The radiation cooling of the anode
3. The long, thick cylindrical cathode

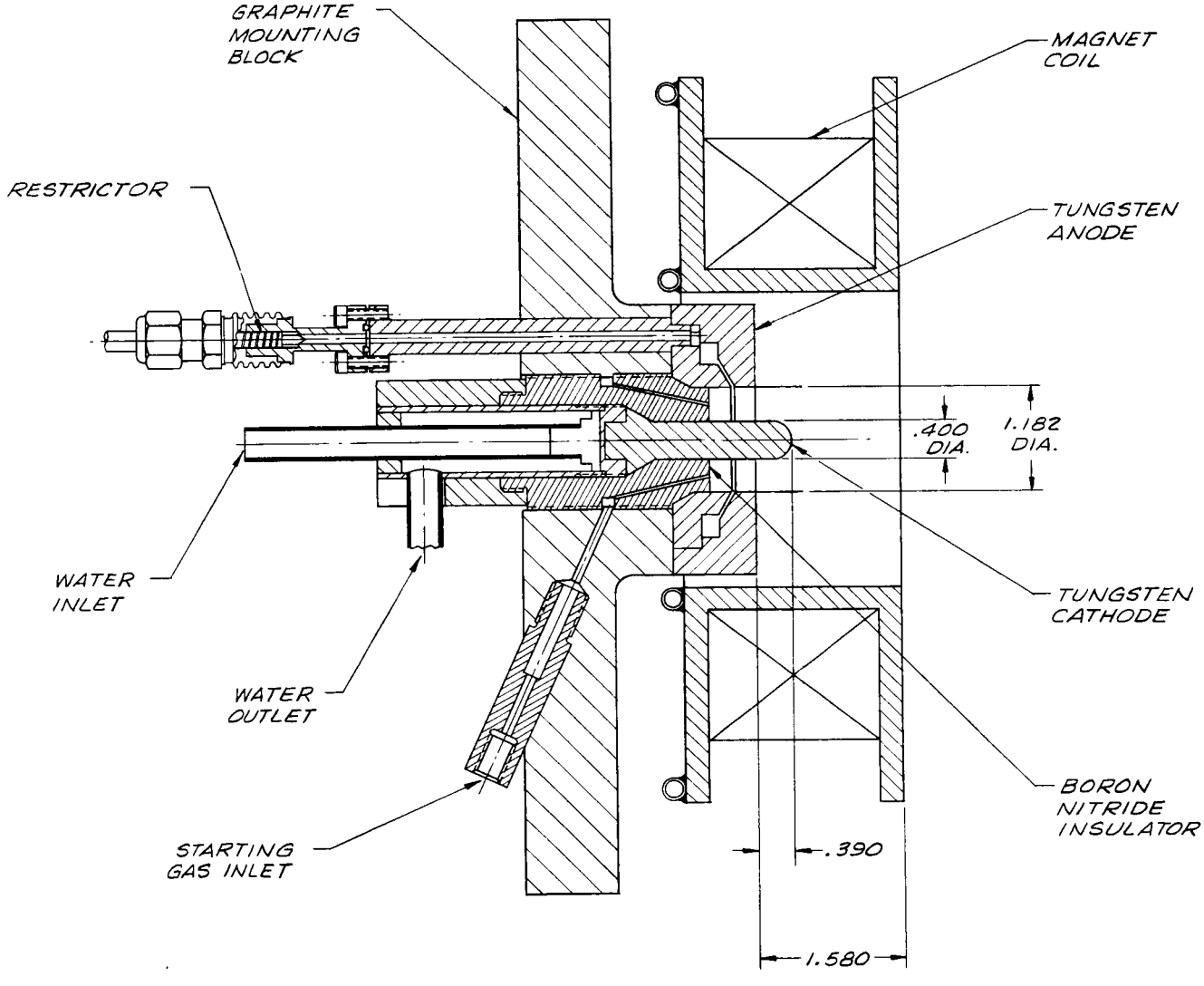

FIG. 6-17 ENGINE CONFIGURATION USED IN SODIUM TESTS

Two feed systems have been used. A boiler was constructed for vapor feed. The vapor was fed into the engine through a sonic orifice. The feed rate was determined by measuring the temperature of the liquid in the boiler and finding the pressure from the vapor pressure curves. Because of the exponential relation between the pressure and the temperature, this technique is not a sensitive or accurate method of determining a flow rate. Consequently, a number of calibration runs were conducted. It was found that a considerable discrepancy between the computed and measured flow rates existed and that they were not reproducible. For this reason only a few tests were conducted with this feed system. In the majority of the tests a liquid feed system was used. This system was identical to that used in the tests with lithium and potassium propellant and is described in Ref. 2.

The tests were conducted in vacuum chambers where the pressure was maintained below one micron by diffusion and mechanical pumps. The vacuum chamber walls were water cooled. Test results are presented in Table 6-II.

6.2.2 Thrust Measurements

One of the first tasks was that of determining the parameters upon which the measured thrust depended. It has been found previously that the tank pressure profoundly affects the measured thrust. Accordingly, several tests were conducted in which the engine was operated at constant arc current, magnet current and mass flow rate. Argon gas was injected into the vacuum chamber and the thrust was measured as a function of the tank pressure. The results of one such test are shown in Fig. 6.18. It was found that the thrust appeared constant at pressures below about one micron. The measured thrust then decreased initially to a minimum of about one-fourth the value at low pressure and then increased. From this test we concluded that valid thrust measurements were possible if the tank pressure was maintained lower than one micron.

TABLE 6-II

PERFORMANCE DATA FOR HALL CURRENT ACCELERATOR H_2-I

WITH SODIUM EXPELLANT

I_C amps	I_A amps	P_{arc} kw	Mass Flow gr/sec	Tank Pressure mm Hg.	Thrust grams	I_{sp} seconds	η_o
1800	300	9.9	.0490	5.2	47.4	970	.223
1800	350	11.7	.0556	3.8	53.2	960	.209
1800	350	11.7	.0591	3.8	58.3	990	.236
1800	350	11.7	.0584	3.8	60.1	1030	.253
1800	350	11.7	.0616	3.8	59.0	960	.231
1800	400	13.8	.0623	2.9	66.6	1070	.247
1800	450	16.3	.0619	2.1	71.2	1140	.241
1800	500	19.4	.0616	-	79.9	1300	.257
1800	500	20.5	.0392	1.2	61.6	1470	.197
1800	400	15.6	.0378	1.1	58.2	1540	.193
1800	250	14.0	.0350	1.1	55.9	1600	.306
1800	300	13.1	.0329	1.4	49.2	1500	.270
1800	200	11.4	.0318	1.4	46.9	1470	.291
1800	250	34	.0205	3.6	35.3	1720	.343
2000	200	33.5	.0186	4.7	27.7	1490	.296
1800	150	30	.0189	6.3	17.8	940	.178
1800	103	30.3	.0188	6.8	10.2	540	.086
1000	250	26.7	.0201	-	24.8	1230	.219
1800	250	34.0	.0194	3.7	37.3	1920	.405
1800	150	31	.0100	5.6	17.5	1750	.320
1800	150	32	.0101	5.8	18.4	1820	.335
1800	100	31.8	.0100	6.6	7.86	786	.093
800	200	25.3	.0100	6.0	16.4	1640	.253
800	250	25.1	.0100	5.9×10^{-4}	20.5	2070	.323

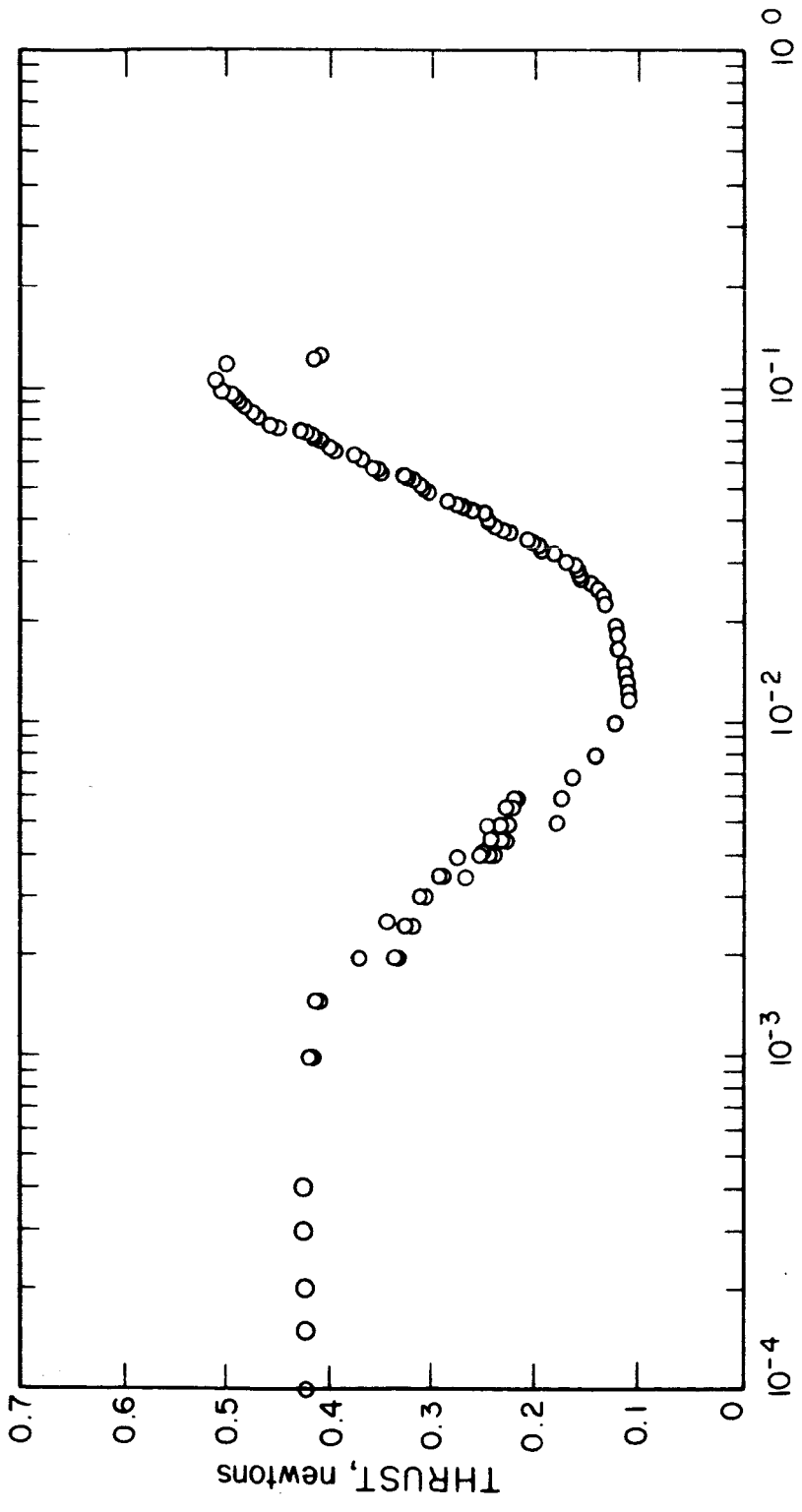

FIG. 6-18 THRUST AS A FUNCTION OF TANK PRESSURE (sodium propellant)

It has been established previously that the thrust increases linearly with the arc current. For this reason the thrust per unit current is generally plotted in this report. However, at low mass flow rates it appears that this relationship breaks down and that the thrust becomes more nearly proportional to the mass flow rate. This trend is shown in Fig. 6-19 where the thrust per unit current is plotted vs. the parameter ψ. It appears that the thrust is independent of the mass flow rate for values of $\dot{m} > .4 \frac{m_a}{|e|} I$. At lower values of $\dot{m}$ the thrust appears to be approximately proportional to the mass flow rate and independent of the arc current. It should be noted that these trends have not been observed so definitely in all tests and further experiments are still needed to clarify the exact dependence of the thrust upon the mass flow rate and the arc current at low values of ψ.

The manner in which the thrust per unit current depends upon the strength of the applied magnetic field is shown in Fig. 6-20. The thrust appears to be rising steadily as the field increases at a rate somewhat less than linearly. This curve indicates that there may be some advantage in increasing the magnetic field strength beyond the maximum of 3000 gauss available from our coil at the present time.

If the above measurements are compared with those in Ref. 6, where H_2 propellant was used, the following comments can be made:

1) In the hydrogen tests the thrust was independent of the tank pressure over the range of 100 to 4000μ. The test with sodium indicates that the thrust falls off and then increases as the pressure is increased.

2) The thrust was found to be linearly dependent upon the arc current and independent of the mass flow rate in hydrogen. At low mass flow rates the thrust appears to become proportional to the mass flow rate and independent of the arc current with sodium propellant. At higher mass flow rates of sodium the thrust is linearly dependent upon the arc current and independent of the mass flow rate.

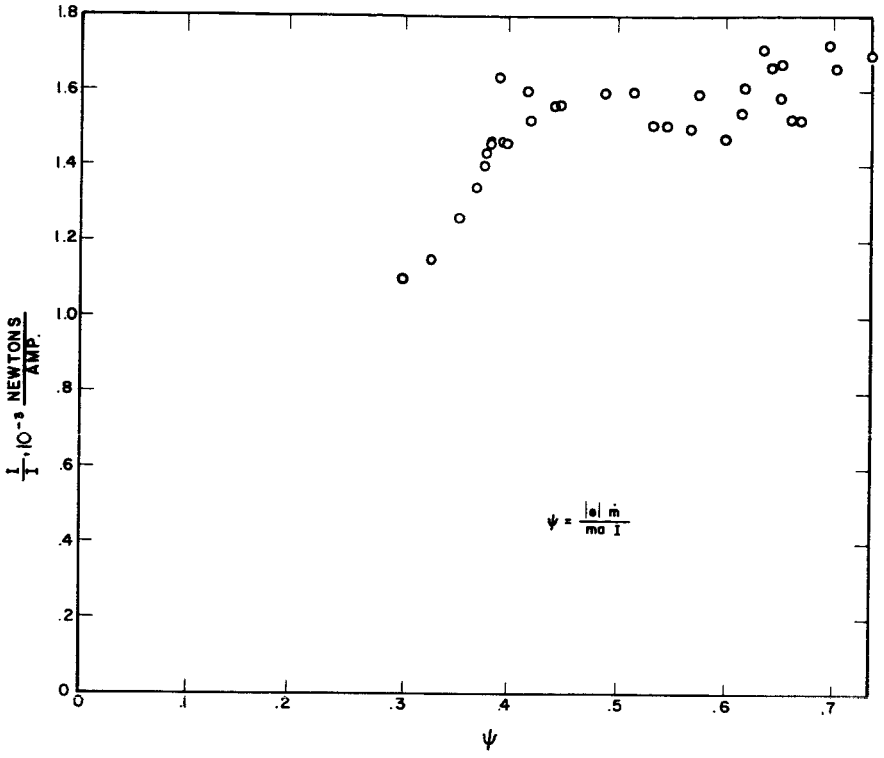

FIG. 6-19 THRUST PER UNIT CURRENT AS A FUNCTION OF THE PARAMETER Ψ (sodium propellant)

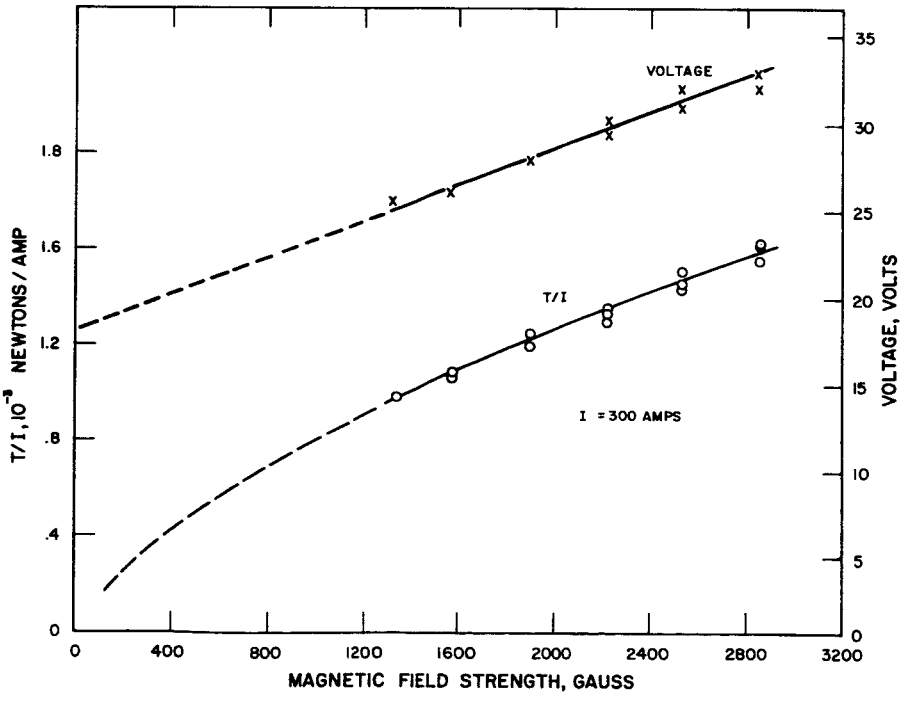

FIG. 6-20 EFFECT OF MAGNETIC FIELD STRENGTH ON HALL-CURRENT ACCELERATOR WITH SODIUM

3) With hydrogen propellant, the thrust was independent of the magnetic field strength between 3000 and 1500 gauss. At lower field strengths the thrust decreased. The tests with sodium propellant indicate that the thrust increases with the magnetic field up to the maximum available of about 3000 gauss.

6.2.3 Potential Measurements

A number of potential measurements have been made. These are as follows:

1) The anode to cathode potential
2) The anode to magnet shield potential
3) The anode to tank potential
4) The cathode to tank potential

The anode to cathode potential is plotted in Fig. 6-21 as a function of the parameter ψ, which is the ratio of mass flow rate to arc current. This plot shows the characteristic predicted by the phenomenological theory, namely, that the potential drop is relatively constant for values of ψ greater than some minimum value and then rises steeply for lower values of ψ. Some plots of the anode to tank potential, cathode to tank potential and anode to magnet shield potential as functions of the arc current and mass flow rate are shown in Figs. 6-22 through 6-26. The general tendency appears to be that the anode to tank potential increases with $1/\psi$ and the cathode to tank potential increases with ψ. A great deal of scatter is found in the anode to magnet shield potential measurements. This appears to be due to a number of factors which are not well understood. One important factor, however, appears to be modal transitions of the arc behavior in which the potential distribution changes spontaneously at one operating point. Such a transition is shown in Fig. 6-27. This transition is tentatively assumed to be associated with the heating of the electrodes.

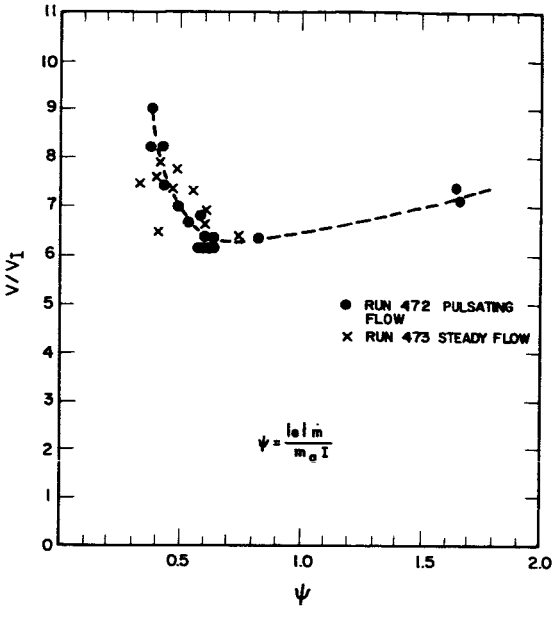

FIG. 6-21

VOLTAGE CHARACTERISTIC FOR SODIUM HALL ACCELERATOR

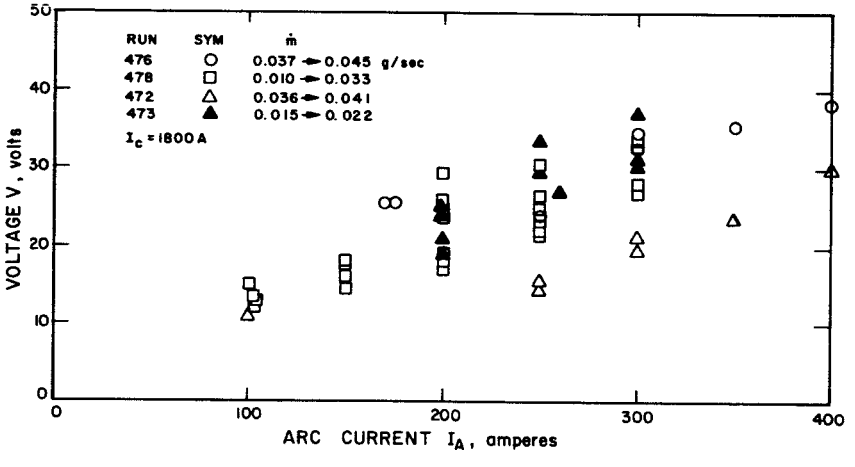

FIG. 6-22

ANODE-TO-TANK POTENTIAL AS A FUNCTION OF ARC CURRENT (sodium propellant)

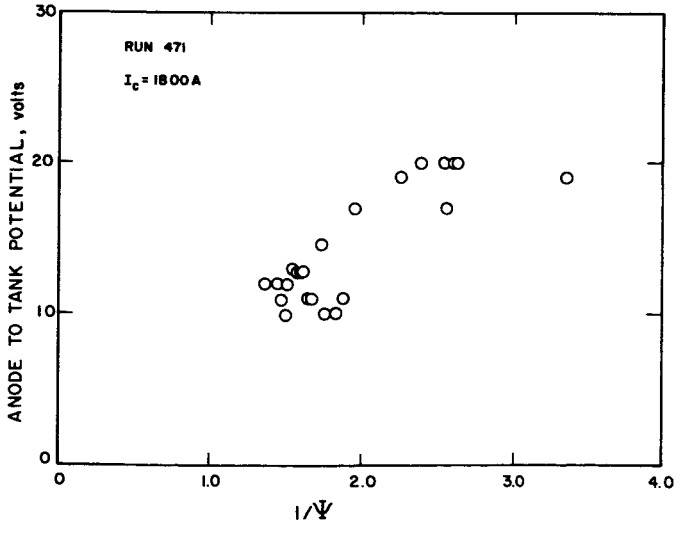

FIG. 6-23

ANODE-TO-TANK POTENTIAL AS A FUNCTION OF 1/Ψ (sodium propellant)

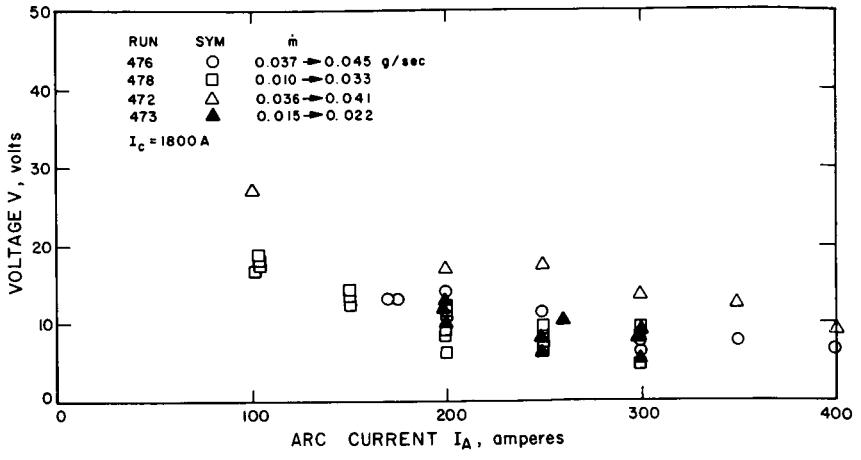

FIG. 6-24

TANK-TO-CATHODE POTENTIAL AS A FUNCTION OF ARC CURRENT (sodium propellant)

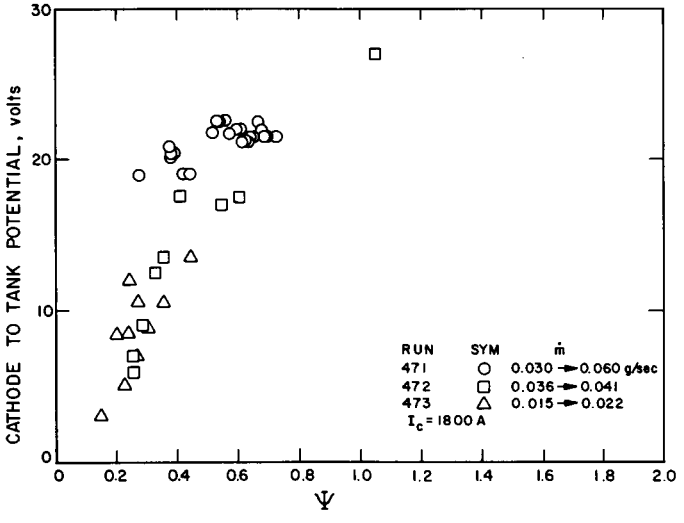

FIG. 6-25

CATHODE-TO-TANK POTENTIAL AS A FUNCTION OF Ψ (sodium propellant)

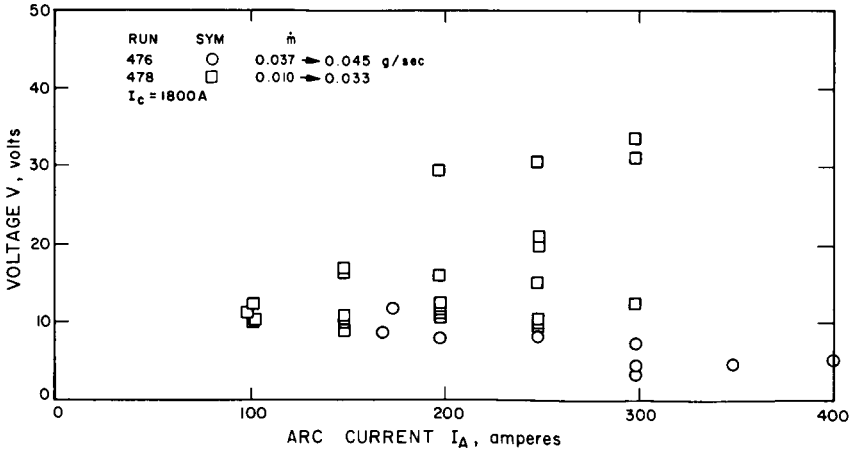

FIG. 6-26

ANODE-TO-SHIELD POTENTIAL AS A FUNCTION OF ARC CURRENT (sodium propellant)

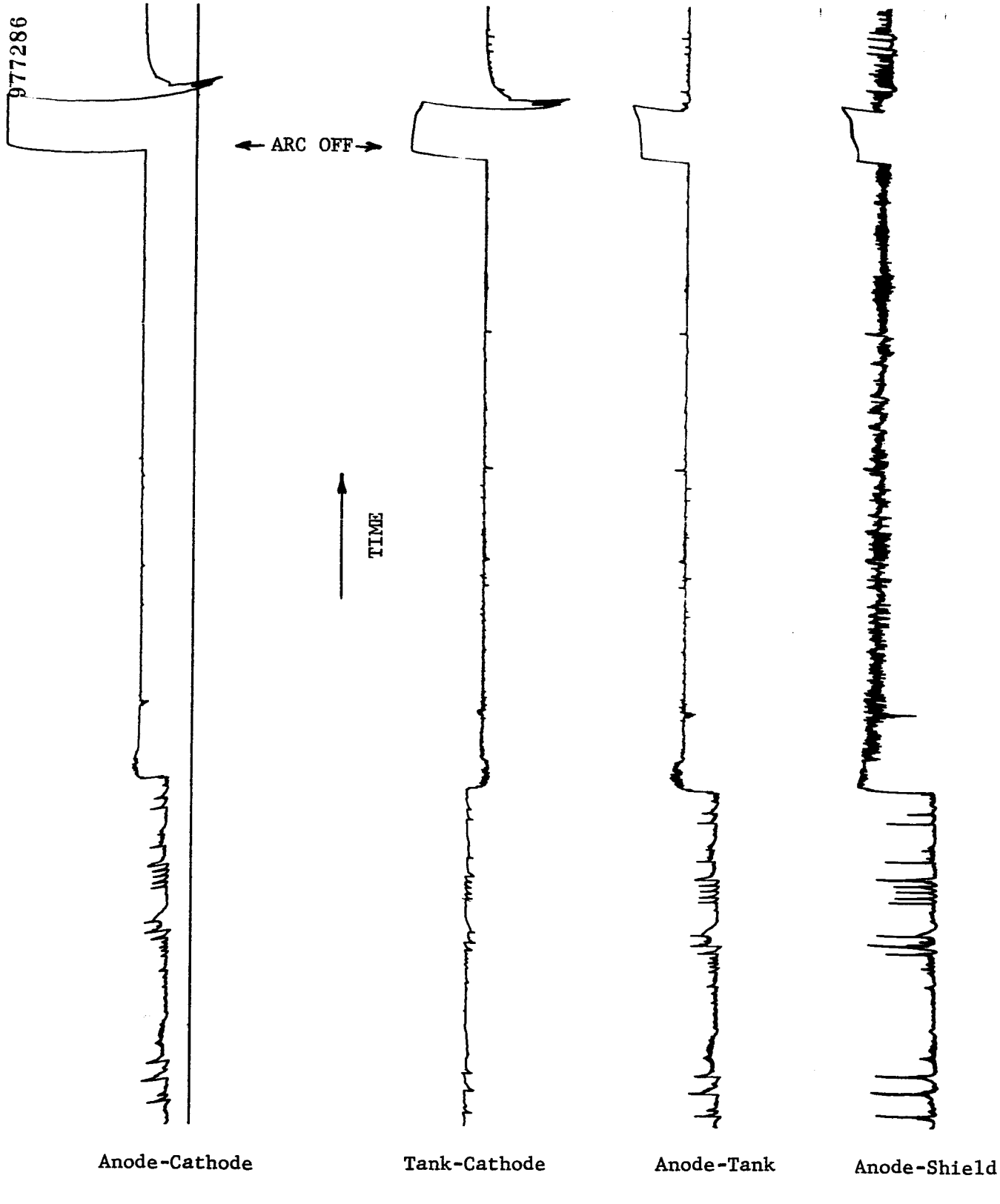

FIG. 6-27 RECORDING OF VOLTAGES OF THE SODIUM ARC JET

The arc potential drop is plotted as a function of the magnetic field strength in Fig. 6-20. The anode to tank potential cathode to tank potential and anode to shield potential are plotted as a function of the magnetic field strength in Figs. 6-28 through 6-31. These plots indicate that the cathode to tank potential is independent of the magnetic field strength, and that the anode to tank potential increases approximately linearly with the strength of the magnetic field.

6.2.4 Anode Power Measurements

The anode in the sodium tests was radiation cooled. However, in order to measure the anode power, it was surrounded by an oil cooled jacket which picked up a high percentage of the radiated power from the anode. A set of measurements of the anode power as a function of the magnetic field strength and arc current are shown in Figs. 6-32, 6-33, and 6-34. Some results from a test with potassium are shown for comparison.

6.2.5 Overall Performance

Plots of the overall performance capability are shown for several tests in Figs. 6-35 and 6-36. These plots show the characteristic linear relation between the efficiency and the specific impulse of most of the results obtained from Hall current plasma accelerators. These curves indicate that good performance can be expected from sodium in the 2000 sec. I_{sp} range and probably at somewhat higher I_{sp} as well. Test results at specific impulses above 2000 sec are not shown due to uncertainty of mass flow measurement.

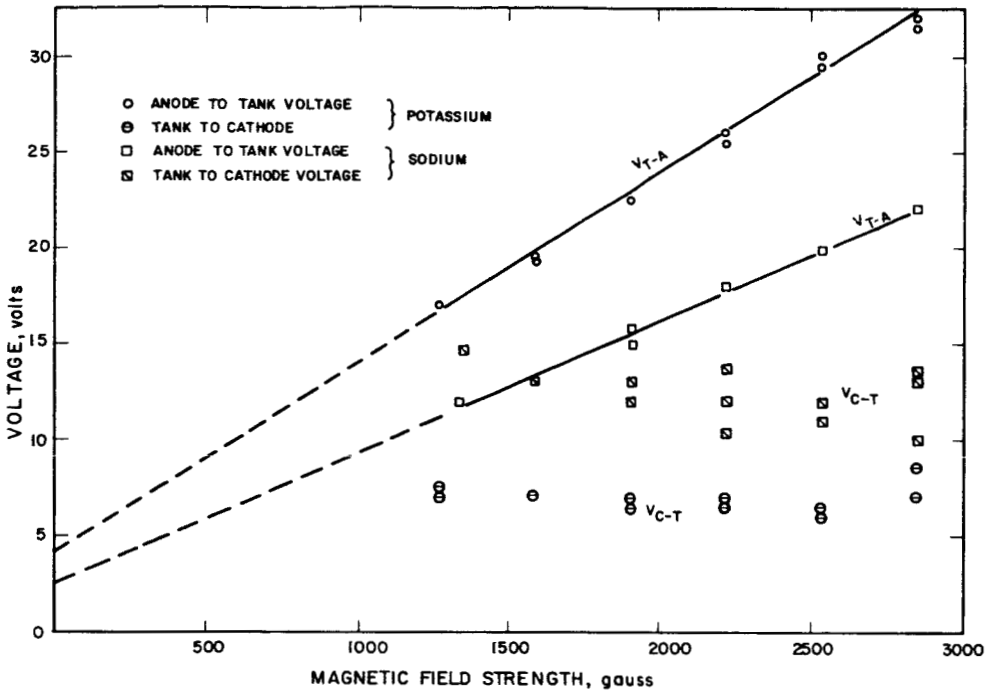

FIG. 6-28

EFFECT OF MAGNETIC FIELD ON ARC POTENTIALS FOR SODIUM AND POTASSIUM

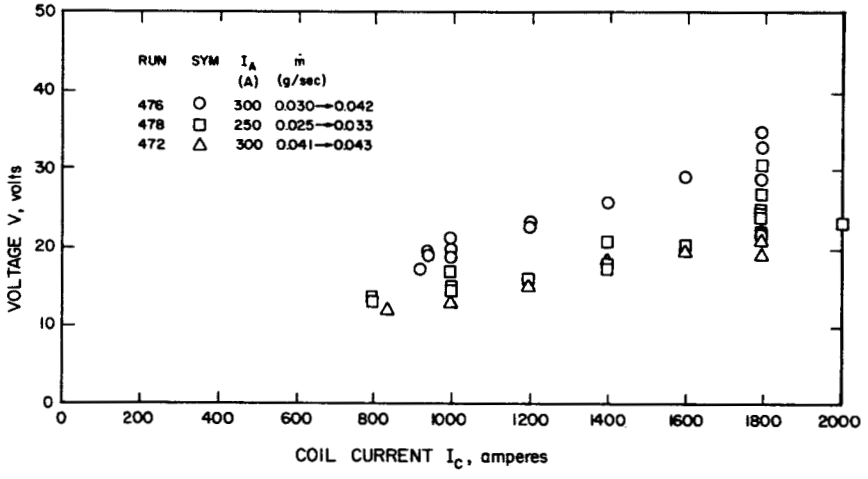

FIG. 6-29

ANODE-TO-TANK POTENTIAL AS A FUNCTION OF COIL CURRENT (sodium propellant)

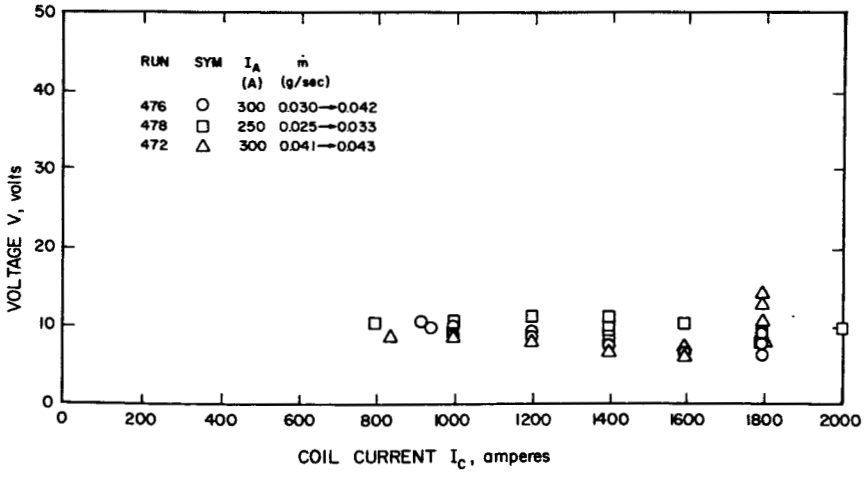

FIG. 6-30

TANK-TO-CATHODE POTENTIAL AS A FUNCTION OF COIL CURRENT (sodium propellant)

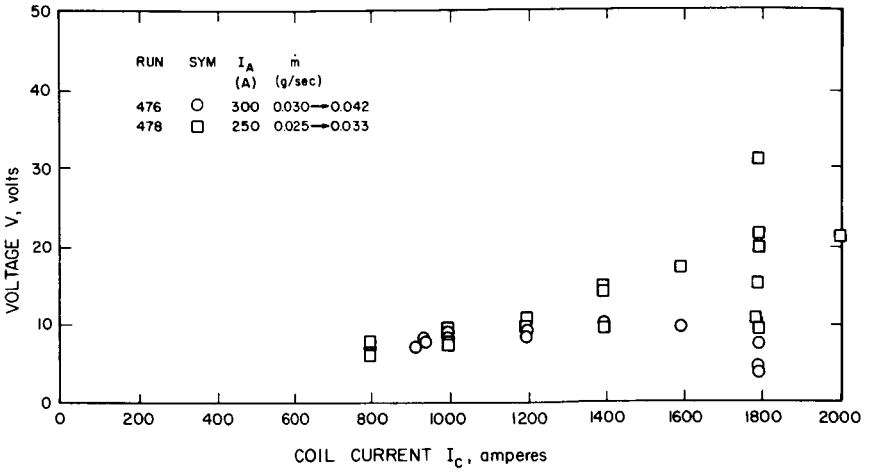

FIG. 6-31

ANODE-TO-SHIELD POTENTIAL AS A FUNCTION OF COIL CURRENT (sodium propellant)

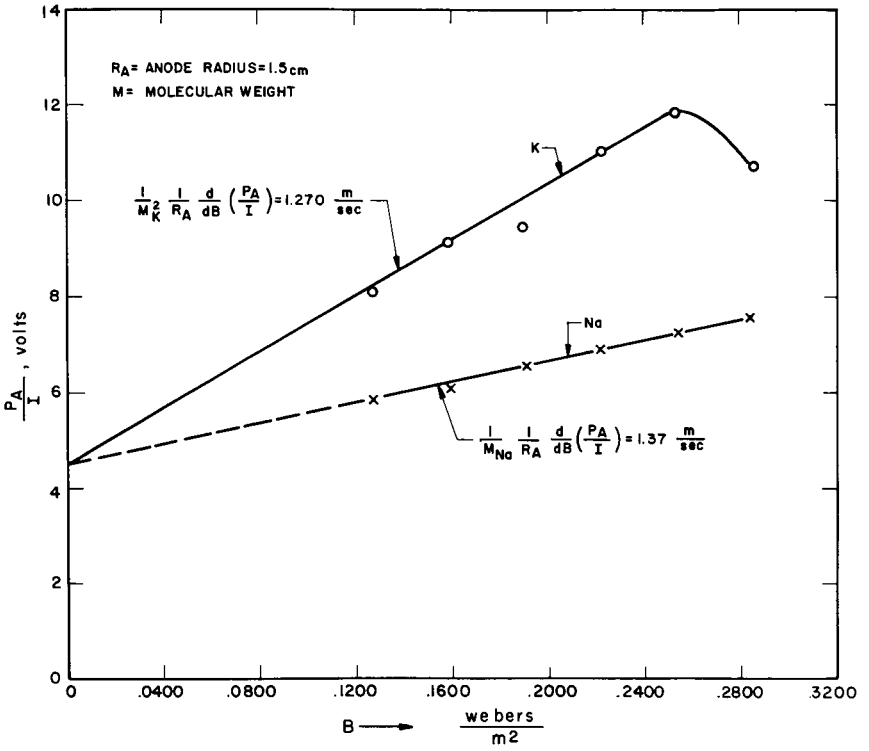

FIG. 6-32

EFFECT OF MAGNETIC FIELD STRENGTH ON ANODE POWER LOSS FOR SODIUM AND POTASSIUM

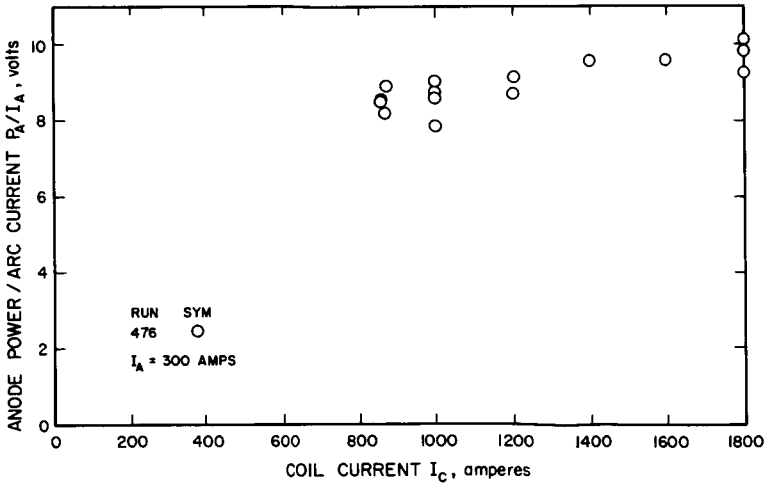

FIG. 6-33

ANODE POWER LOSS AS A FUNCTION OF COIL CURRENT (sodium propellant)

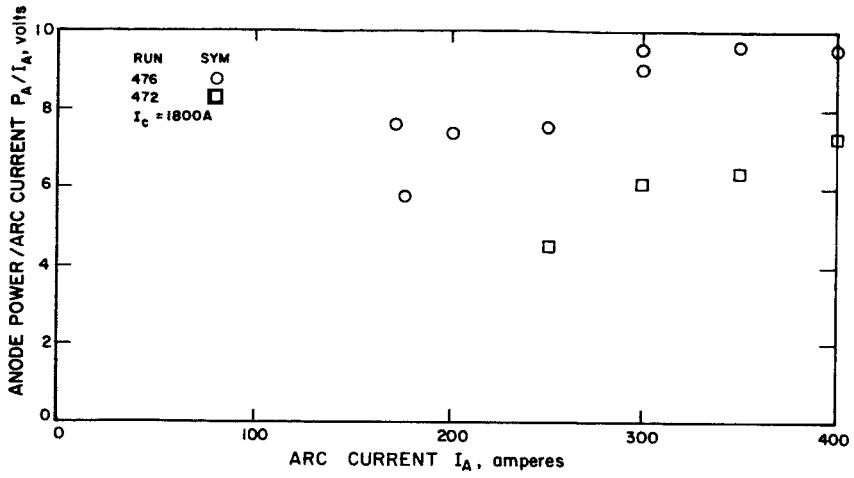

FIG. 6-34

ANODE POWER LOSS AS A FUNCTION OF ARC CURRENT (sodium propellant)

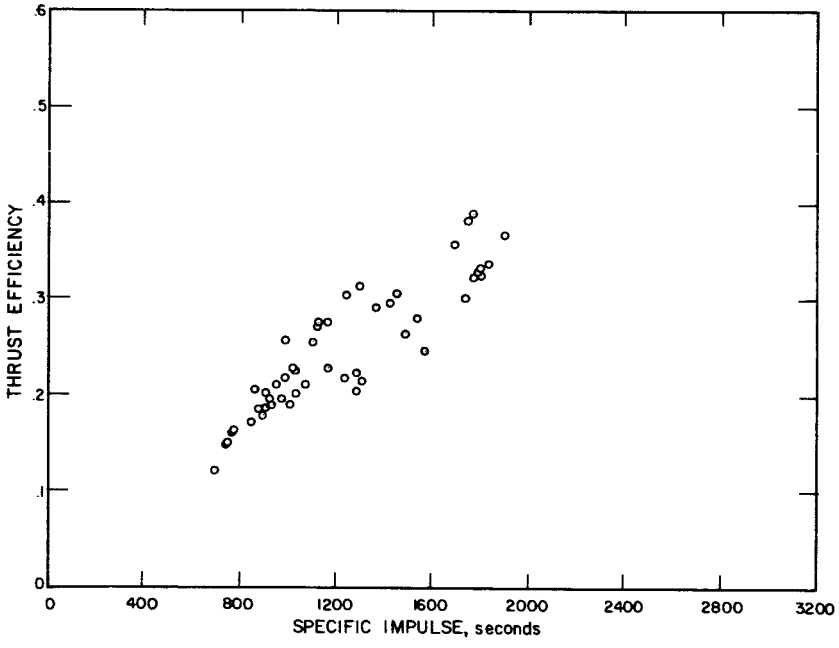

FIG. 6-35

PERFORMANCE OF HALL-CURRENT ACCELERATOR WITH SODIUM

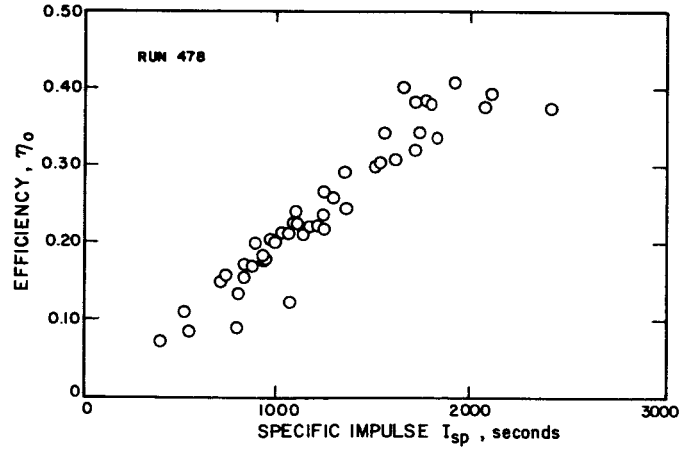

FIG. 6-36

EFFICIENCY AS A FUNCTION OF SPECIFIC IMPULSE (sodium propellant)

6.3 Development of Engine for Low Density Tests

The operating characteristics of Hall current accelerators were found to change mode as the mass flow was reduced below a critical value (see Ref. 1). It is not certain whether this effect was due to the decrease in mass flow or tank pressures. For this, and for other reasons, there is a need to conduct experiments with an accelerator when the tank pressure is very low, e.g., about 10^{-4}-10^{-5} mm of Hg. A partially radiation cooled engine that is to be used for such tests has been designed and given preliminary tests. The engine was designed to run at a power level of 10 kW and a mass flow rate of 1-3 mg/sec.

The first model that was built and tested is shown in Fig. 6-37. This engine ran well at high mass flow, i.e., 10 mg/sec but would not operate in a steady mode at lower mass flow rates. Accordingly, the anode shape was modified as shown by the insert on Fig. 6-37. When this model was tested, the insulator burned back very quickly and an axial arc of low voltage established itself between the outer edge of the cathode rod and the inner edge of the anode cavity.

The electrode configuration was next modified to that shown in Fig. 6-38. A larger diameter magnet was also used. This model operated satisfactorily for extended periods of time at a mass flow rate of about 3 mg/sec. However, the specific impulse and thrust efficiency as computed from the target thrust measurement appeared to be abnormally low. It was speculated that this was caused by the target being too far from the engine (approximately 14 inches) and intercepting only part of the jet. Another possible cause was thought to be the friction forces of the shroud, which had been designed to increase the radiating surface of the anode. For the next test, the shroud was removed from the anode (see insert on Fig. 6-38) and the target was moved up to within 7 inches of the anode face. The measurements on this engine configuration indicated that acceptable performance was being obtained at a mass flow rate of about 3 mg/sec. Some representative data from the tests are shown in Table 6-III. A plot of the

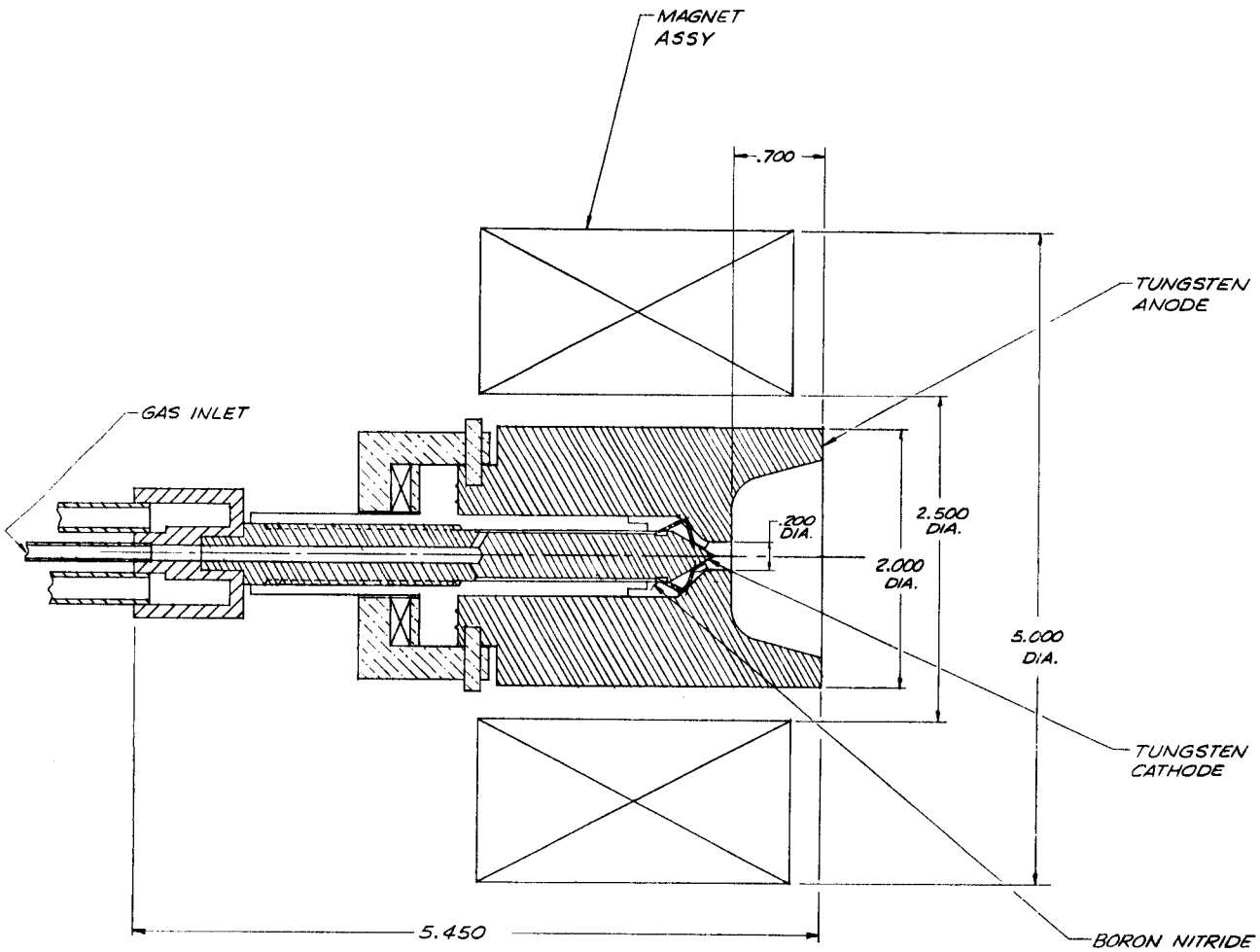

-1 ACCELERATOR ASSY
(MODEL H_2-2-A)

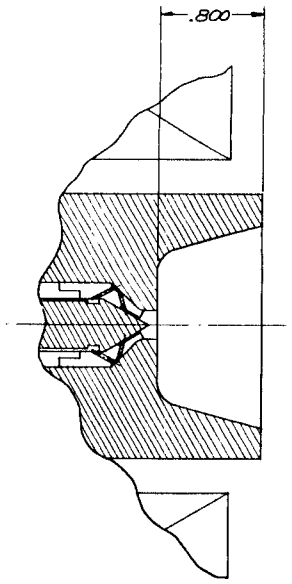

-2 ACCELERATOR ASSY
(MODEL H_2-2-B)
NOTE: IDENTICAL TO -1 EXCEPT AS SHOWN.

FIG. 6-37 10 KW HALL CURRENT ACCELERATOR - MODEL H_2-2-A AND H_2-2-B

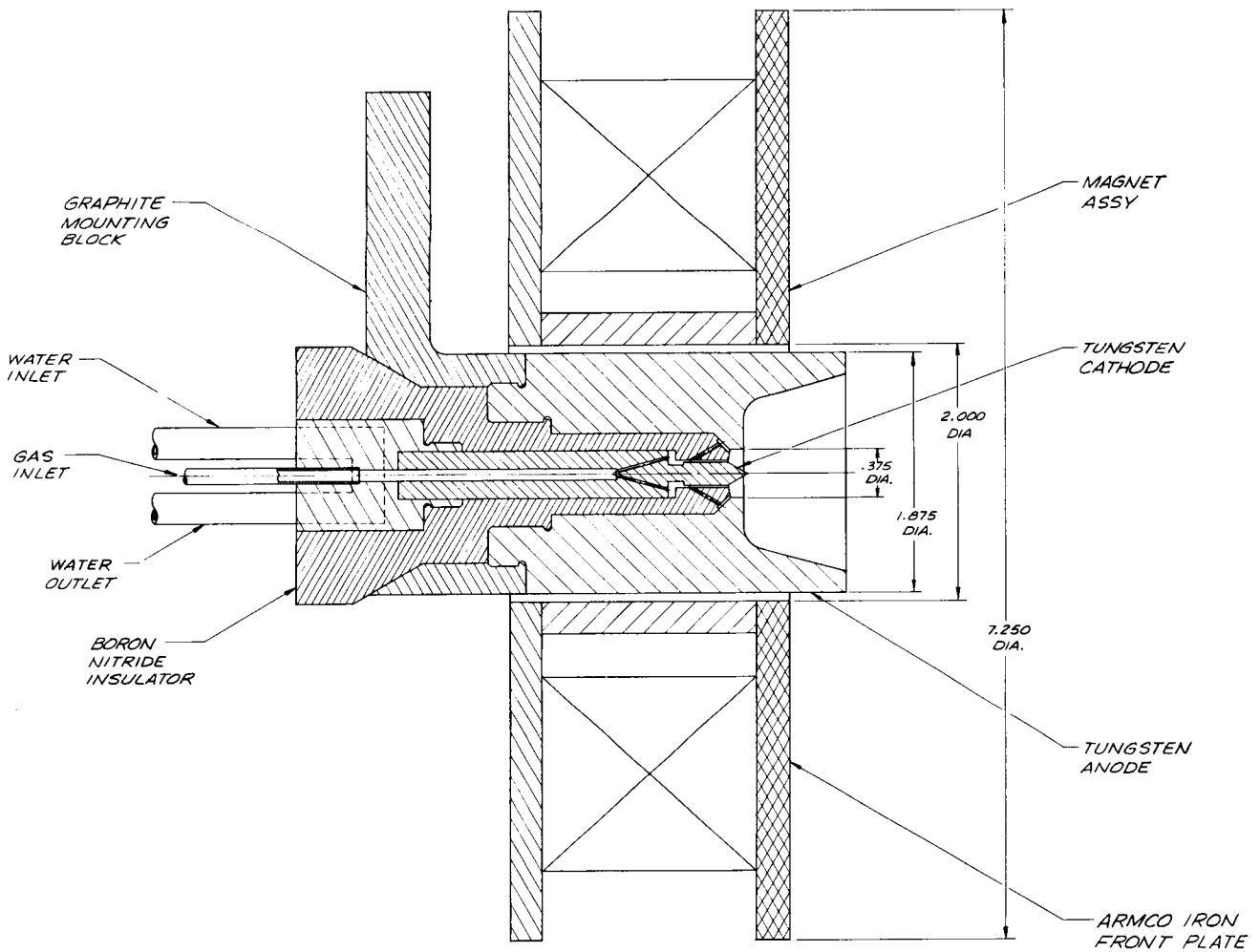

-1 ACCELERATOR ASSY
(MODEL H_2-2-C)

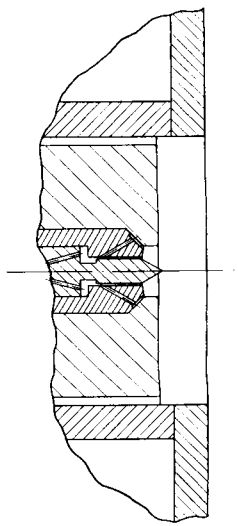

-2 ACCELERATOR ASSY
(MODEL H_2-2-D)
NOTE: IDENTICAL TO -1 EXCEPT AS SHOWN

FIG. 6-38 HALL CURRENT ACCELERATOR ASSEMBLY, 10 KW - MODEL H_2-2-C AND H_2-2-D

TABLE 6-III

EXPERIMENTAL DATA FOR THE 10 KW ENGINE

$\dot{m}$ mg/sec	I_a amps	I_m amps	P_{IV} kw	p_t mm Hg.	T gms	I_{sp} sec.	η_o
6.85	177	1800	11.2	.052	6.83	997	.029
6.85	200	1800	12.3	.045	8.63	1260	.042
6.85	225	1800	13.6	.050	10.0	1460	.052
6.69	235	1800	14.3	.053	11.0	1640	.061
5.23	150	1800	10.4	.040	9.69	1850	.083
5.23	175	1800	11.4	.040	11.7	2240	.110
5.23	200	1800	12.1	.042	13.9	2660	.147
3.93	200	1800	11.7	.037	12.9	3280	.174
3.93	200	1800	11.6	.038	13.2	3360	.183
3.69	210	1940	12.2	.038	15.8	4280	.266
3.61	208	1920	12.9	.110	11.5	3190	.136
3.61	208	1920	13.0	.250	8.03	2220	.066
3.61	206	1915	12.7	.040	14.8	4100	.229
3.61	208	1900	12.8	.040	15.6	4320	.253
3.61	206	1880	12.8	.040	15.8	4380	.259

thrust efficiency versus the specific impulse is shown in Fig. 6-39. A plot of the specific impulse at constant mass flow rate versus the tank pressure is shown in Fig. 6-40. This plot indicates that the thrust is increasing slightly as the tank pressure is reduced to 30μ of Hg pressure.

Unstable arc operation occurred when attempts were made to reduce the mass flow rate below 3 mg/sec. Alternative designs which would operate well at 1 mg/sec mass flow rate were sought.

During the tests on the high power accelerator (H_2-I) (Ref. 4), as well as during those conducted on the 10-kW engine (H_2-2C and H_2-2B), an instability of the discharge occurring in the exhaust plume was found to occur below certain mass flow rates. Observation of the accelerator electrodes while this instability was setting in indicated that it was most likely caused by an unsteady cathode attachment; the attachment region moving discontinuously from the point of the conical cathode to a side of the cathode. A similar transition of the cathode attachment region in an argon arc had been observed and reported in Ref. 7. Stable attachment to the point of the conical cathode appeared to occur only above some critical pressure, which was about 1-2 mm Hg when the ambient gas was hydrogen. Based on this hypothesis, a number of engines were designed in which various techniques were used to maintain the pressure at the cathode at values of over 10 mm Hg at mass flow rates for H_2 of under 0.001 g/sec. Attempts were made to keep the anode and cathode configuration similar to that shown in Fig. 6-41 since this accelerator performed well at mass flow rates of 0.001 g/sec and relatively high tank pressure (Table 6-IV, Model H_2-2B).

In configurations similar to that shown in Fig. 6-41, the pressure at the cathode is controlled by the anode orifice which acts as a sonic nozzle. The pressure at the cathode can then be expressed as

$$p_c = \frac{\dot{m}\sqrt{h_o}}{\Psi A_A} \qquad (3)$$

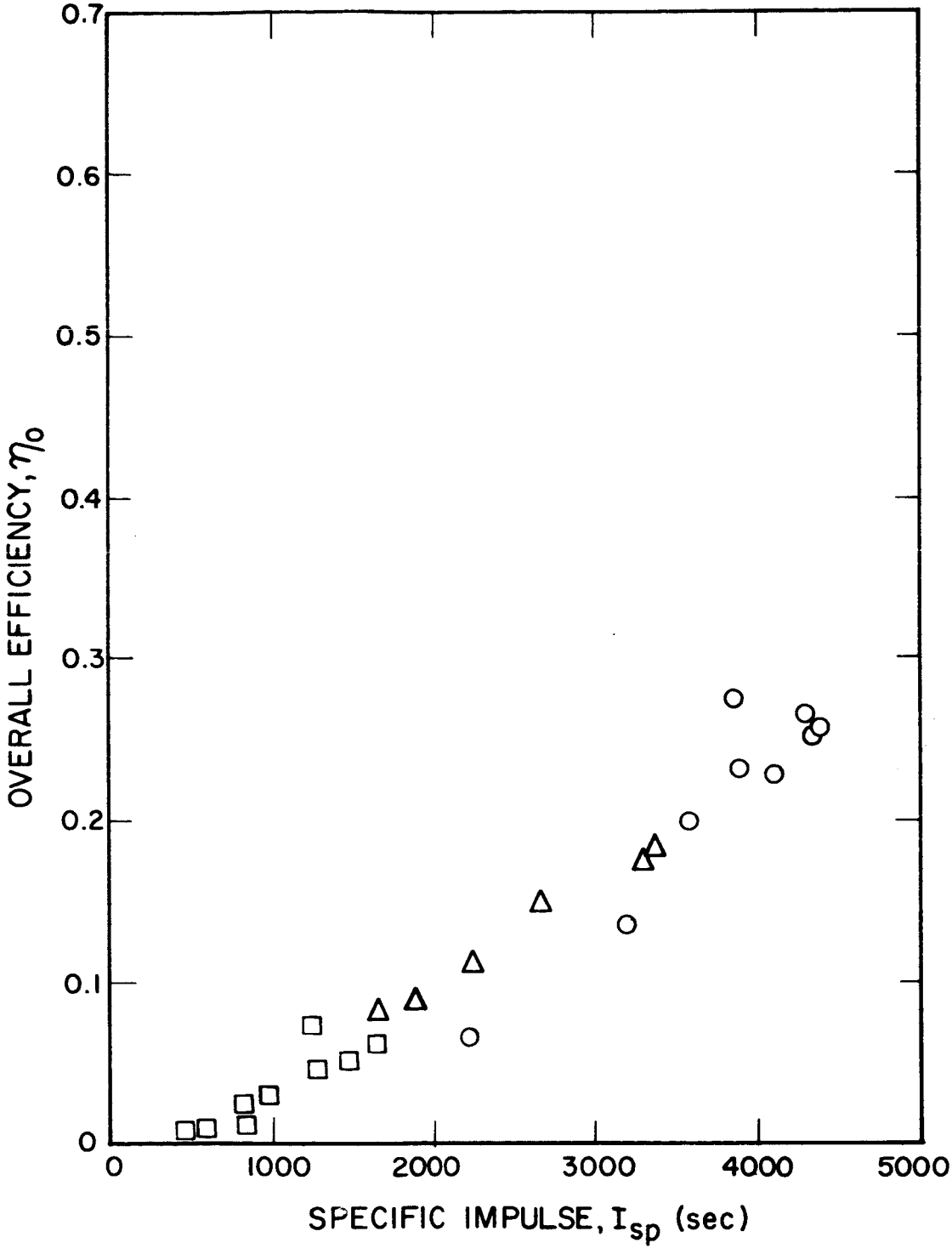

FIG. 6-39 OVERALL EFFICIENCY VERSUS SPECIFIC IMPULSE FOR RADIATION-COOLED ENGINE

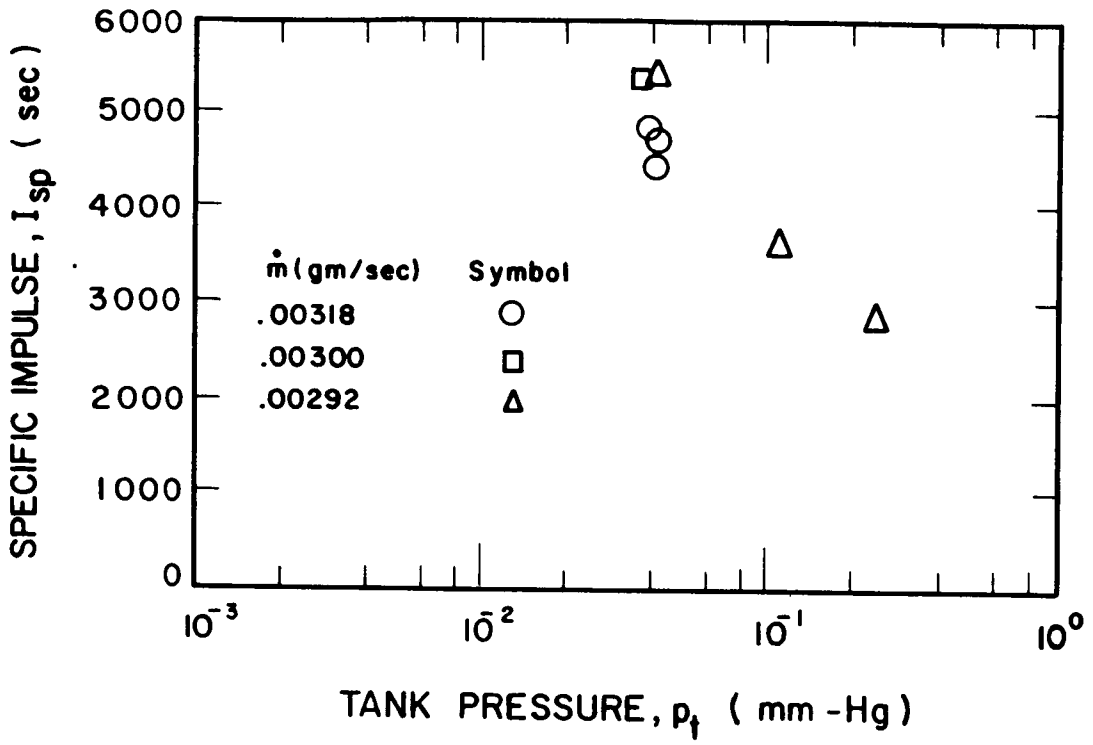

FIG. 6-40 SPECIFIC IMPULSE VERSUS AMBIENT PRESSURE WITH VARYING MASS FLOW

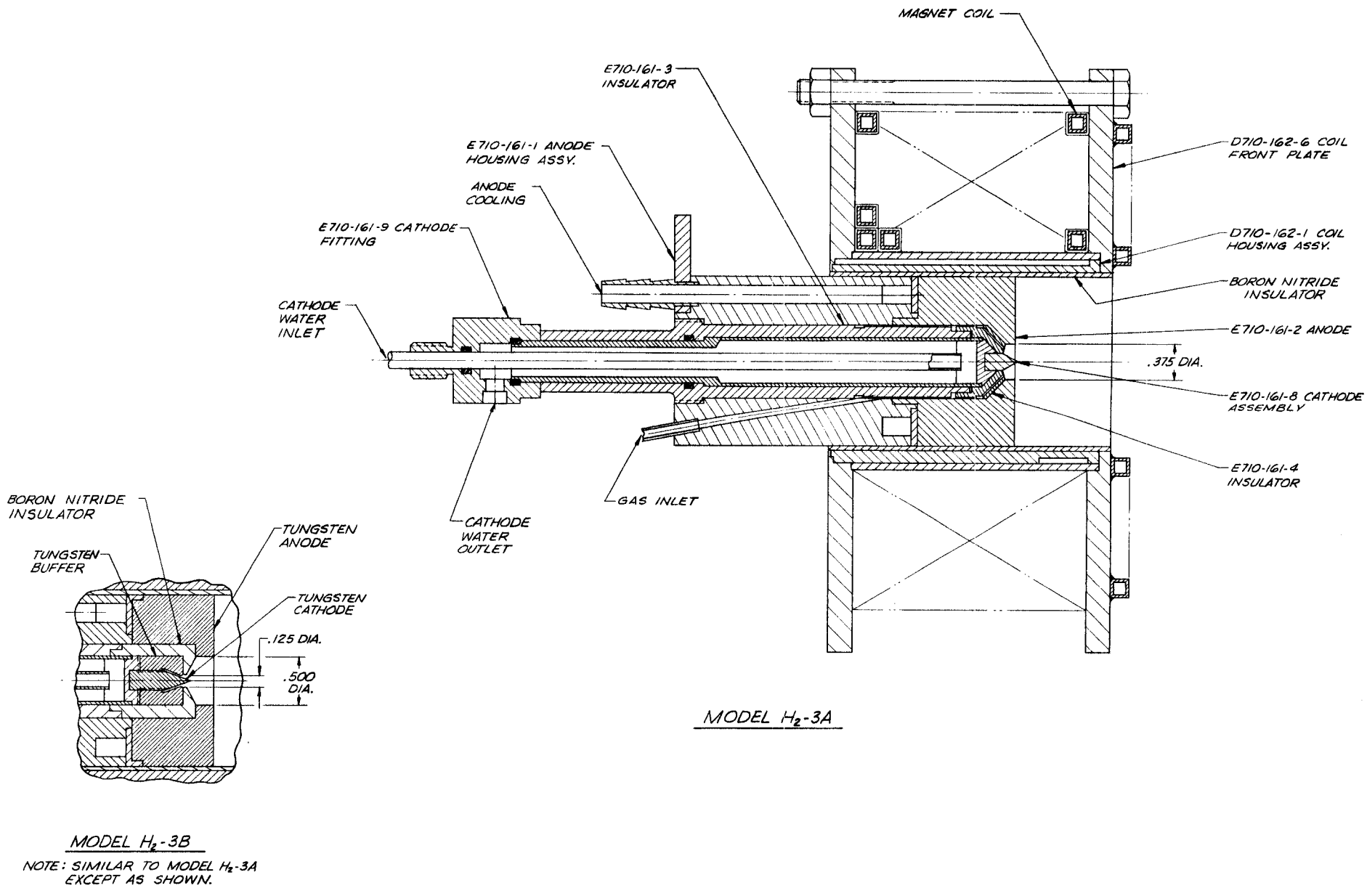

FIG. 6-41 HALL CURRENT ACCELERATOR, MODEL H_2-3

TABLE 6-IV

PERFORMANCE DATA ON EXPERIMENTAL ENGINES

Model	I_A (amperes)	V_A (volts)	P_{IV} (kW)	P_{tank} (mm Hg)	$\dot{m}$ (g/sec)	Thrust (gr)	I_{sp} (sec)	η_o
H_2-3B	100	82	8.20	.04	.0100	6.81	680	.027
	150	83	12.5	.05	.0137	14.8	1080	.061
	200	81	16.2	.05	.0137	18.1	1320	.071
	200	75	15.0	.04	.0100	18.0	1800	.103
	200	83	16.6	1.15	.00167	11.0	6590	.210
	200	68	13.6	.89	.00097	8.75	9010	.279
H_2-2E	150	50	7.5	.035	--	4.11	--	--
	150	41	6.15	.025	.00485	1.35	278	.003
	150	41	6.15	.020	.00485	0.74	152	.001
	150	33	4.45	.017	.00241	0.12	--	--
	150	26	3.90	.018	.00097	0.12	--	--
H_2-2F	150	41	6.15	.041	--	5.09	--	--
	150	37	5.55	.023	.00485	3.25	670	.019
	200	34	6.80	.024	.00485	3.85	794	.022
	200	31	6.20	.020	.00317	2.57	811	.016
	200	28	5.60	.014	.00167	1.03	617	.005
	200	41	8.20	.023	.0040	2.26	565	.007
	200	39	7.80	.022	.0040	6.55	1640	.066
H_2-4A	100	95	9.5	.050	.0188	--	--	--
	100	85	8.5	.030	.010	4.30	430	.010
	100	74	7.4	.023	.005	5.13	1020	.034
	100	72	7.2	.020	.00317	4.91	1310	.043

TABLE 6-IV

PERFORMANCE DATA ON EXPERIMENTAL ENGINES (contd.)

Model	I_A (amperes)	V_A (volts)	P_{IV} (kW)	P_{tank} (mm Hg)	$\dot{m}$ (g/sec)	Thrust (gr)	I_{sp} (sec)	η_o
H_2-4B	100	77	7.7	.040	.020	--	--	--
	100	71	7.1	.028	.00545	6.43	1180	.051
	100	70	7.0	.024	.00375	6.18	1650	.070
	100	72	7.2	.019	.0024	5.23	2180	.076
	100	76	7.6	.012	.00167	5.20	3110	.088
	100	88	8.8	.012	.00097	5.81	5990	.190
	100	74	7.4	--	.0078	--	--	--
	100	73	7.3	.029	.0078	--	--	--
	100	70	7.0	.021	.004	--	--	--
	100	75	7.5	.014	.00233	--	--	--
	100	87	8.7	.009	.00097	--	--	--
	120	84	10.1	.008	.00097	--	--	--
	120	83.5	10.0	.008	.00097	--	--	--
H_2-4B	120	83.5	10.0	.010	.00097	--	--	--
	120	84	10.1	.010	.00097	--	--	--
	120	84	10.1	.010	.00097	--	--	--
	100	84	8.4	.035	--	2.78	--	--
	100	69.5	6.95	.019	.0024	2.72	1130	.021
	100	66	6.6	.011	.00097	2.36	2430	.042
	100	67	6.7	.012	.00097	2.48	2560	.045
	120	66	7.9	.011	.00097	3.13	3230	.061

TABLE 6-IV

PERFORMANCE DATA ON EXPERIMENTAL ENGINES (contd.)

Model	I_A (amperes)	V_A (volts)	P_{IV} (kW)	P_{tank} (mm Hg)	$\dot{m}$ (g/sec)	Thrust (gr)	I_{sp} (sec)	η_o
H_2-4B	140	66	9.2	.011	.00097	3.53	3640	.067
	160	68	10.5	.010	.00097	2.66	2740	.033
	140	66	9.2	.011	.00097	4.08	4210	.090
H_2-4C	100	67.5	6.75	.010	.00097	1.83	1870	.024
	140	67	9.38	.011	.00097	3.46	3540	.062
	160	65	10.4	.011	.00097	3.70	3780	.065
	180	66	12.0	.012	.00097	7.81	7990	.249
	200	66.5	13.3	.012	.00097	5.34	5460	.104
H_2-4D	100	89.5	8.95	.024	.0040	8.25	2060	.091
	100	84	8.40	.020	.0024	9.66	4030	.222
	100	84.5	8.45	.012	.00097	--	--	--
	100	85.5	8.55	.010	.00097	7.73	7960	.346
	100	87	8.70	.013	.00097	5.23	5390	.155
	120	80	9.60	.010	.00097	5.50	5670	.155
	120	79	9.48	.010	.00097	8.64	8910	.389
	140	79	11.1	.010	.00097	10.64	10970	.505
H_2-4E	100	78	7.80	.012	.00097	3.14	3230	.062
	140	80.5	11.3	.012	.00097	5.54	5710	.134
	140	81.5	11.4	.014	.00097	5.86	6040	.149
	140	82	11.5	.014	.00097	7.53	7760	.244

TABLE 6-IV

PERFORMANCE DATA ON EXPERIMENTAL ENGINES (contd.)

Model	I_A (amperes)	V_A (volts)	P_{IV} (kW)	p_{tank} (mm Hg)	$\dot{m}$ (g/sec)	Thrust (gr)	I_{sp} (sec)	η_o
H_2-4E	140	83	11.6	.013	.00097	7.66	7900	.249
	140	83.5	11.7	.010	.00097	7.14	7360	.216
	140	83	11.6	.011	.00097	6.63	6840	.186
	140	81.5	11.4	.014	.00097	5.93	6110	.152
	140	82.5	11.6	.013	.00097	7.34	7570	.231
	140	82.5	11.6	.013	.00097	7.98	8230	.272
	140	82	11.5	.013	.00097	8.62	8880	.320
	140	81.5	11.4	.011	.00097	8.62	8880	.322
H_2-4E	140	81.5	11.4	.011	.00097	8.62	8880	.322
	140	82	11.5	.010	.00097	8.04	6660	.278
	140	82	11.5	.010	.00097	7.98	8230	.274
	140	82	11.5	.010	.00097	7.85	8090	.265
	140	79.5	11.1	.010	.00097	7.66	7900	.260
	140	81.5	11.4	.010	.00097	7.21	7430	.224
	140	82	11.5	.010	.00097	7.02	7230	.212
	140	82	11.5	.010	.00097	7.98	8230	.274
	140	82	11.5	.011	.00097	7.02	7230	.212
	140	82	11.5	.010	.00097	6.37	6570	.175
H_2-4F	140	71	9.94	.011	.00097	7.84	8076	.297

Note: Magnet current (I_M) = 500 amps throughout (center-line field of about 3000 gauss).

where p_c is the pressure at the cathode, $\dot{m}$ is mass flow rate, h_o is stagnation enthalpy of the gas, A_A is the area of the anode orifice, and Ψ is a "flow coefficient" which is close to unity. If the mass flow is fixed, then the pressure at the cathode can be increased by increasing the stagnation enthalpy of the gas at the exit and by decreasing the cross sectional area of the exit orifice. The enthalpy of the gas at the orifice can be increased by moving the cathode back from the orifice. However, a limiting enthalpy is soon attained, whose value is controlled by the wall heat flux rate to the anode (Ref. 8). Model H_2-2E was accordingly designed and built with the cathode well back from the orifice and the orifice itself reduced from 1/2 in. to a diameter of 1/8 in. (Fig. 6-42). This engine operated well at very low mass flow rate but developed very little thrust (Table 6-IV, Model H_2-2E). The low thrust was thought to be caused by friction forces on the gas as it flowed through the long anode orifice. Accordingly, the length of the orifice was reduced, as shown in the insert of Fig. 6-42. Tests on this modified engine indicated that more thrust was developed, but the overall performance was still very poor (Table 6-IV, Model H_2-2F). It was concluded that the small orifice did not allow enough interaction of the current with the electromagnetic field and the small diameter anode approach was thus abandoned.

The next approach to maintaining a high pressure at the cathode was to place a buffer electrode between the anode and cathode. This electrode is electrically insulated from the anode and cathode, but forces the gas and the discharge to flow through a small orifice, thus maintaining the cathode pressure at adequately high values. The technique of buffer design had been worked out previously (Ref. 9).

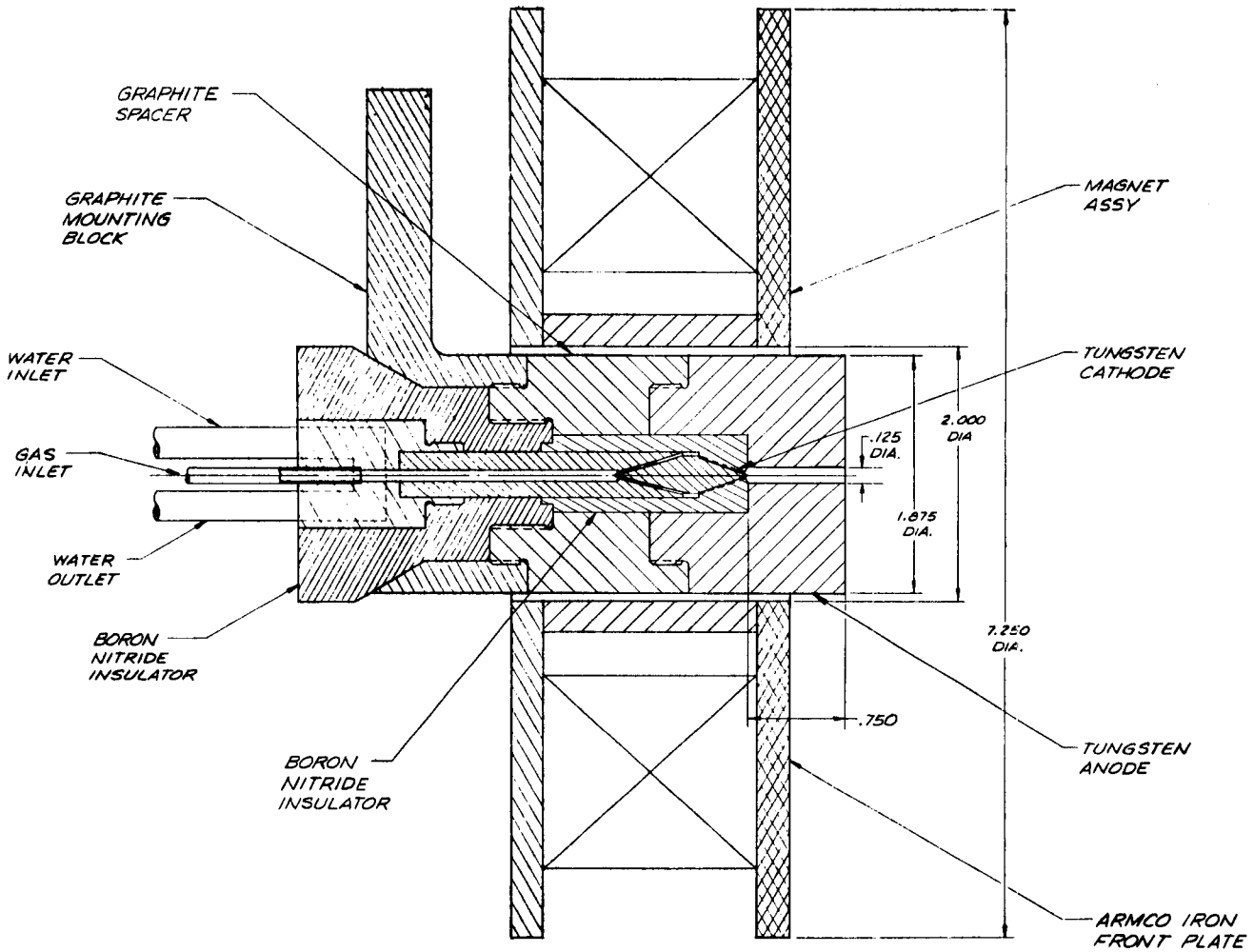

MODEL H_2-2E

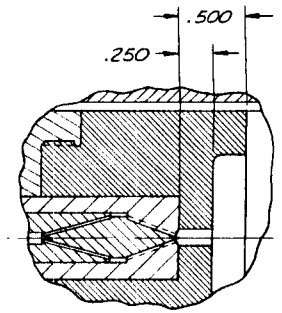

MODEL H_2-2F

NOTE: IDENTICAL TO MODEL H_2-2E EXCEPT AS INDICATED.

FIG. 6-42 HALL CURRENT ACCELERATOR ASSEMBLY, MODELS H_2-2E AND H_2-2F

and the buffer configuration developed at that time was used for this engine. A second magnet was also added to the rear of the engine (Fig. 6-43). It was hoped that by bucking this magnet against the accelerating magnet, the discharge could be channeled through the buffer orifice with little power loss. Initial tests with this configuration indicated that the second magnet had little or no effect on buffer performance and heated excessively. Also, the overall engine performance was still very poor (Table 6-IV, Model H_2-4A). In the next modification, the second magnet was removed and the length of the anode orifice decreased (Fig. 6-44). The performance of this engine was quite good at low mass flow rate and low tank pressure. (Table 6-IV, Model H_2-4B). For this reason only minor changes were subsequently made in the configuration. These modifications are illustrated in Fig. 6-44.

6.3.1 Low Pressure Tests

A 10-kW buffered-cathode Hall current accelerator of the design shown in Fig. 6-44 was delivered to the Lewis Research Center for testing at low ambient (tank) pressures. The accelerator was installed on a thrust stand in a test facility equipped with twenty 36-in. diffusion pumps and tested at pressures as low as 5×10^{-5} mm Hg, under the direction of S. Domitz (Ref. 3). The data from these tests are presented in Tables 6-V and 6-VI.

The thrust stand calibrations were performed by dead-weight loading to determine sensitivity and by a shorting test to determine the interaction of the arc and magnet currents with the tank and fixed current leads. The effect of the Hall currents upon the thrust stand calibration is discussed in Section 6.5. Drift and zero shifts of the thrust reading raised some doubt as to absolute accuracy. However, repeated dead-weight loading of the thrust stand with the accelerator on and off gave reproducible increments in the thrust reading. Thus, the precision of the thrust readings is thought to be quite good. The tank pressure was measured using thermocouple and ionization gauges. A factor of two was used throughout in order to correct the air calibration of those gauges for use in hydrogen.

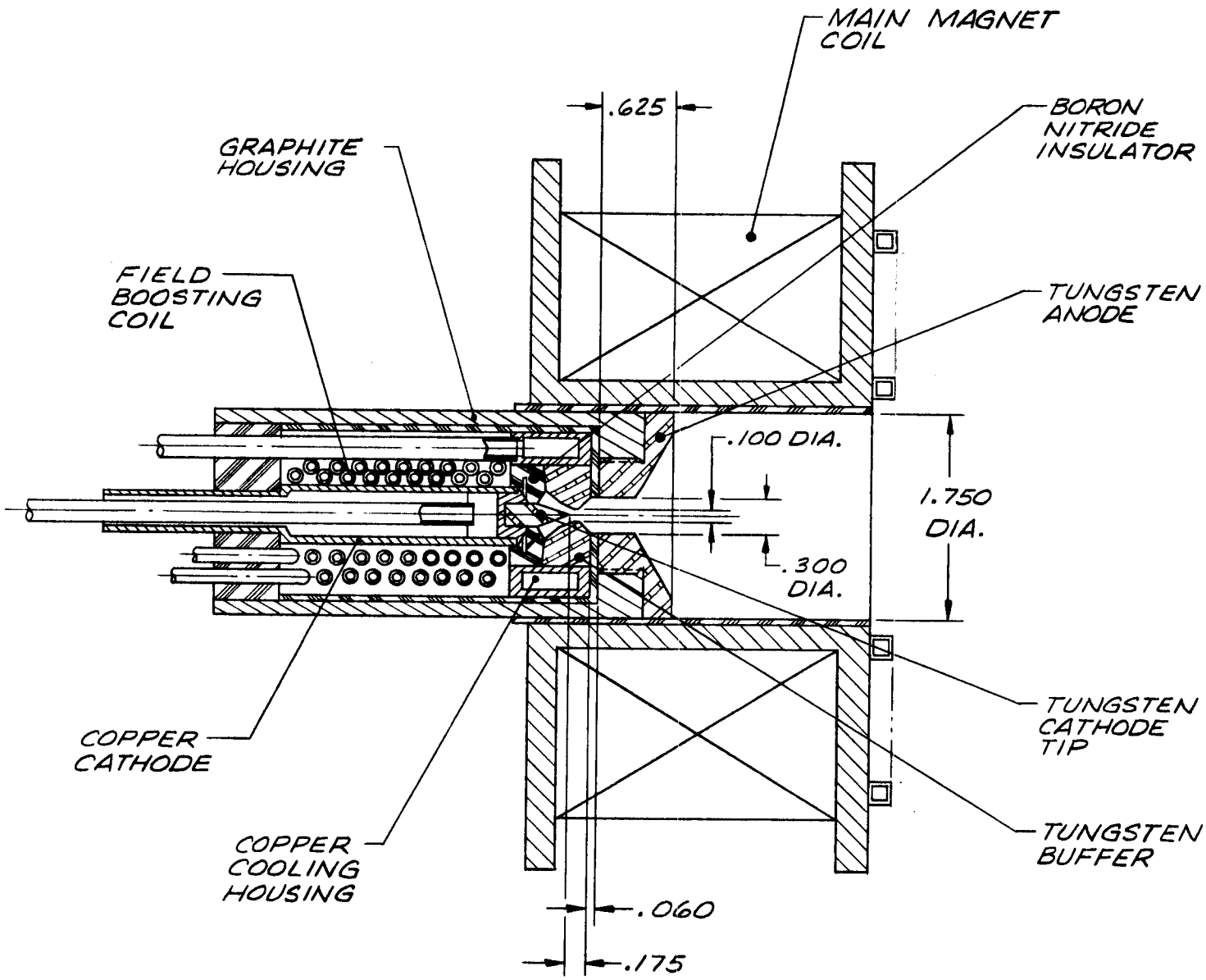

FIG. 6-43 HALL CURRENT ACCELERATOR, MODEL H_2-4A

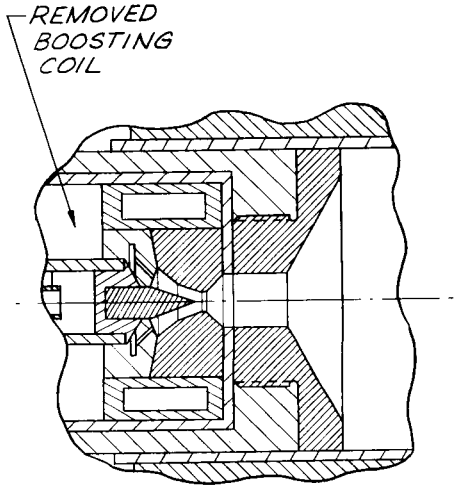

MODEL H_2-4B

NOTE: IDENTICAL TO MODEL H_2-4A EXCEPT AS INDICATED.

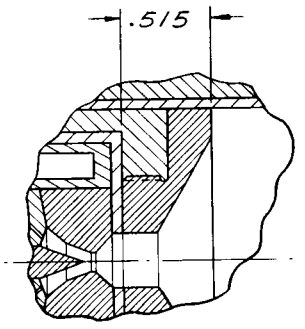

MODEL H_2-4C

NOTE: IDENTICAL TO MODEL H_2-4B EXCEPT AS INDICATED.

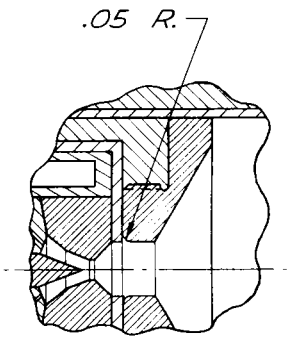

MODEL H_2-4D

NOTE: IDENTICAL TO MODEL H_2-4C EXCEPT AS INDICATED.

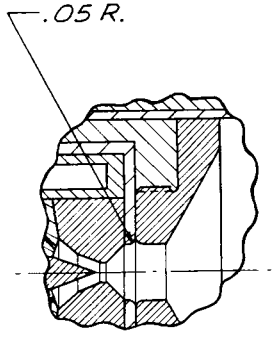

MODEL H_2-4F

NOTE: IDENTICAL TO MODEL H_2-4E EXCEPT AS INDICATED.

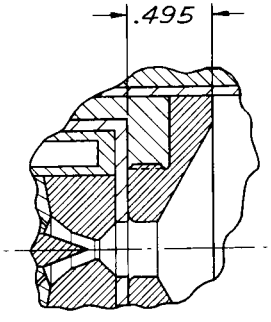

MODEL H_2-4E

NOTE: IDENTICAL TO MODEL H_2-4D EXCEPT AS INDICATED

FIG. 6-44 HALL CURRENT ACCELERATOR ASSEMBLY, MODELS H_2-4B, H_2-4C, H_2-4D, H_2-4E, AND H_2-4F

TABLE 6-V

PERFORMANCE OF 10-kW HALL CURRENT ACCELERATOR

COMPARED AT HIGH AND LOW AMBIENT PRESSURES

$\dot{m}$ (mg/sec)	I_a (amperes)	I_m (amperes)	P_{IV} (kW)	P_t (mm Hg)	T (gr)	I_{sp} (sec)	η_o
*1.24	140	500	11.5	1×10^{-2}	8.6	6900	0.25
1.04	140	500	9.52	1.15×10^{-2}	4.0	3850	0.078
1.04	140	500		8×10^{-5}	4.4	4231	
1.4	120	500	7.56	1×10^{-3}	3.3	2360	0.049
1.4	120	500	7.69	5×10^{-5}	3.1	2210	0.043

*Test at EOS.

TABLE 6-VI

LOW AMBIENT PRESSURE PERFORMANCE DATA FOR 10-kW HALL CURRENT ACCELERATOR

$\dot{m}$ (mg/sec)	I_a (amperes)	I_m (amperes)	P_{IV} (kW)	p_t^* (mm Hg)	T (gr)	I_{sp} (sec)	η_o^{**}
1.8	98	490	6.76	28×10^{-5}	3.3	1830	0.043
1.8	99	480	6.93	28×10^{-5}	4.3	2410	0.072
1.8	100	500	7.00	5.6×10^{-5}	4.3	2390	0.070
1.8	122	500	8.54	5.0×10^{-5}	4.9	2740	0.076
1.7	120	500	8.40	4.8×10^{-5}	4.9	2900	0.082
1.6	119.5	500	8.37	4.8×10^{-5}	5.1	3190	0.093
1.6	140	500	9.80	4.8×10^{-5}	5.8	3590	0.101
1.5	140	504	9.80	4.2×10^{-5}	5.2	3470	0.088
1.2	140	505	10.0	4.0×10^{-5}	4.8	3970	0.091
1.2	118	500	8.44	3.6×10^{-5}	3.8	3150	0.068
1.2	101	503	7.47	2.6×10^{-5}	2.5	2050	0.032
1.0	97	501	7.76	2.8×10^{-5}	2.2	2240	0.031
1.0	120.5	500	8.92	2.8×10^{-5}	3.1	3060	0.050
1.0	140	500	9.52	8.0×10^{-5}	4.4	4400	0.098
1.4	120	500	7.92	5.0×10^{-5}	3.1	2210	0.042
1.4	120	500	8.04	4.6×10^{-5}	3.5	2500	0.052
1.4	120	500	8.04	---	--	--	--
1.2	120	500	9.00	3.4×10^{-5}	3.1	2580	0.043

* Twice average reading of ionization gauges to correct for H_2.

** Exclusive of magnet power of 6-6.25 kW at 500 A.

The most significant results of the tests are listed below:

1. To within the precision of the thrust measurement, the thrust did not change with ambient pressure over the range from 10^{-2} to 5×10^{-5} mm Hg (Table 6-V).
2. At constant arc current, magnetic field strength, and mass flow rate, the applied voltage did not change appreciably with tank pressure (Table 6-V).
3. Under the same operating conditions, the absolute magnitude of the thrust was about 40 percent lower than that observed at the EOS facility (Table 6-V).
4. As the ambient pressure was lowered to 10^{-3} mm Hg, the anode and cathode jets changed in appearance and became distinctly separated. The anode jet flared out from the anode for a distance of about 6 inches. The cathode jet increased in length to about 8 feet and curved toward the tank wall. The arc formed by the cathode jet appeared to have a radius of curvature of perhaps 12 feet and ended near the tank wall. At pressures less than 10^{-3} mm Hg, the appearance of the jet did not change.
5. Reversing magnetic field polarity had no effect upon accelerator performance or the appearance of the jet.

The fact that thrust and voltage were independent of tank pressures as low as 5×10^{-5} mm Hg indicates that the possible entrainment of ambient gas into the exhaust stream at high tank pressures does not appreciably affect performance data. An estimate of the maximum possible entrained mass flow may be made by computing the number of particles which enter the interaction region by free diffusion:

$$\dot{m}_e = A \frac{m_a n_a v_{th}}{3} = \frac{Ap}{\sqrt{T}} \sqrt{\frac{8 m_a}{k}} \quad \text{(in mks units).} \qquad (4)$$

For hydrogen at temperatures above $300^{\circ}K$,

$$\dot{m}_e \leq 4.4 \times 10^{-3} Ap ,$$

where $\dot{m}_e$ is in g/sec, A is in cm^2 and p is in mm Hg. Thus, at a supplied mass flow rate of $\dot{m}_s = 10^{-3}$ g/sec and an ambient pressure of 5×10^{-5} mm Hg, the ratio of total to supplied mass flow rates would be

$$\frac{\dot{m}_T}{\dot{m}_s} = \frac{\dot{m}_s + \dot{m}_e}{\dot{m}_s} = 1 + 2.2 \times 10^{-4} A \ . \qquad (5)$$

If it is estimated that the interaction region coincides roughly with the luminous portion of the anode jet, $A \leq 750$ cm^2 and $\dot{m}_T/\dot{m}_s \leq 1.15$. Even if the above estimates are somewhat in error, it appears certain that entrainment of ambient gas has no major effect upon accelerator performance.

The difference between the absolute magnitude of the thrust observed in the Lewis Research Center tests and that which was observed at EOS is not fully understood. The large zero drift and shifts of the thrust stand at LRC leads one to suspect the accuracy of those measurements. However, other factors may be responsible for the observed discrepancy.

The long cathode jet which was observed at ambient pressures less than 10^{-3} mm Hg suggests the possibility that a portion of the arc current was being carried by a ground loop which bypassed the accelerator anode. Though direct measurement of the anode and cathode currents close to the accelerator were not made, the two currents were equal just outside the tank. This indicated that any possible ground loop was closing within the tank. Experiments were performed in which the anode was shorted to the tank; the current carried by the short increased from practically zero at 10^{-2} mm Hg to about 40 amperes at pressures of 10^{-3} mm Hg and less. The applied arc current was 120 amperes during these tests. Thus, even with a direct short from tank to anode, the ground loop current was only 1/3 of the applied current. Closing the tank-to-anode short caused the cathode jet to curve more sharply so that it approached the tank wall closer to the accelerator.

However, even when the short was carrying 40 amperes, no arc attachment of the cathode jet to the tank wall was observed. By turning off various sets of the diffusion pumps in turn, it was determined that the curvature of the cathode jet was not affected by the gas flow pattern in the tank.

A possible interpretation of the long, curved cathode jet is the following. The probability of volume recombination of ions and electrons is quite small and much of the recombination might occur when the ions accelerated in the anode jet strike the tank wall. The wall is supplied with electrons accelerated in the cathode jet. If the directed kinetic energies of the electrons and ions were different downstream of the accelerator, there would be a tendency for electrons to bend toward the tank more sharply than the ions. Since the accelerated electrons and ions would continue to flow downstream in a space environment, regardless of the rate of recombination, the curvature of the cathode jet observed in a vacuum tank test will not occur in space.

6.4 Tests of Various Propellants

A series of experiments was performed with hydrogen, helium, nitrogen, and argon using the 10-kW accelerator shown in Fig. 6-45 in an attempt to determine the effects of atomic weight and ionization potential on accelerator performance. The results of these tests are presented in Tables 6-VII and 6-VIII and Figs. 6-46 through 6-51.

The effect of mass flow rate on thrust for the various propellants is shown in Figs. 6-46 and 6-47. The data indicate that thrust increases with mass flow for each propellant, though sufficient data are not available to determine the functional dependence accurately. Except for a small difference with nitrogen, the thrust appears to be independent of propellant type. The fact that the thrust approaches a positive intercept as the mass flow is reduced toward zero may be explained by the fact that electromagnetic forces should be fairly independent of mass flow down to very small flow rates. The increase in thrust with increasing mass flow may be caused by an increase in aerodynamic forces. The aerodynamic thrust may be approximated by

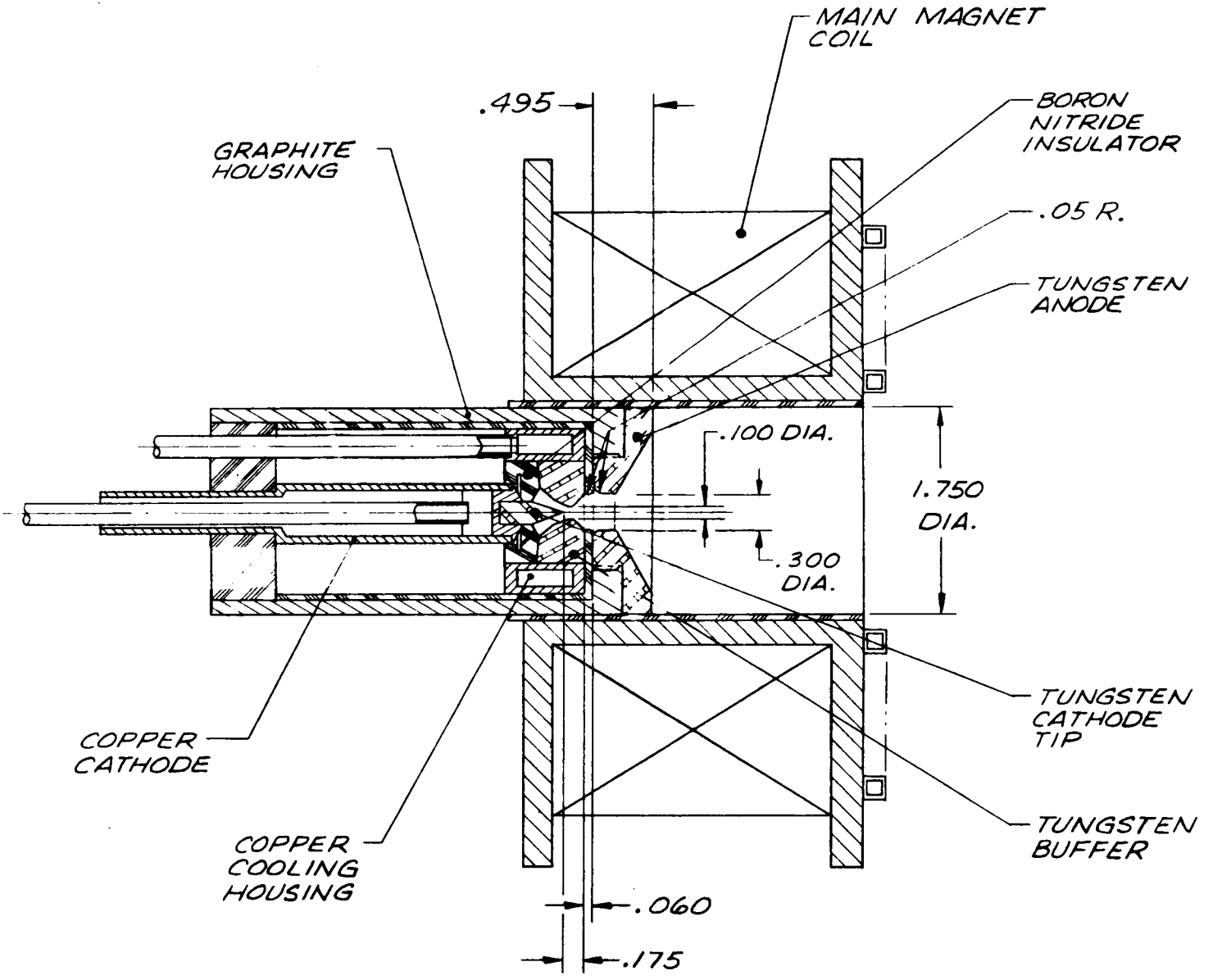

FIG. 6-45 HALL CURRENT ACCELERATOR, MODEL H_2-4E

TABLE 6-VII

PERFORMANCE DATA FOR 10-kW ACCELERATOR WHEN OPERATED WITH ARGON PROPELLANT

$\dot{m}$ (mg/sec)	I_a (amperes)	I_m (amperes)	P_{IV} (kW)	p_t (mm Hg)	T (gr)	I_{sp} (sec)	η_o
13.6	100	500	4.0	0.018	11.2	820	0.11
4.55	100	500	5.10	0.013	5.51	1210	0.063
4.55	100	500	5.60	0.013	6.32	1390	0.075
3.63	100	500	6.10	0.010	5.20	1430	0.059
2.93	100	500	6.60	0.012	5.06	1730	0.064
2.93	100	500	7.00	0.010	4.35	1490	0.044
2.31	100	500	7.30	0.012	5.39	2330	0.083
2.31	100	500	7.60	0.009	4.72	2040	0.061
4.55	125	500	7.38	0.014	7.09	1560	0.072
2.31	125	500	9.38	0.011	6.30	2730	0.081
2.31	125	500	9.63	0.010	6.33	2740	0.086
17.0	140	500	8.12	0.030	15.6	920	0.085
11.4	140	500	8.33	0.016	11.7	1030	0.069
2.31	140	500	10.8	0.010	7.13	3090	0.098
2.31	140	500	10.6	0.010	6.54	2830	0.084
1.71	140	500	12.6	0.02	7.05	4120	0.111
2.31	150	500	11.7	0.011	7.19	3110	0.092

TABLE 6-VIII

PERFORMANCE DATA FOR 10-kW ACCELERATOR WHEN OPERATED WITH NITROGEN AND HELIUM PROPELLANTS

	$\dot{m}$ (mg/sec)	I_a (amperes)	I_m (amperes)	P_{IV} (kW)	P_t (mm Hg)	T (gr)	I_{sp} (sec)	η_o
N_2	40.0	100	500	6.20	0.028	14.33	358	0.040
	3.59	100	500	6.40	0.011	3.73	1040	0.029
	2.83	100	500	6.40	0.011	2.63	929	0.017
	2.85	120	500	8.04	0.012	3.35	1180	0.024
	40.0	140	500	8.26	0.029	20.5	513	0.061
	18.7	140	500	7.98	0.031	14.0	746	0.063
	8.14	140	500	7.84	0.013	7.19	883	0.039
	3.62	140	500	8.4	0.012	4.60	1270	0.033
	3.59	140	500	7.14	0.012	4.74	1320	0.042
	2.95	140	500	9.10	0.010	4.45	1510	0.035
	2.30	140	500	9.80	0.015	5.22	2270	0.058
He	11.0	140	500	8.61	0.065	12.6	1140	0.081
	5.97	140	500	8.40	0.050	10.4	1750	0.104
	4.7	140	500	8.68	0.040	7.84	1640	0.071

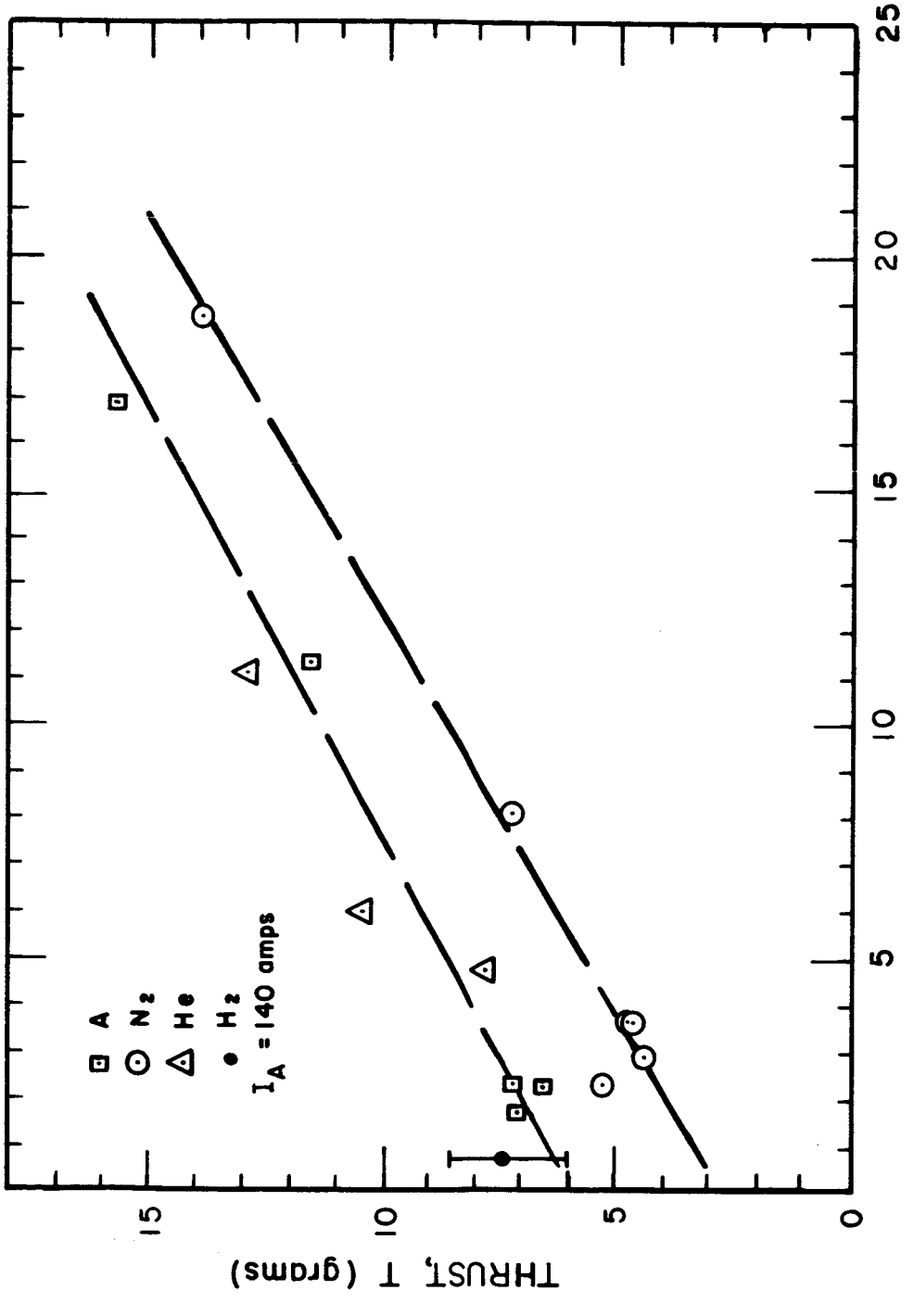

FIG. 6-46 EFFECT OF MASS FLOW RATE ON THRUST OF 10-kW ACCELERATOR WITH VARIOUS PROPELLANTS AND ARC CURRENT OF 140A

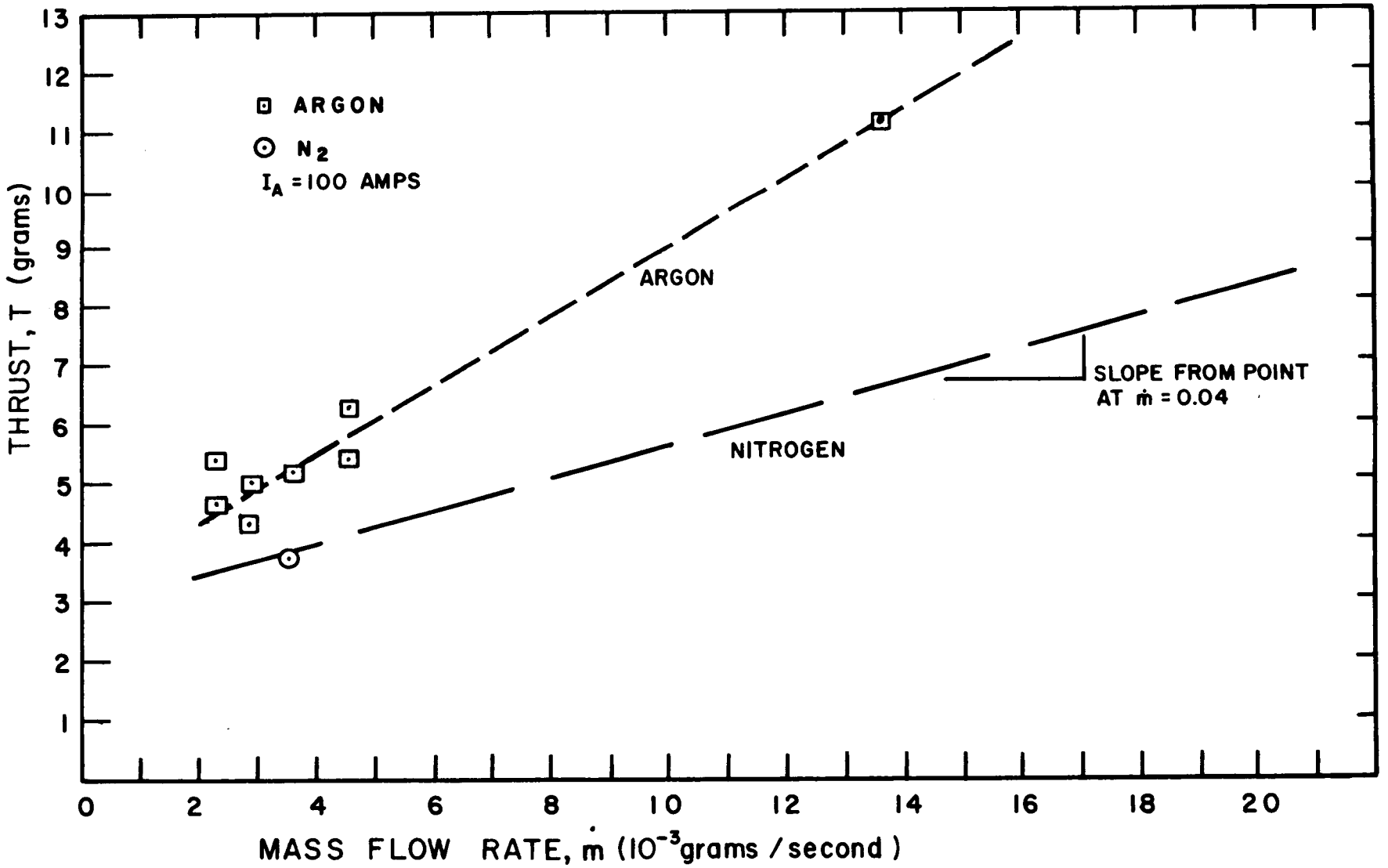

FIG. 6-47 EFFECT OF MASS FLOW RATE ON THRUST OF 10-kW ACCELERATOR WITH VARIOUS PROPELLANTS AND ARC CURRENT OF 100A

$$p_o A_{exit} = \left(\frac{\gamma-1}{\gamma k} h_{exit}\right)^{1/2} \dot{m} \ (1.67 \times 10^{-12}) \ \text{(in mks units)}, \qquad (6)$$

where h_{exit} is the static enthalpy of the gas, excluding ionization and dissociation energy. If h_{exit} varied inversely with the mass flow rate, the aerodynamic forces would be proportional to the square root of the mass flow rate and independent of atomic weight, or roughly of the same form as the data presented in Figs. 6-46 and 6-47. The effect of mass flow on thrust was not observed with the accelerator configuration tested during the first quarter (Ref. 10).

The acceleration efficiency, η_b, is plotted in Fig. 6-48 as a function of specific impulse for each of the propellants. The rise in efficiency at very low values of specific impulse is mainly caused by the fact that, in computing η_b, the stagnation enthalpy of the stored gas is not added to the supplied electrical energy. Above about 1000 seconds, the efficiency begins to increase with I_{sp}, as has been observed with hydrogen, lithium (Ref. 11), and NH_3 (Ref. 12). The ratio of observed acceleration efficiency to frozen flow efficiency (based upon complete single ionization) for the various propellants is plotted in Fig. 6-49 as a function of I_{sp}. For reference, the frozen flow efficiency, η_{fr}, is shown in Fig. 6-50 as a function of I_{sp} for each of the propellants. Though the present accelerator was developed for use with hydrogen and the value of η_b/η_{fr} at a given I_{sp} was largest for hydrogen, there is not sufficient data at this time to determine the extent of accelerator redesign required to improve performance with the other propellants. The difference in performance obtained with the various propellants may be inherent in the acceleration mechanisms, and may be affected very little by changes in engine configuration.

Figure 6-51 is a graph of the observed values of V_{KE}/V_o as a function of $1/\Psi$ for each propellant. The symbol V_{KE} designates the equivalent voltage required to accelerate a singly charged ion to the observed average stream velocity:

$$V_{KE} = \frac{1}{e}\left(\frac{1}{2} m_i\right)\left(\frac{T}{\dot{m}}\right)^2 \ \text{(in volts)} \qquad (7)$$

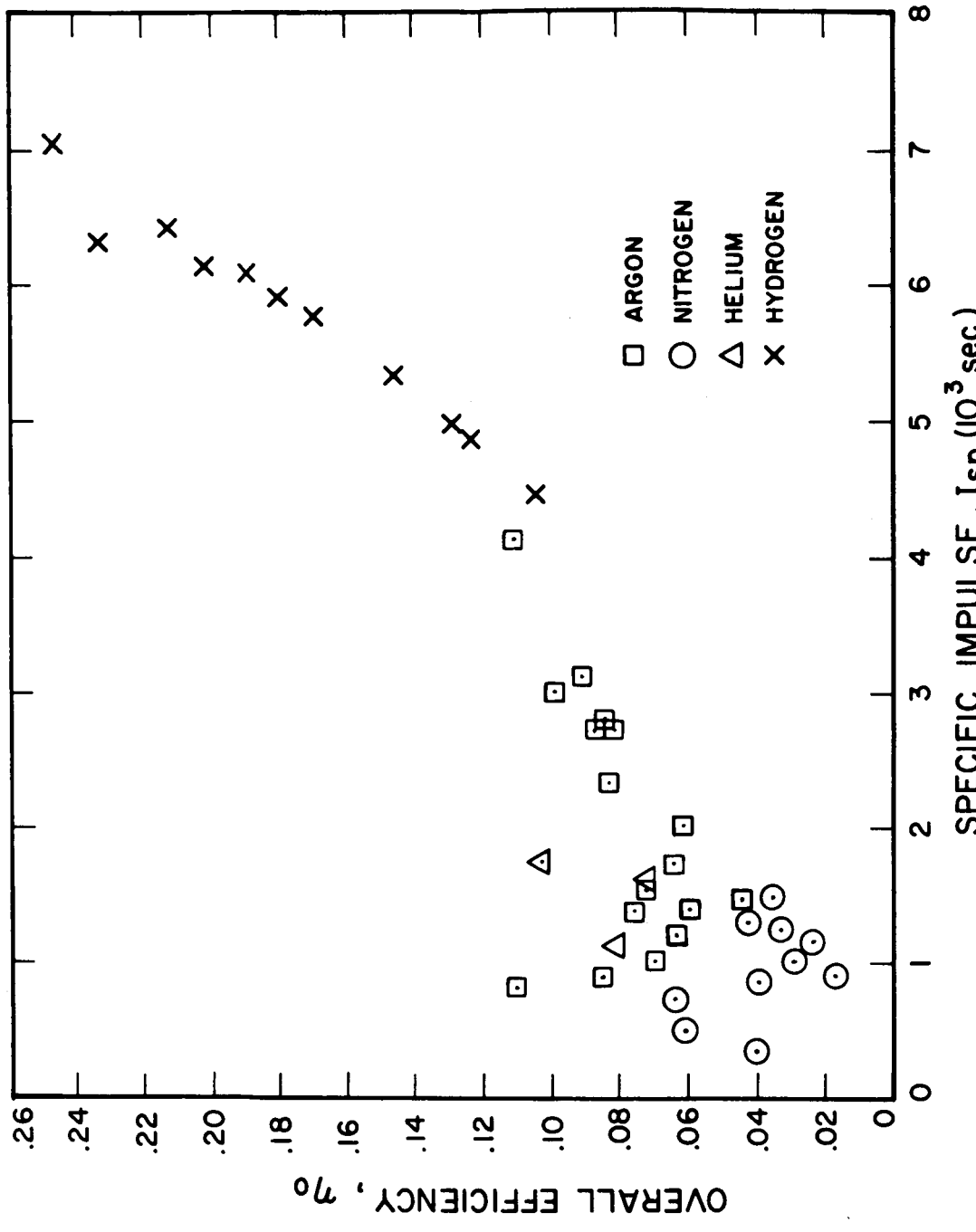

FIG. 6-48 ACCELERATION EFFICIENCY AS A FUNCTION OF SPECIFIC IMPULSE

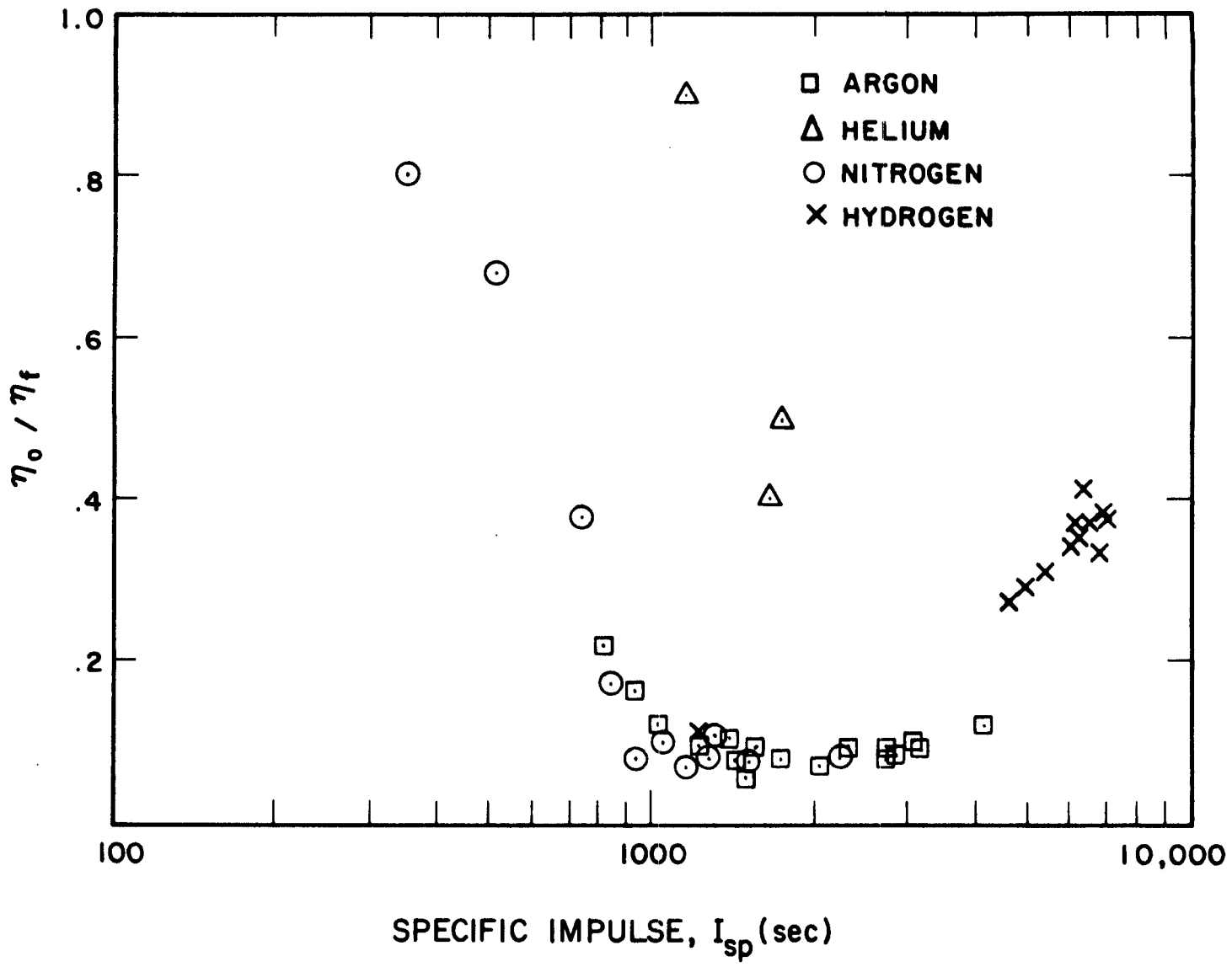

FIG. 6-49 RATIO OF ACCELERATION AND FROZEN FLOW EFFICIENCIES AS A FUNCTION OF SPECIFIC IMPULSE

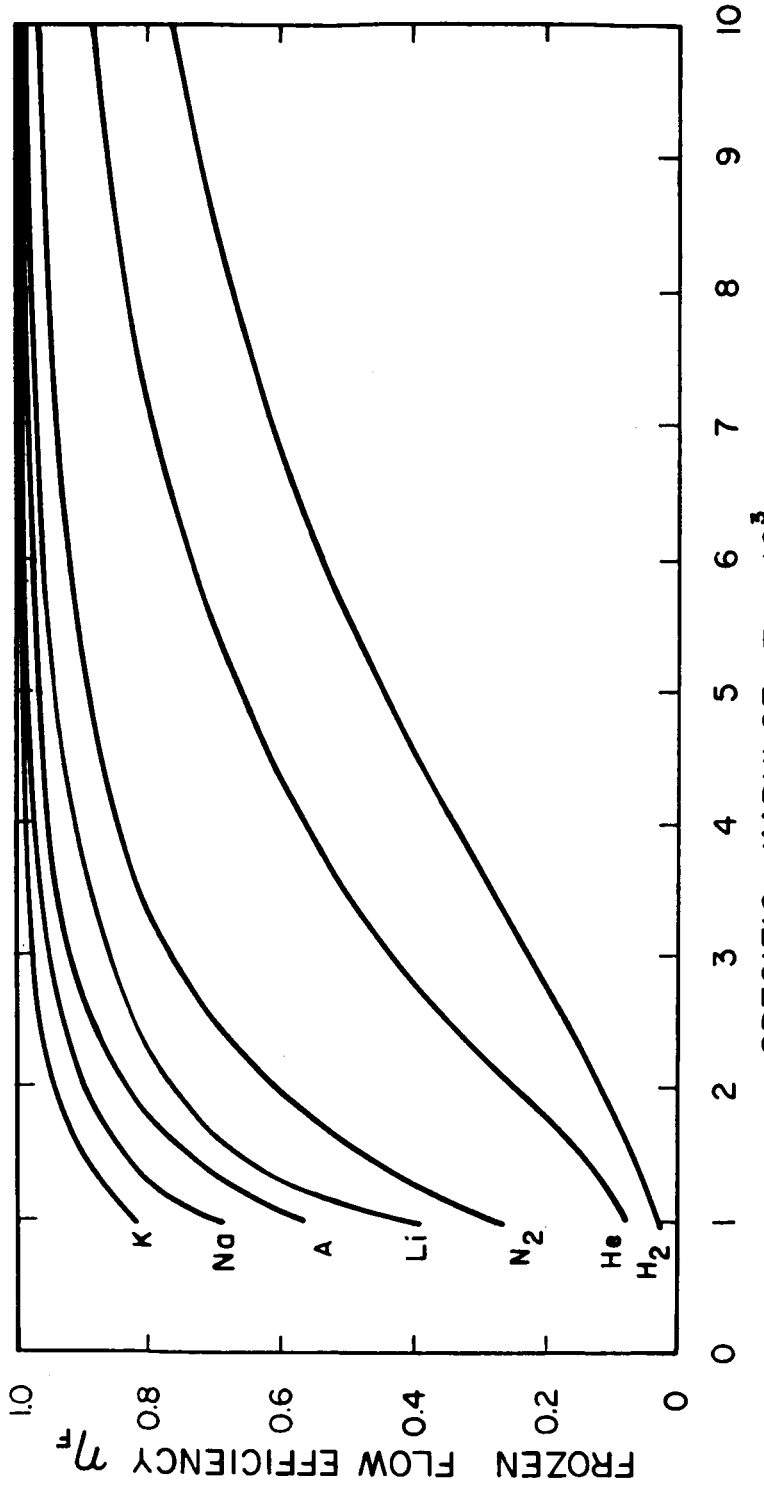

FIG. 6-50 FROZEN FLOW EFFICIENCY AS A FUNCTION OF SPECIFIC IMPULSE FOR VARIOUS PROPELLANTS

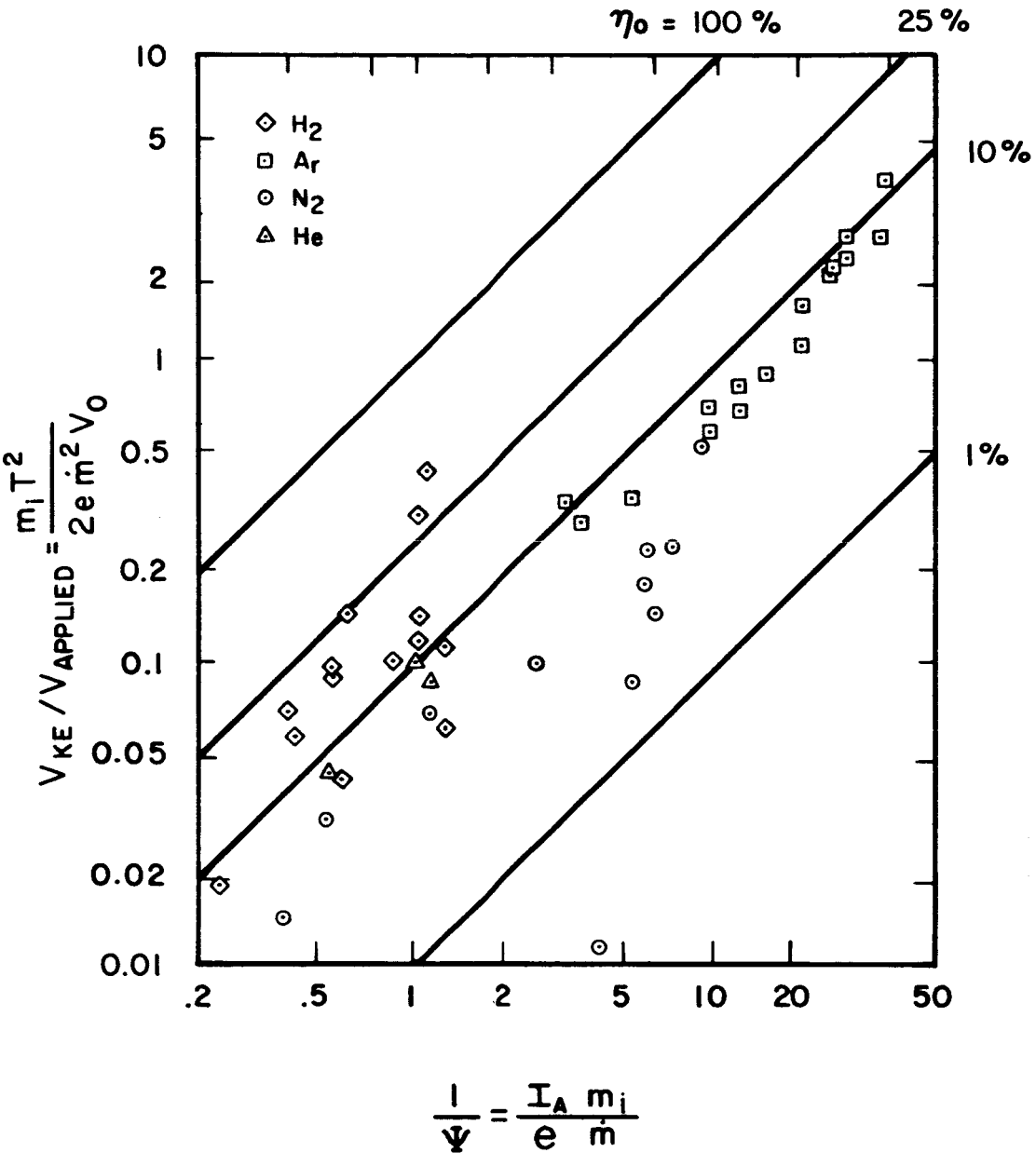

FIG. 6-51 RATIO OF VOLTAGE NECESSARY TO ACCELERATE A FIRST ION TO OBSERVED STREAM VELOCITY TO APPLIED VOLTAGE AS A FUNCTION OF DIMENSIONLESS RATIO OF MASS FLOW TO ARC CURRENT

Applied voltage is designated by V_o and Ψ is the dimensionless ratio of mass flow to arc current:

$$\Psi = \frac{e\,\dot{m}}{m_i\,I_A} \tag{8}$$

The acceleration efficiency may be written as

$$\eta_b = \frac{\left(\frac{T^2}{2\dot{m}}\right)}{I\,V_o} = \Psi(V_{KE}/V_o). \tag{9}$$

Since the kinetic energy flux of the stream is a minimum when the velocity distribution is uniform, the first law of thermodynamics imposes the requirement that η_b as defined in Eq. 9 be less than unity (so long as tne enthalpy flux of the supplied gas is negligible in comparison to the electrical power). It can be seen from Fig. 6-51 that none of the data violate that condition. However, the data for argon indicate that the ions are being accelerated to velocities higher than would be attained after a drop through the total applied voltage ($V_{KE}/V_o > 1$). Anomalous values have also been observed in argon by other experimenters (Refs. 10 and 13). The possible mechanisms which could produce such results are

1. Mass entrainment from surroundings, leading to velocities which are less than $T/\dot{m}$.
2. Multiple ionization. (The highest values of V_{KE}/V_o in Fig. 6-51 would be reduced to less than unity only if fourth ionization occurred.)
3. Alternating current effects.
4. Multiple collisions with electrons which accelerate the ions toward the limiting E/B velocity.

Whether the anomalous results are simply caused by mass entrainment could be determined most readily by testing the device at low tank pressure; a pressure of 10^{-3} mm Hg or less should be sufficient. Since multiple ionization results in larger frozen flow losses, the second mechanism appears undesirable and might be avoided through the use of either hydrogen or an alkali metal with its high second ionization

potential. Either the third or fourth mechanism could be exploited to improve accelerator performance. Alternating current effects might be enhanced by changing the inductance and capacitance of the dc power circuit. The collisional acceleration mechanism might be enhanced by such things as altering the magnetic field configuration to provide additional electromagnetic containment of the anode jet and using a propellant of greater atomic weight. If it is possible to obtain values of V_{KE}/V_o which are greater than unity, it becomes important to definitely identify the responsible mechanisms experimentally in order to optimize accelerator performance. Some progress in this direction has been made analytically by identifying the rotational speed up due to electron collisions as the most likely method of energy exchange from the electrons to the ions.

The tests conducted with the low-power engines have shed some light upon the power scaling laws for the accelerator and upon the design parameters which can improve performance. The results can be summarized as follows:

1. The overall performance of the best low-power engine was poorer than that of the high-power engine. This occurred because the power loss to the engine components of the low-power accelerator was a higher percentage of the overall input power.
2. Of all the gases tested, e.g., hydrogen, helium, argon, and nitrogen, hydrogen exhibited the best accelerator performance. This is probably due to the occurrence of higher electron energies in the other gases, which increases the anode power loss per unit current and leads to the occurrence of multiple ionization.
3. Many electrode configurations were tested in order to obtain stable performance and acceptable efficiency at low mass flow rates. The buffered cathode design was the only one which permitted us to reduce the mass flow rate below 1 milligram/second without injecting gas into the vacuum chamber to keep the ambient pressure up.

6.5 Experimental Anode Studies

A special test apparatus was designed and fabricated for the purpose of studying the anode characteristics of the accelerator. The anode consisted of three identical copper segments which were insulated electrically and thermally from each other (see Fig. 6-52). These segments were connected individually through shunts to the power lead so that the current drawn by each could be measured. The cooling circuit of each was also connected separately to a flowmeter and thermocouple so that the power absorbed by each could be found. A pressure tap was provided in one segment for measuring the pressure in the anode cavity. During some of the tests, the pressure tap was located in the third segment and at other times it was located in the first segment. As closely as could be determined, the pressure was similar at the two positions.

The pressure that was measured in the anode cavity is plotted versus the gas mass flow rate in Fig. 6-53. If we assume that the gas is sonic at the exit orifice, then a value for the exit velocity can be computed from perfect gas theory. As a first order approximation this is given as:

$$\dot{m} = \frac{\gamma}{1 + \gamma} \frac{p_o A_t}{u}$$

or

$$u_{exit} = 3.65 \frac{p}{\dot{m}} \frac{m}{sec}$$

where p is given in m.m. of mercury and $\dot{m}$ is in gm/sec. A plot of these computed values is presented in Fig. 6-54.* These values are considered to be only approximate, but they do indicate some interesting and important trends. First, a considerable amount of energy is transferred to the gas inside of the anode cavity. Second, the energy per particle transferred inside of the anode from the discharge to the gas appears to go through a maximum as the mass flow is decreased.

In order to investigate this phenomenon further, the information obtained from the energy balance can be used. If we assume that all of

* The pressure used in this calculation was 3 m.m. lower than the measured value because of an apparent intercept of 3 m.m. at $\dot{m} = 0$ in Fig. 6-53).

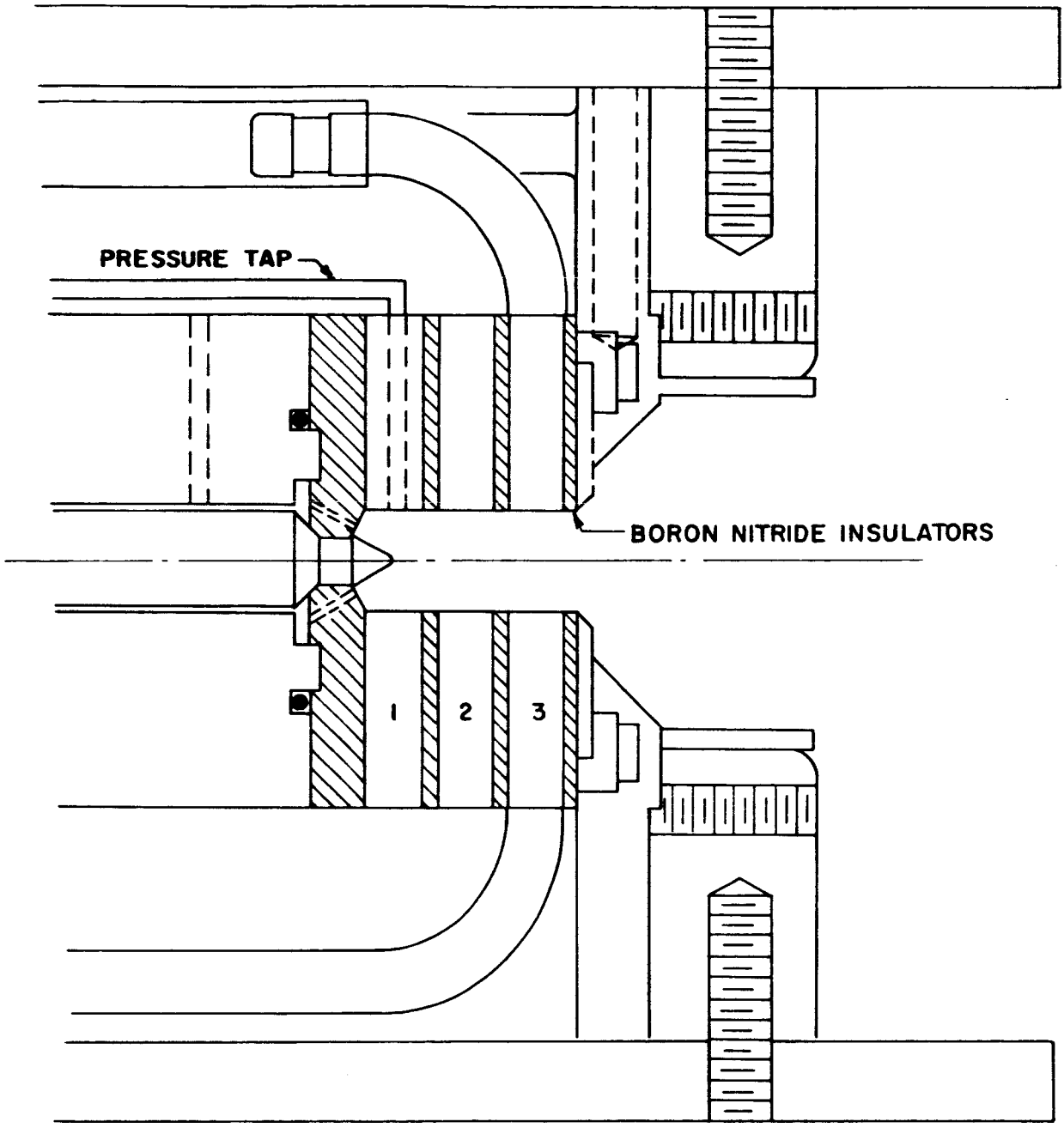

FIG. 6-52 WATER COOLED, SEGMENTED ANODE ACCELERATOR USED IN THE ELECTRODE STUDY TESTS TO DETERMINE CURRENT AND POWER DISTRIBUTIONS AT THE ANODE. THE THREE NUMBERED ANODE SEGMENTS WERE CONNECTED IN PARALLEL TO THE POWER SUPPLY

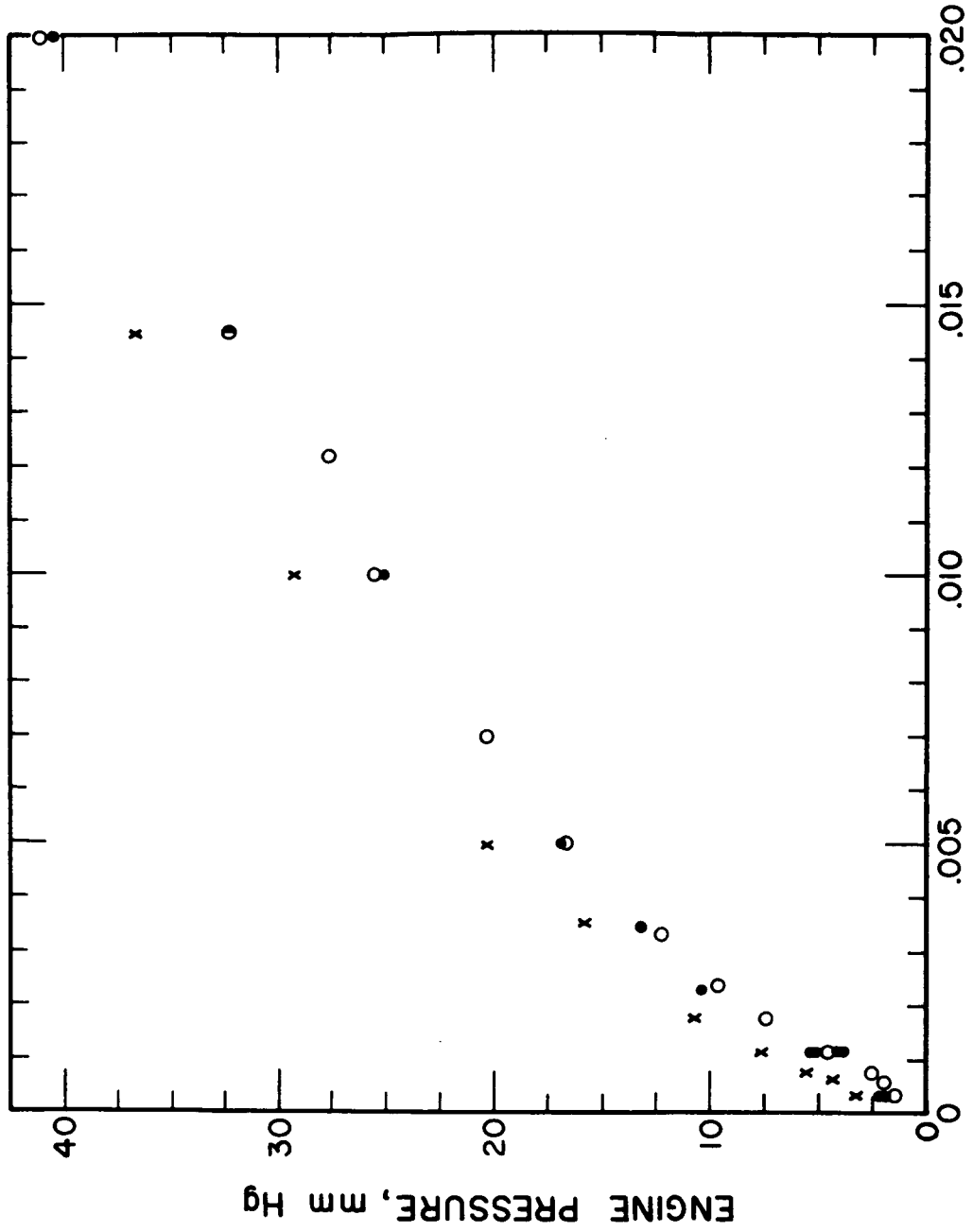

FIG. 6-53 ENGINE PRESSURE VERSUS MASS FLOW RATE FOR SEGMENTED ANODE ACCELERATOR

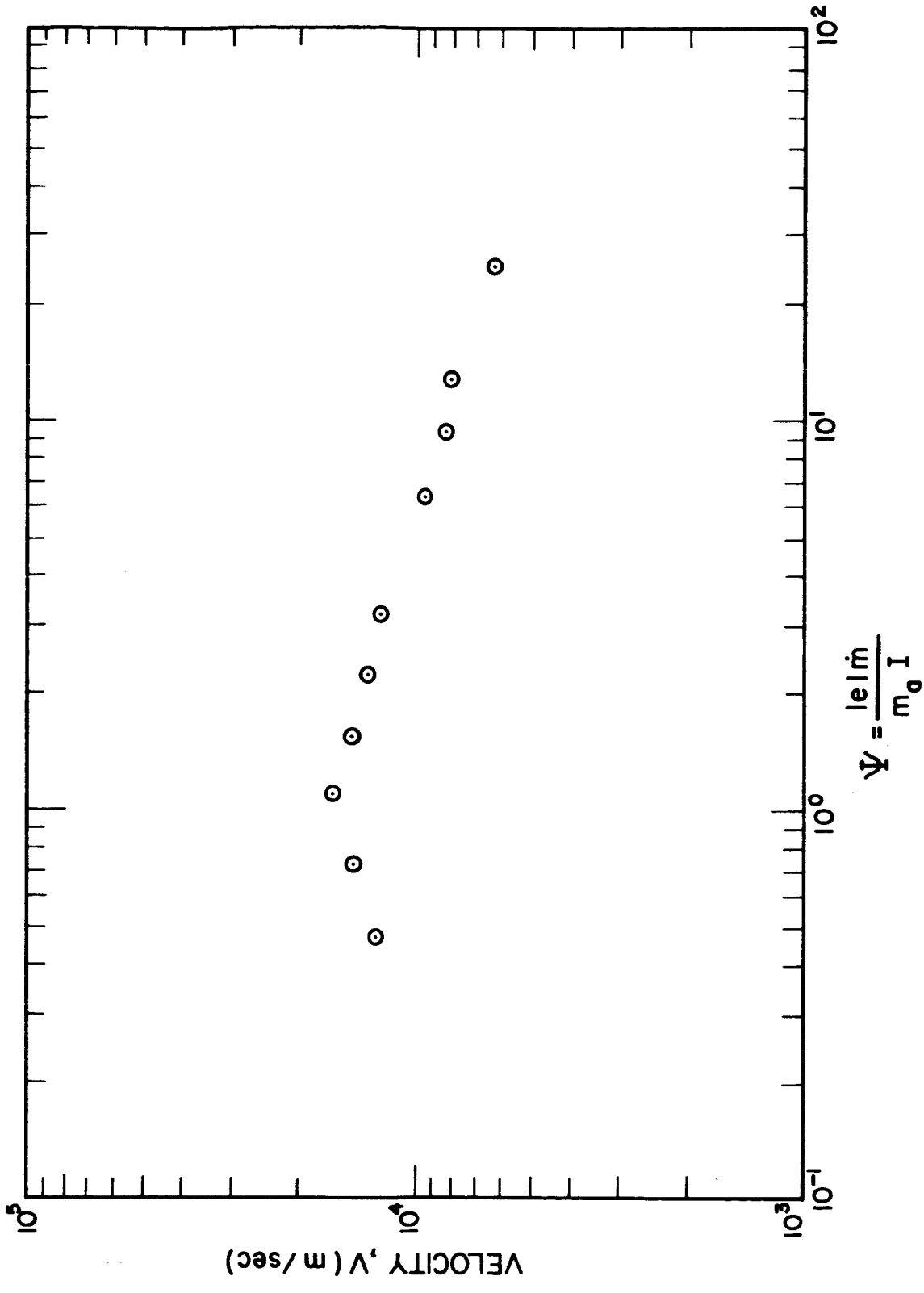

FIG. 6-54 COMPUTED EXIT VELOCITY

the energy has been transferred to the gas inside of the anode cavity, it is possible to establish values for the temperature, dissociation and ionization levels of the gas at the anode exit by using a Mollier chart. The point is determined by the intersection of the enthalpy, $h = \frac{P_G}{\dot{m}}$, and the pressure curves. The information obtained from the Mollier chart is shown in columns 7-9 of Table 6-IX. We can now compute the exit gas temperature from the sonic condition, using the values for ionization and dissociation level found from the Mollier chart

$$T = \frac{u^2_{exit}}{\gamma(1 + \alpha)(1 + \beta)\ R} .$$

These values are shown in columns 4 & 5 of Table 6-IX. Comparing the values of the average gas temperature computed from these two independent calculations will give a good indication of the validity of the assumptions used in the calculations, namely;

1. All of the energy is transferred to the gas inside of the anode cavity.
2. The gas leaves the anode orifice at sonic velocity.
3. The gas is in thermodynamic equilibrium.

The computed temperatures are plotted in Fig. 6-55 as a function of the mass flow non-dimensionalized by the arc current, i.e., $\frac{|e|\dot{m}}{m_a I}$. The two values computed for the average gas temperature agree to within about 10% for values of $\frac{|e|\dot{m}}{m_a I}$ greater than unity. For values of $\frac{|e|\dot{m}}{m_a I}$ less than unity, a sharp divergence between the two computed temperatures occurs. This would seem to indicate that for high values of the mass flow rate, i.e., $\Psi = \frac{|e|\dot{m}}{m_a I} > 1$, most of the energy is transferred from the discharge to the gas inside of the anode cavity, and that as Ψ becomes smaller, larger and larger quantities of energy are transferred to the gas in the exhaust plume. Further evidence to support this tentative conclusion is found in Fig. 6-54 where the computed value for the gas exit velocity peaks at $\Psi = 1$. Also, during the test, it was observed that no structure could

TABLE 6-IX

COMPUTED TEMPERATURES FROM THE ANODE STUDY EXPERIMENT

1	2	3	4	5	6	7	8	9
Ψ	p_{arc} m.m. Hg.	$\dot{m}$ gm/sec	u m/sec	T ^{o}K	h/RT_o	β^* Dis.	α^{**} Ion.	T ^{o}K
24.9	70	.039	6270	3320	196	.73	0	3550
12.8	47.8	.020	8160	4870	268	1.0	0	4500
9.26	36.4	.0145	8400	5150	274	1.0	0	4800
6.39	29.2	.010	9600	6720	314	1.0	0	6700
3.19	20.3	.0050	12,600	10,600	500	1.0	.1	9700
2.22	15.7	.00347	13,400	11,300	606	1.0	.16	10,200
1.53	12.7	.0024	14,900	11,500	896	1.0	.37	11,000
1.10	10.7	.00172	16,300	12,000	1280	1.0	.63	12,000
.722	7.6	.00113	14,800	8,000	1930	1.0	1.0	16,400
.473	5.6	.00074	12,800	6,000	3220	1.0	1.0	51,000
.377	4.3	.00059	--	--	4120	1.0	1.0	76,000
.211	3.3	.00033	--	--	5600	1.0	1.0	92,500

Arc Current - 150 amps

Magnet Current - 1800 amps

* α - Fraction of Atoms Ionized

** β - Fraction of Molecules Dissociated

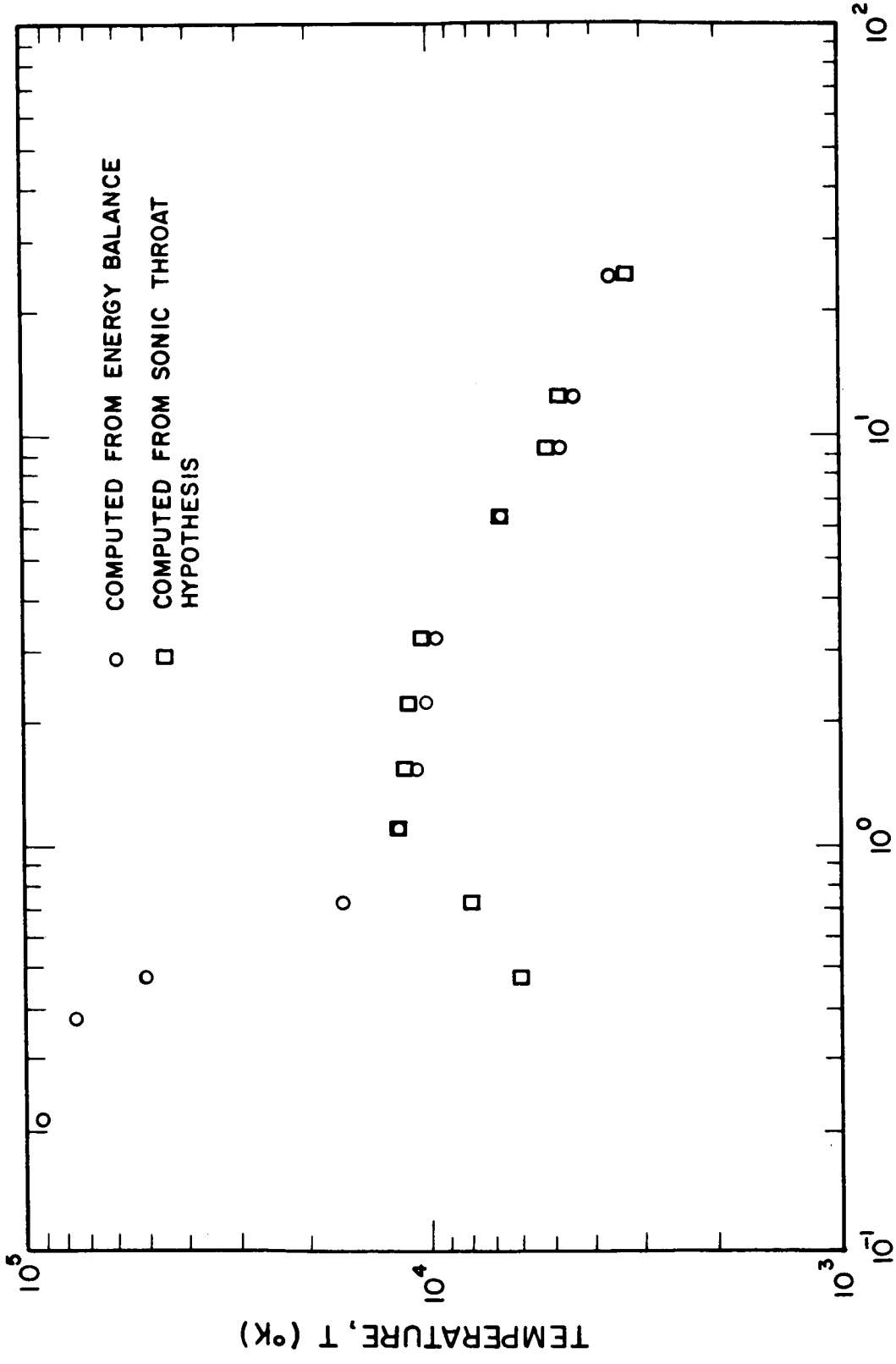

FIG. 6-55 COMPUTED TEMPERATURE VERSUS MASS FLOW RATE PARAMETER

be seen in the exhaust jet for values of $\Psi > 1$, but that the white jet from the cathode* appeared and grew in intensity as the mass flow was further reduced.

Considerable effort was devoted to conducting experiments which would throw light upon the factors determining the current density distribution in the anode. Only limited success was achieved, however, because of a number of experimental problems and the lack of reproducibility from one run to the next. Consequently, the data presented in the following graphs are only representative and no general conclusions concerning the current density distribution on the anode should be drawn.

The distribution of current to each of the three segments is plotted versus the total current in Fig. 6-56. The current to each segment increases linearly with the total current. However, the fraction of the total current carried by each segment changes, mostly between the second and third segments. Changing the pressure in the tank between 50 and 500 μ appears to have no influence on the current distribution among the segments (see Fig. 6-57). Since the pressure in the anode cavity was about 25 mm of Hg, this is not too good an indication that the pressure could not affect the distribution if the tank pressures were raised to values comparable to those in the anode cavity.

Tests were run in an effort to determine if the strength of the applied magnetic field had any effect upon the current distribution to the three anode segments. The results are presented in Fig. 6-58. At the lower magnetic field strengths the anode attachment appears to be moving further back so that the first and second segments take the majority of the current. Over a wide range of field strength, the current density distribution appears to be relatively independent of the magnitude of the field. However, at the stronger fields, the currents appear to be shifting forward onto the third segment.

---

* Characteristic of Hall current accelerators, see Ref. 1.

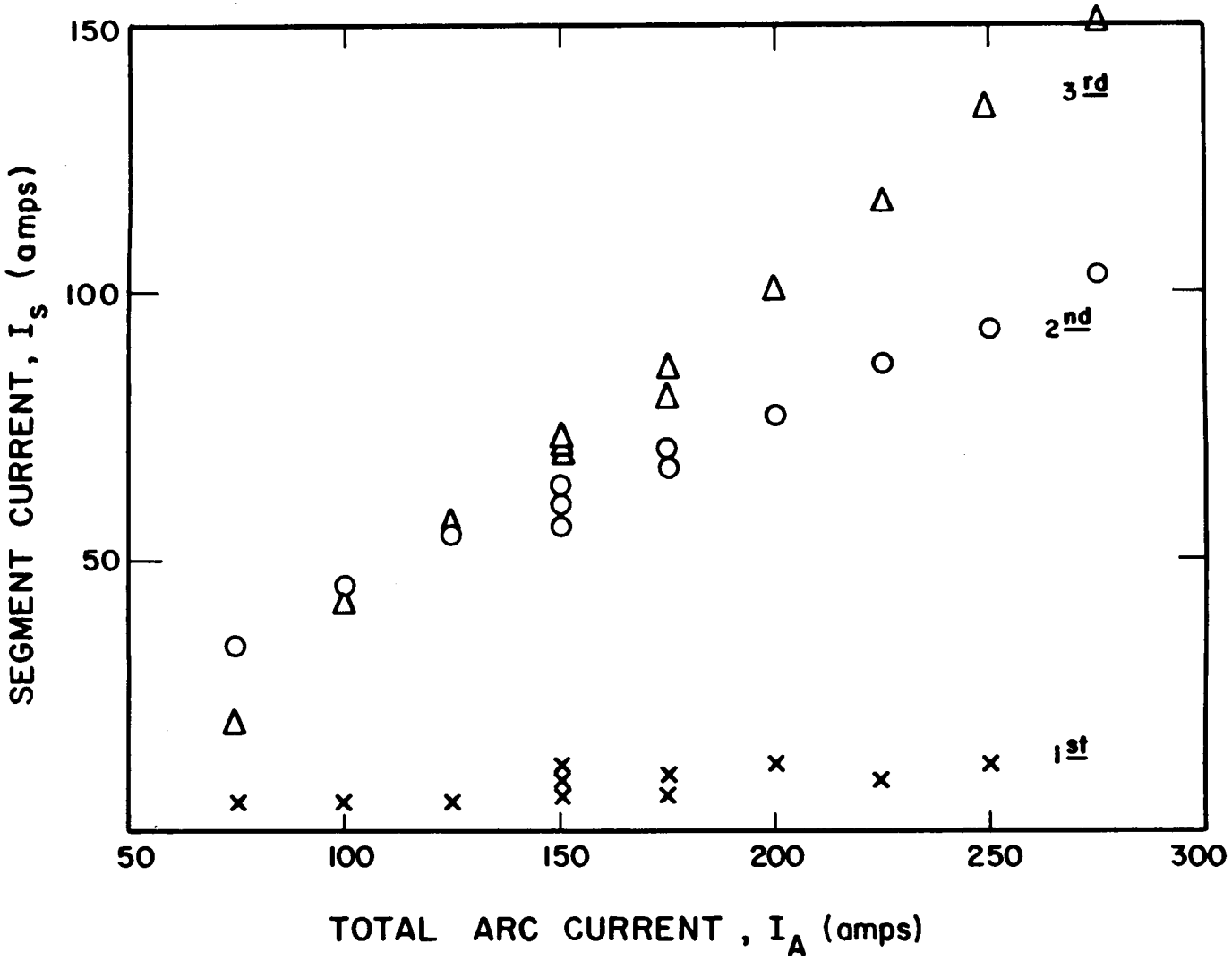

FIG. 6-56 SEGMENT CURRENT VERSUS TOTAL ARC CURRENT

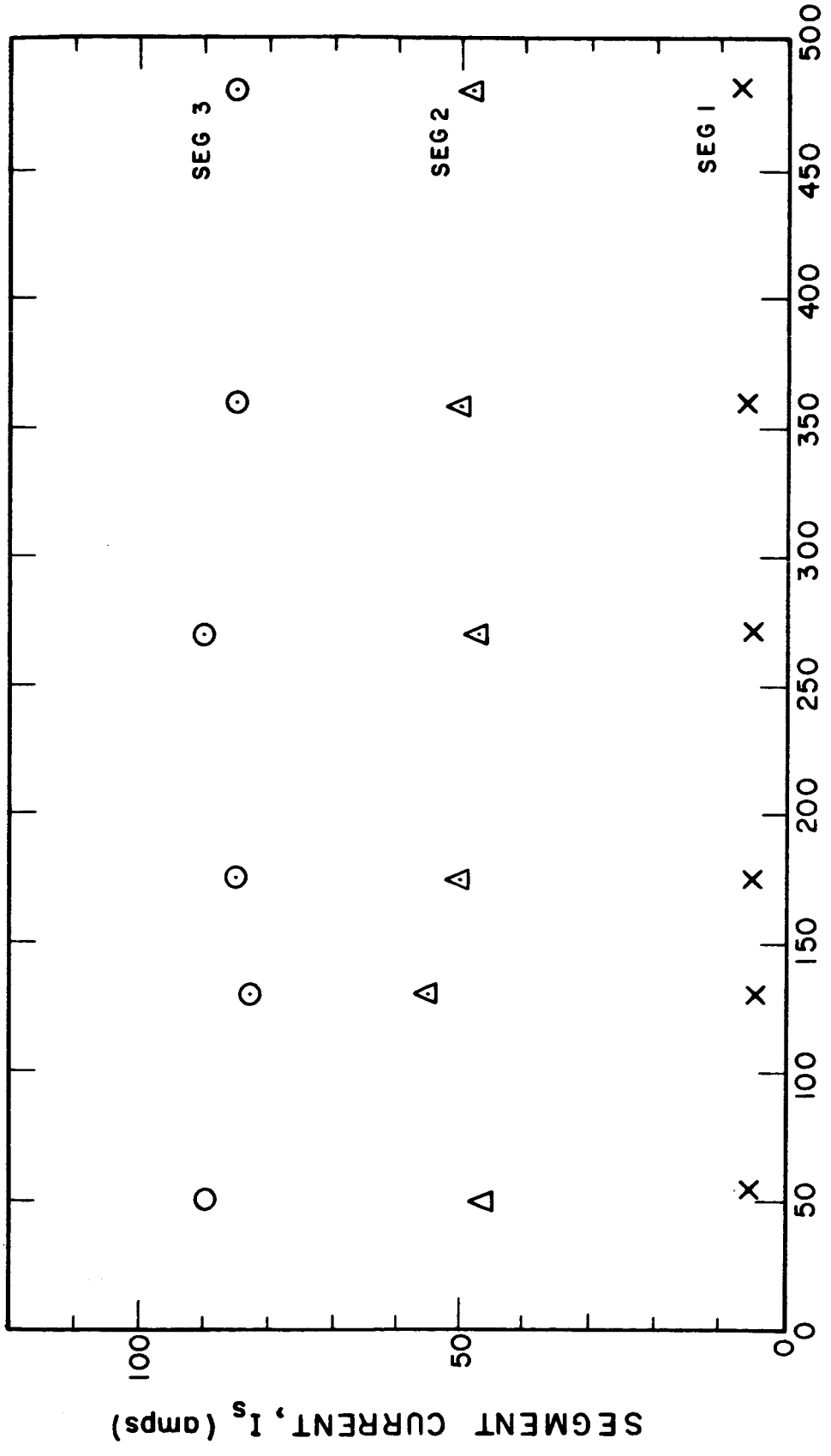

FIG. 6-57 SEGMENT CURRENT VERSUS TANK PRESSURE

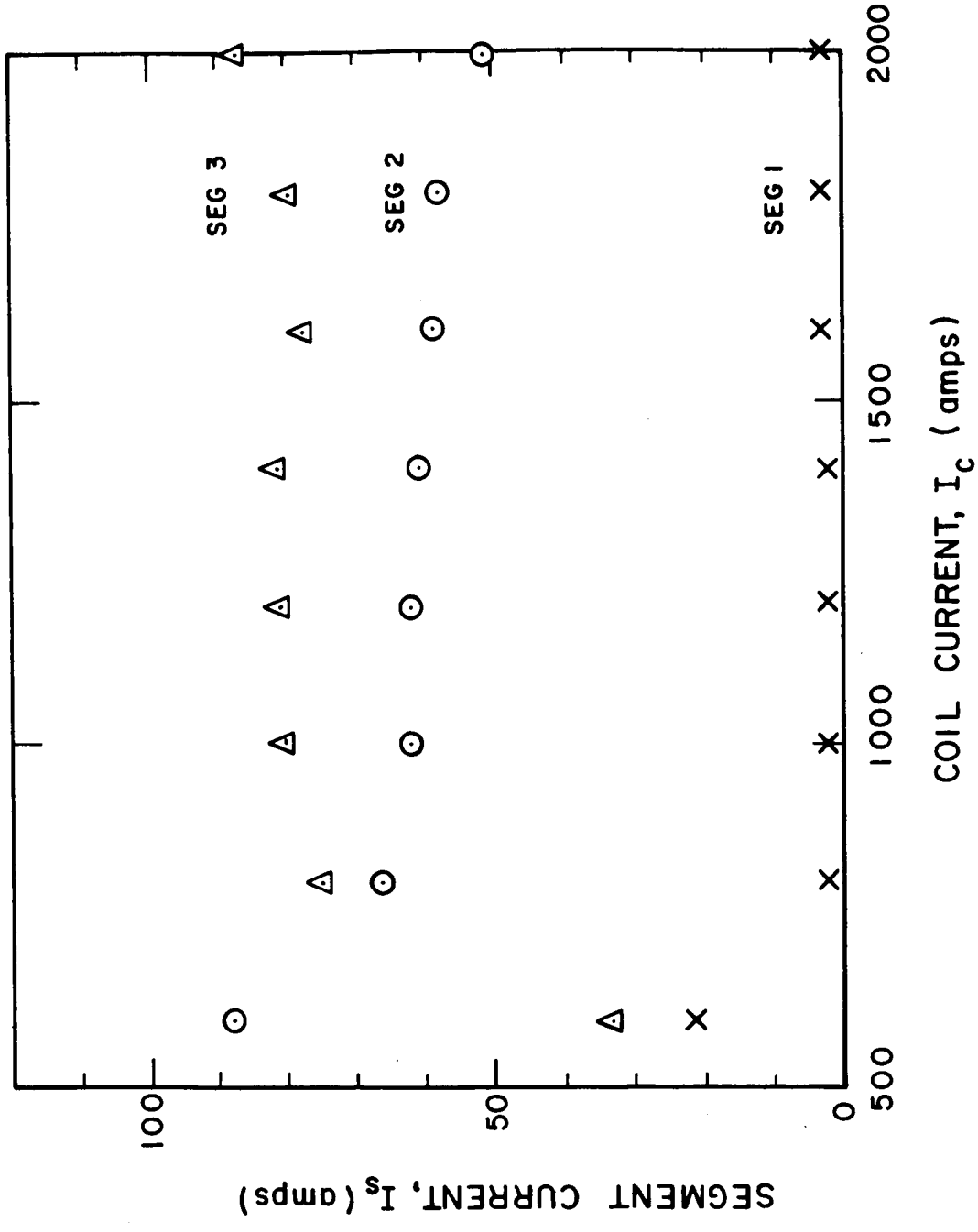

FIG. 6-58 SEGMENT CURRENT VERSUS COIL CURRENT

The manner in which the current density distribution is influenced by the mass flow rate is probably the most difficult to determine from the experimental results. One set of data is presented in Fig. 6-59. The trend observed at high flow rates in this figure was not reproducible and at times the current distribution between segments two and three reversed. However, in all tests the current tended to distribute evenly between segments two and three at low mass flow rates, i.e., $\dot{m} \approx .001$ gm/sec.

The fraction of the total power lost to each segment is shown in Fig. 6-60 as a function of the mass flow rate. Power loss correlates somewhat with current density but is not proportional to it. These results are similar to those found in Refs. 1, 9, and 14, where the power absorbed by the anode could be directly correlated with the sum of the electron condensation power, $I\Phi$, and the convective heat transfer through a boundary layer.

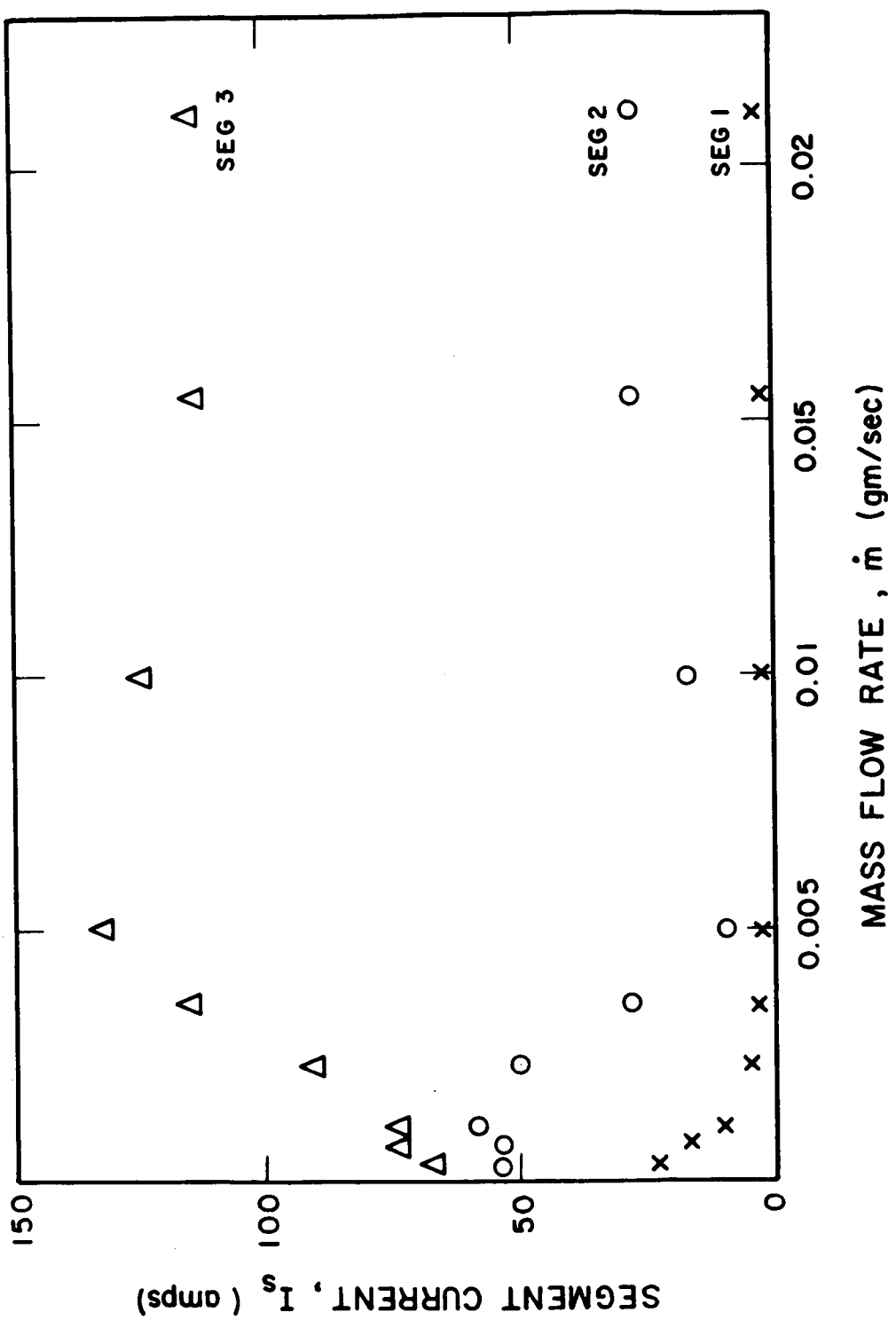

FIG. 6-59 SEGMENT CURRENT VERSUS MASS FLOW RATE

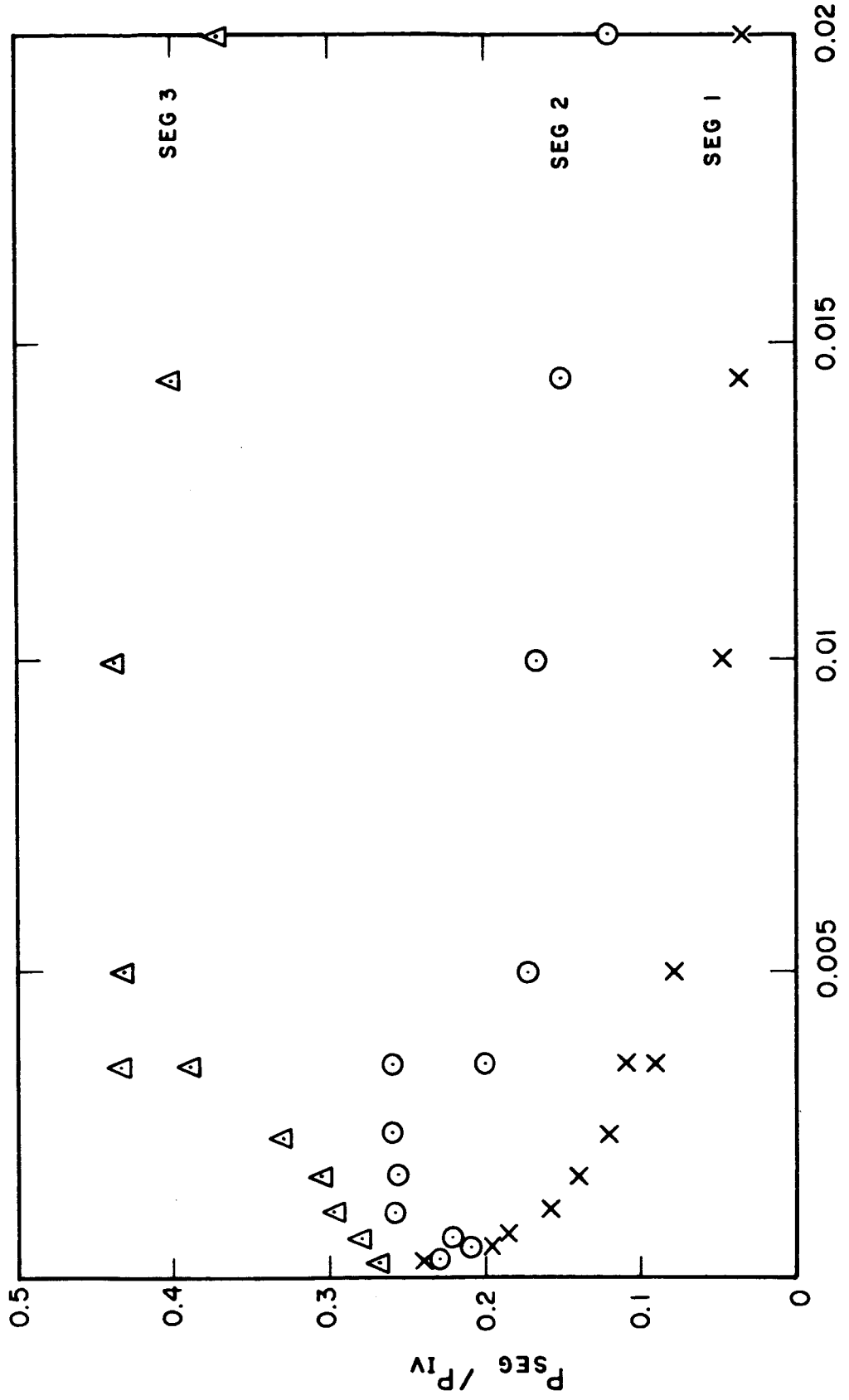

FIG. 6-60 FRACTION OF TOTAL POWER ABSORBED BY SEGMENTS VERSUS MASS FLOW RATE

6.6 Current Density Measurements

Knowledge of the current distributions downstream of a Hall current accelerator is important for understanding the accelerating mechanisms and for optimizing the performance of these devices. The axial component of the current density is more directly measurable than the radial and azimuthal components because it is simply related to the local magnetic field strength. A series of measurements was therefore undertaken to measure the axial current density distribution and to substantiate the qualitative observation that the currents flow far into the region downstream of a Hall accelerator. These experiments are described in this section.

The axial currents in a Hall current accelerator are the only source of a tangential component of the magnetic field. For the case of axial symmetry, derivatives with respect to angular position vanish and one component of the induction law is given by

$$(\vec{\nabla} \times \vec{B}) \cdot \vec{k} = \frac{1}{r}\left[\frac{\partial (rB_\theta)}{\partial r} - \frac{\partial B_r}{\partial \theta}\right] = \frac{1}{r}\frac{\partial (rB_\theta)}{\partial r} = \mu_o J_z \qquad (10)$$

where $\vec{k}$ is a unit vector in the axial direction. The integral form of Eq. 10 is

$$B_\theta(r, z) = \frac{\mu_o}{r}\int_o^r J_z(\rho, z)\, \rho\, d\rho \qquad (11)$$

Thus, measurement of the distribution of $B_\theta(r, z)$ yields $J_z(r, z)$ through use of either Eq. 10 or Eq. 11.

A water-cooled probe suitable for the measurement of $B_\theta(r, z)$ is shown in Fig. 6-61 and described in Ref. 15.

The axial current density downstream of the electrodes of an H_2-1 accelerator was surveyed with the probe. The accelerator was operated with argon under the following conditions:

Mass flow rate of argon	10^{-4} kg/second
Arc current	400 amperes
Arc voltage	110 volts
Arc power	44 kW

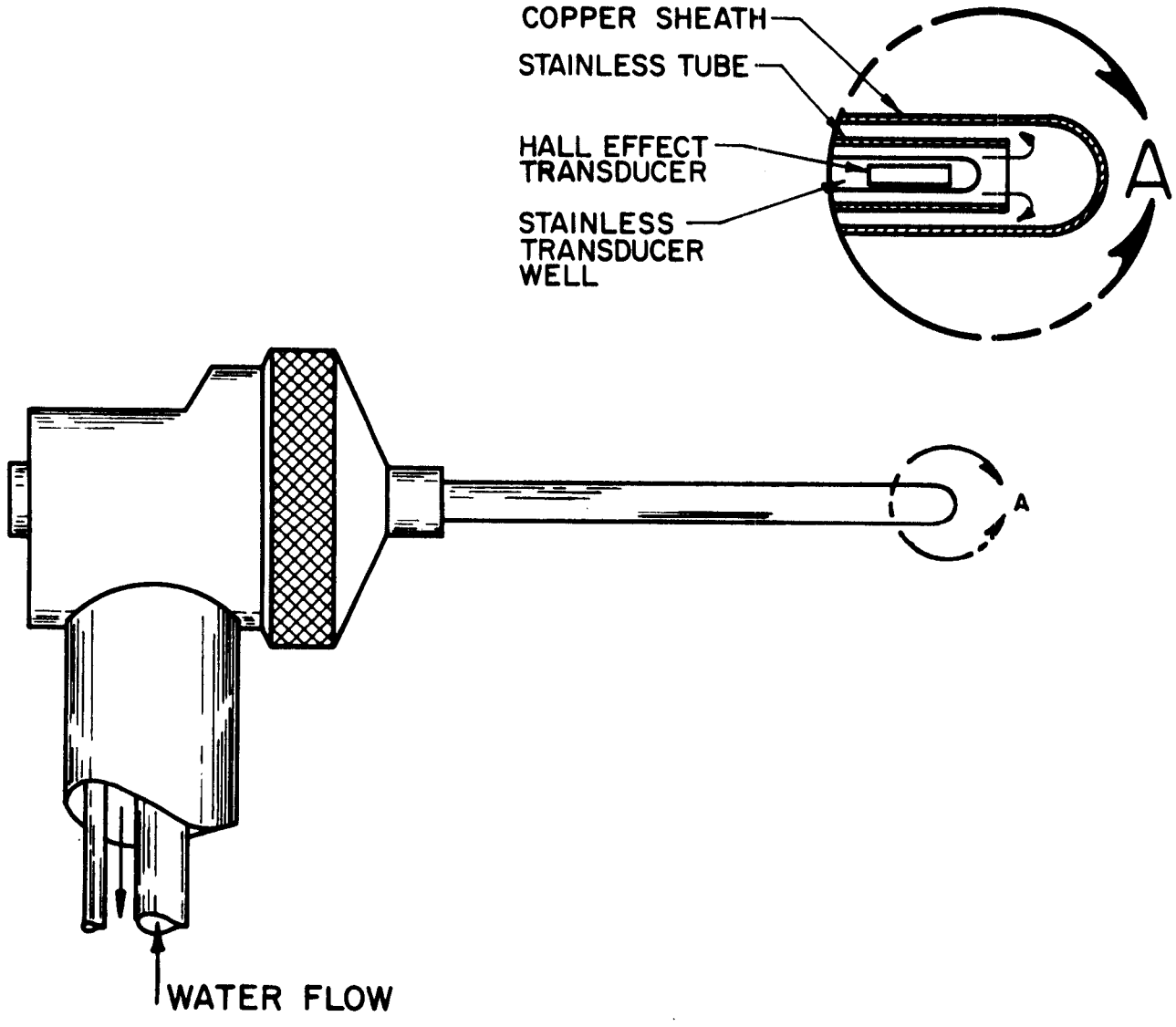

FIG. 6-61 AXIAL CURRENT DENSITY, PROBE, HALL EFFECT TRANSDUCER CARRIED IN WATER COOLED PROBE USED TO MEASURE TANGENTIAL FIELD, B_θ, INDUCED BY AXIAL CURRENT, J_z. ARROWS INDICATE WATER FLOW

Coil current	1800 amperes
Tank pressure	0.09 mm Hg
Power absorbed by coolant	
Anode	12.3 kW
Cathode	0.6 kW

The magnetic field strength and distribution provided by the coil at a current of 1800 amperes is shown in Fig. 6-62. The current distribution which is also shown in Fig. 6-62 follows the field lines closely.

The axial current density distribution was calculated from the measured B_θ distribution using Eq. 10. The values obtained are shown in Fig. 6-63. The measured B_θ was from 1 to 30 gauss.

There were a number of possible sources of error in the experimental results. Since the probe was swung through the discharge on an arc of 12" radius rather than being translated rectilinearly, an orientation error was introduced. At the farthest extreme of the discharge, the probe rotated so that it measured about 91% of B_θ. The relative position of the traces obtained during a test and during calibration was uncertain by about 0.5 cm because of backlash in the position transducer. In reducing the data, the two traces were realigned to make B_θ zero at the centerline. The measured distributions of B_θ were found to be asymmetric by up to 15% in the cases tested. Lack of axial symmetry of the discharge or failure of the probe to respond instantaneously to the local field (finite skin depth) could have caused the asymmetry. Except near the axis of the discharge where the field changes rapidly with position, it is thought that little error was introduced by skin depth effects. Arc attachment to the probe was a possible cause of asymmetry of the discharge. To investigate that possibility, measurements were also performed with the probe covered by a boron nitride sheath. Use of the sheath did not affect the data, indicating that arc attachment was not an important effect under the conditions tested. Since it is difficult to correct accurately for other causes of asymmetry, such as curvature of the jet caused by asymmetrical aerodynamic or electromagnetic forces, the data were reduced by

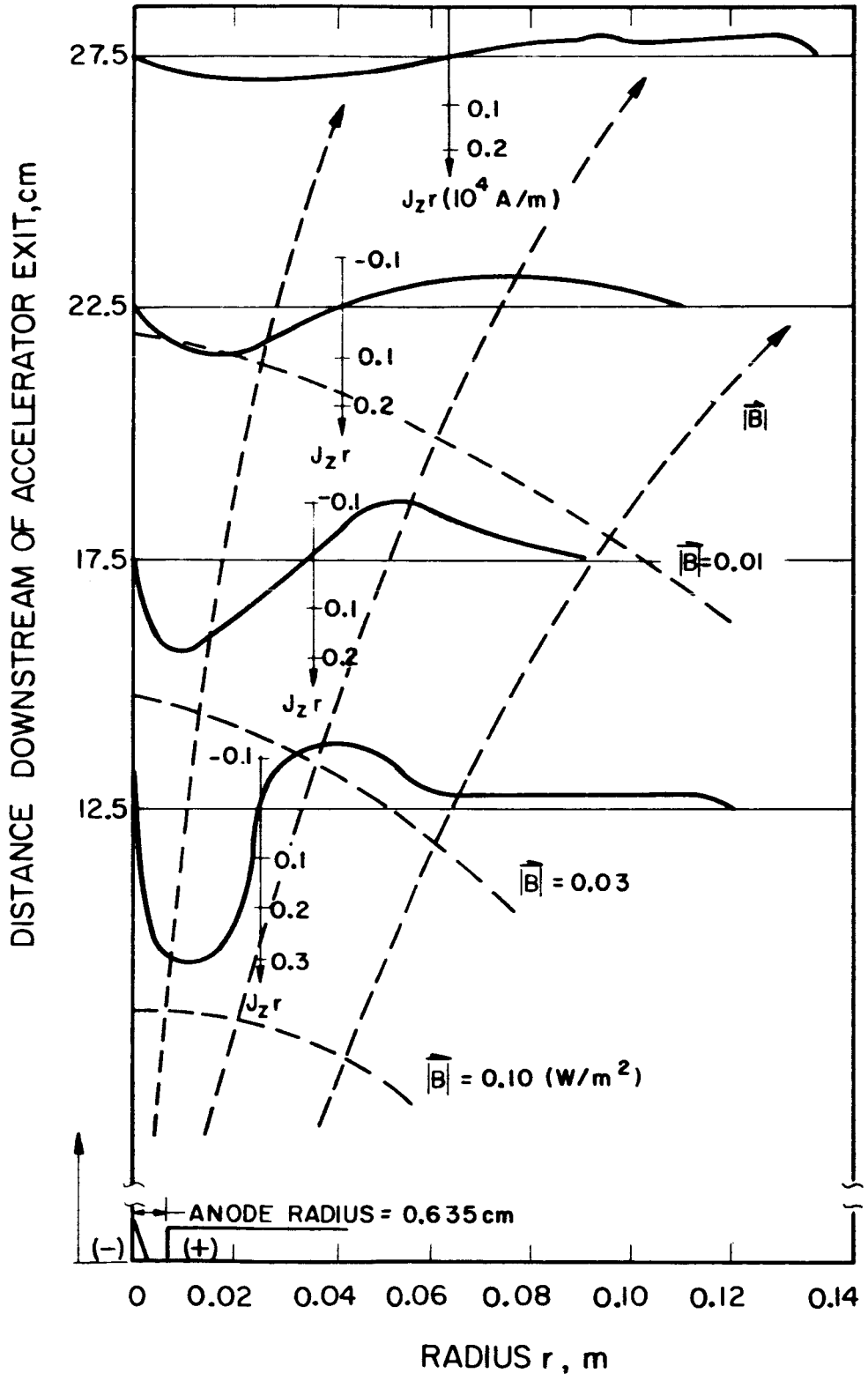

FIG. 6-62 AXIAL AND RADIAL DISTRIBUTIONS OF AXIAL CURRENT DENSITY AND APPLIED MAGNETIC FIELD. CONTOURS OF CONSTANT MAGNETIC FIELD STRENGTH ARE ALSO SHOWN

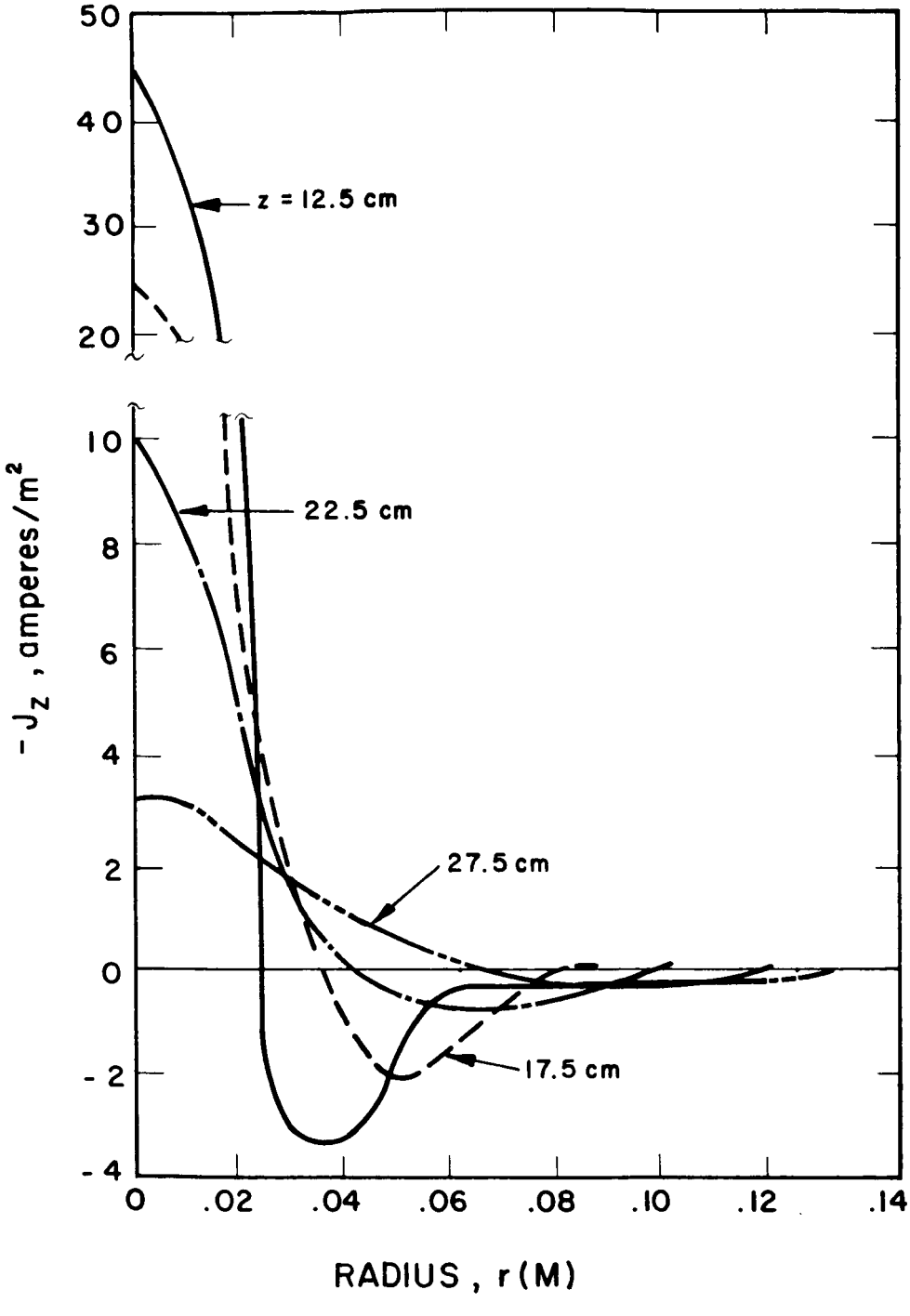

FIG. 6-63 AXIAL CURRENT DENSITY DISTRIBUTION DOWNSTREAM OF A HALL ACCELERATOR

averaging the magnetic field distributions observed on either side of the centerline. Because of these possible sources of error in the data, it is estimated that the final results for the axial current density and the axial currents in the anode and cathode jets are uncertain by about ± 25%.

In an axisymmetric discharge, the current is related to the current density by the relation:

$$I = \int_{r_1}^{r_2} 2\pi r \, J_z \, dr \qquad (12)$$

Therefore, the distribution of rJ_z gives a better physical picture of the current pattern. The observed values of rJ_z are shown in Fig. 6-64. The area under each curve is proportional to the current. The curves of rJ_z in Fig. 6-64 are also shown in Fig. 6-62.

The data substantiate the model of the discharge in a Hall current accelerator that was deduced on the basis of visual observations (Ref. 1). The current (positive current) flows downstream from the anode in a well defined anode jet and returns along the centerline of the stream to form the cathode jet. As the current in the cathode jet is essentially parallel to the magnetic field, it is probably carried mostly by electrons flowing downstream. In the anode jet, where the electronic mobility is reduced by the radial component of the magnetic field, the current is primarily carried by the downstream flow of ions. Radial currents flow from the anode to the cathode jet, causing the total axial current in each jet to decrease with distance from the accelerator. The current in each jet, as a function of axial position, is noted in Fig. 6-64 and plotted in Fig. 6-65. It is seen that the anode and cathode jets persist far downstream of the electrodes. In Fig. 6-61 the shapes of the anode and cathode jets are compared to that of the applied magnetic field. It is seen that the anode and cathode jets follow the field lines fairly closely.

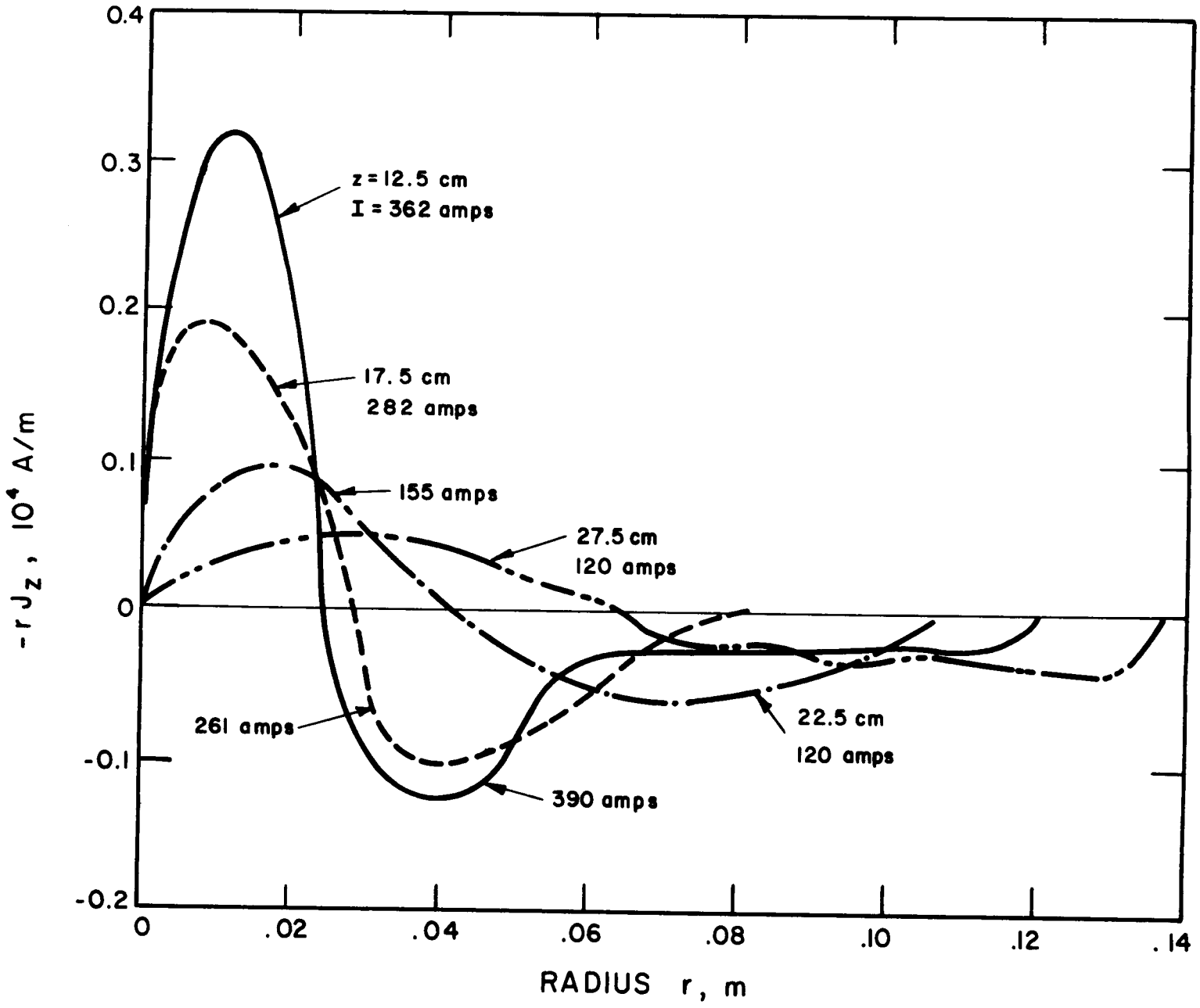

FIG. 6-64 AXIAL AND RADIAL DISTRIBUTION OF rJ_z. AREA UNDER CURVE IS PROPORTIONAL TO TOTAL CURRENT. CURRENTS IN THE ANODE AND CATHODE JETS ARE NOTED FOR EACH AXIAL POSITION

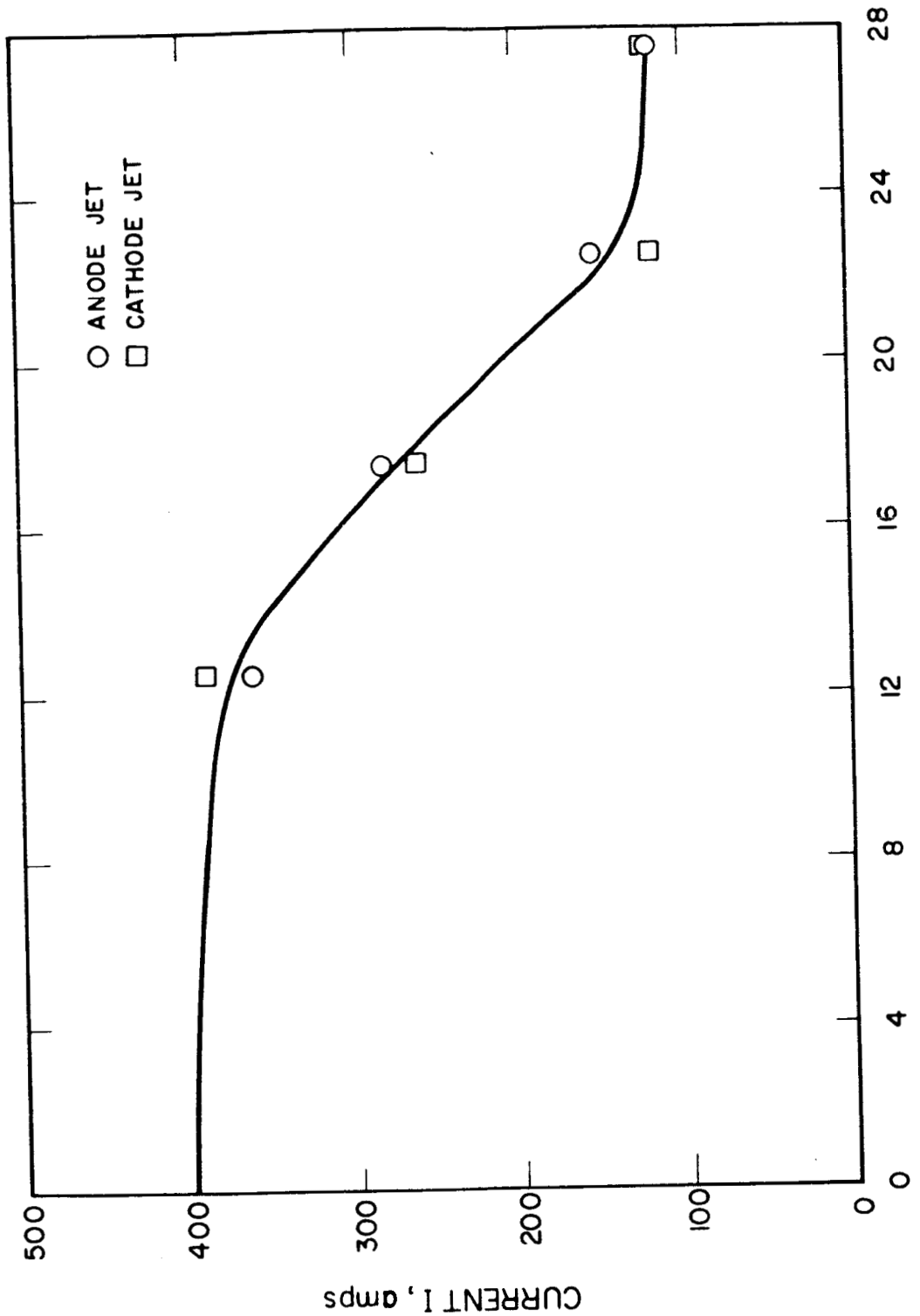

FIG. 6-65 CURRENT CARRIED IN ANODE AND CATHODE JETS AS A FUNCTION OF AXIAL POSITION

7. CONCLUSIONS AND RECOMMENDATIONS

7.1 Thrust Mechanisms and Measurement

1. In all cases a linear relationship between thrust and arc current has been measured if all other controllable variables are maintained constant. This relationship has been found to break down only where the ratio of ion flux rate to arc current falls below a critical value, i.e., $\psi < \psi_{cr}$.
2. The measured thrust has been found to be independent of the mass flow rate of the propellant for values of $\psi > \psi_{cr}$.
3. The measured thrust has been found to remain constant or to rise as the tank pressure is reduced to values lower than 10μ of mercury.
4. The thrust increased initially as the strength of the magnetic field was increased. In some cases the rate of increase dropped to zero at quite low fields and no further change in thrust occurred as the field strength was increased beyond this point.

It has been found possible to explain these trends with an analytic model. In this model the mechanism that contributes the major amount of thrust is the directed kinetic energy transferred to the ions in the discharge. Most of this energy is put initially into ion rotation. A large fraction of this energy later goes into ion axial and radial ion motion by expansion in the magnetic nozzle. The analysis also predicts that a one-to-one relationship should exist between the arc currents and the propellant mass flow rate to obtain the best accelerator performance. If less than the critical flow rate of propellant is used, the electron temperature rises and the power

loss to the anode increases rapidly, decreasing the overall efficiency. If more than the critical flow rate of propellant is used, the excess is not ionized and diffuses out of the engine unused, resulting in poor propellant utilization.

7.2 Electrode Loss Measurements and Mechanisms

1. Whenever measurements were made, it was found that the anode power loss was approximately proportional to the arc current.
2. The power loss to the anode was found to increase as the mass flow rate decreased.
3. In some cases the anode power loss increased as the magnetic field strength was increased. In other cases there was no change in the anode power as the magnetic field strength was varied.
4. The power loss to the anode did not appear to depend upon the pressure in the vacuum tank as it was varied over quite a wide range.

The above results apply to accelerators where the anode attachment occurred on the front face. When this happens, the power transferred to the anode is primarily the power convected into the anode with the electrons which carry the arc current. The trends discussed above then indicate:

1. The electron temperature near the anode surface is independent of the arc current.
2. The electron temperature decreases somewhat as the mass flow rate increases.
3. Increasing the magnetic field either increases the electron temperature near the anode or does not appreciably affect it.
4. The electron temperature at the anode is approximately independent of the tank pressure. This indicates that the values of E/p probably remain constant throughout the accelerator as p is varied. Such a relationship is consistent with the observation that the discharge volume decreases as the pressure increases; the voltage meanwhile remaining constant.

Two types of cathode attachment have been observed. In the gaseous accelerators the arc attached to the tip of a tungsten cone. In the alkali metal accelerator the arc attached to the cathode on the outer surface of the cylindrical portion of the cathode. The power loss to the cathode per unit current was higher in the latter case by about a factor of four. This indicates that point attachment should be used whenever feasible.

REFERENCES

1. G. L. Cann and R. L. Harder, Follow-on Investigation of a Steady State Hall Current Accelerator, Report No. NAS CR-54062, Contract NAS3-3568, NASA-Lewis Research Center, 30 October 1964

2. R. A. Moore, G. L. Cann, and L. R. Gallagher, High Specific Impulse Thermal Arc Jet Thrustor Technology, AFAPL-TR-65-48, Part I, Air Force Aero Propulsion Laboratory, June 1965

3. S. Domitz, H. Ferguson, J. S. Sovey, and H. R. Hunczak, Private Communication of results of low-pressure test of EOS hydrogen accelerator, January 1965

4. G. L. Cann, P. D. Lenn, and R. L. Harder, Hall Current Accelerator, First Quarterly Progress Report on Contract NAS3-5909, 5 October 1964

5. R. M. Patrick and W. E. Powers, Plasma Flow in a Magnetic Annular Arc Nozzle, AVCO-Everett Research Labs, Contract AF 49(638)-659

6. G. L. Cann, R. L. Harder, and J. Glass, Hall Current Accelerator, First Monthly Progress Report, Contract NAS3-5909, 20 December 1964

7. G. L. Cann and R. L. Harder, Study of Electrode Attachment Regions in High Current Gaseous Discharges, AEDC-TDR-64-107, Arnold Engineering Development Center, August 1964

8. G. L. Cann, et al, Basic Research on Gas Flows Through Electric Arcs - Hot Gas Containment Limits, ARL Report 64-49, Aeronautics Research Lab, March 1964

9. G. L. Cann, R. A. Moore, R. D. Buhler, and G. L. Marlotte, Thermal Arc Jet Research, ASD-TDR-63-632, Air Force Aero Propulsion Laboratory, 15 August 1963

10. AVCO Corporation, RAD Division, Arc Jet Technology Research and Development, First Quarterly Progress Report, by R. R. John, Contract NAS3-5900, Boston, Mass., 9 October 1964

11. R. A. Moore, G. L. Cann, et al, High Specific Impulse Thermal Arc Jet Thrustor Technology, Interim Technical Report on Contract AF 33(615)-1579, Air Force Aero Propulsion Laboratory, 30 November 1964

12. R. R. John, Private Communication, December 1964

13. R. V. Hess and P. Brockman, Private Communication, December 1964

14. G. L. Cann, et al, Heat Transfer Study for Arc Jet Engines, Part A, NASA-Lewis Research Center, Contract NAS8-2548, Final Report, 18 October 1962

15. G. L. Cann, P. D. Lenn, and R. L. Harder, Hall Current Accelerator, Second Quarterly Progress Report, Contract NAS3-5909, 20 December 1964

SUMMARY REPORT DISTRIBUTION LIST

CONTRACT NAS3-5909

NASA Headquarters
FOB - 10B
600 Independence Avenue, Southwest
Washington, D. C. 20546
Attn: RNT/James Lazar (3)
RRP/Dr. K. H. Thom (1)

NASA-Langley Research Center (2)
Langley Air Force Base, Virginia 23365
Attn: M. Ellis

NASA-George C. Marshall Space Flight Center (1)
Huntsville, Alabama 35812
Attn: M-RP-DIR/E. Stuhlinger

NASA-Ames Research Center (1)
Moffett Field, California 94035
Attn: G. Goodwin

Jet Propulsion Laboratory (1)
Institute of Technology
4800 Oak Grove Drive
Pasadena, California 91103
Attn: J. J. Paulson

Commander/Aeronautical Systems Division (2)
Wright-Patterson Air Force Base, Ohio 45433
Attn: AFAPL(APIE)/R. Supp

Office of Scientific Research, USAF (1)
Washington, D. C. 20025
Attn: (SRMP)/Dr. M. Slawsky

NASA Scientific and Technical Information Facility (6)
P. O. Box 33
College Park, Maryland 20740
Attn: NASA Representative RQT-2448

NASA-Lewis Research Center
21000 Brookpark Road
Cleveland, Ohio 44135
Attn: Spacecraft Technology Division
J. H. Childs (3)
S. Domitz (30)
H. Hunczak (1)
Attn: Electromagnetic Propulsion Division
G. Seikel (1)
W. Moeckel (1)
R. E. Jones (1)
Attn: Library (2)
Attn: Technology Utilization Office (1)
John Weber
Attn: Spacecraft Technology Procurement Section (1)
J. H. DeFord

Electro-Optical Systems, Inc. (1)
125 North Vinedo Avenue
Pasadena, California 91107
Attn: G. L. Cann

Aeronutronic Division (1)
Philco Corporation
Ford Road
Newport Beach, California
Attn: R. M. Spongberg/ATC

General Dynamics/Astronautics (1)
P. O. Box 1128
San Diego, California 92112
Attn: T. J. Gooding

Thermal Mechanical Research Laboratory (1)
OAR USAF
Wright-Patterson Air Force Base, Ohio 45433
Attn: Eric Soehngen

Giannini Scientific Corporation (1)
3839 South Main Street
Santa Ana, California 92702
Attn: Mr. A. Ducati

AVCO Corporation (1)
Research & Advanced Development Division
201 Lowell Street
Wilmington, Massachusetts 01887
Attn: Dr. R. R. John

Professor C. C. Chang (1)
Department of Space Sciences and Applied Physics
Catholic University of America
Washington, D. C. 20017

AVCO-Everett Research Laboratory (1)
2385 Revere Beach Parkway
Everett 49, Massachusetts
Attn: Dr. R. M. Patrick

Space Sciences, Incorporated (1)
301 Bear Hill Road
Waltham, Massachusetts 02154
Attn: Joseph M. Proud

General Electric Company (1)
Missile and Space Division
P. O. Box 8555
Philadelphia, Pennsylvania 19101
Attn: Dr. P. Gloersen

Princeton University (1)
Forrestal Research Center
Princeton, New Jersey
Attn: Dr. R. G. Jahn

Los Alamos Scientific Laboratory (1)
P. O. Box 1663
Los Alamos, New Mexico
Attn: Dr. T. F. Stratton

AFWL (1)
Kirtland Air Force Base, New Mexico
Attn: Capt. C. F. Ellis/WLPC

Aerospace Corporation (1)
P. O. Box 95085
Los Angeles, California 90045
Attn: Library Technical Documents Group

Westinghouse Astronuclear Laboratories (1)
Pittsburgh, Pennsylvania 15234
Attn: Mr. H. W. Szymanowski, Mgr.
Electrical Propulsion Laboratory